University of Southampton Research Repository

UNIVERSITY OF SOUTHAMPTON

Faculty of Medicine

Clinical & Experimental Sciences

‘Investigating the Host-Pathogen Interaction in Tuberculosis by Bioelectrospray 3D Cell Culture Modelling and Label-Free Imaging’

by

Eleni Konstantinopoulou

ORCiD ID: 0000-0003-4077-9648

PhD Thesis

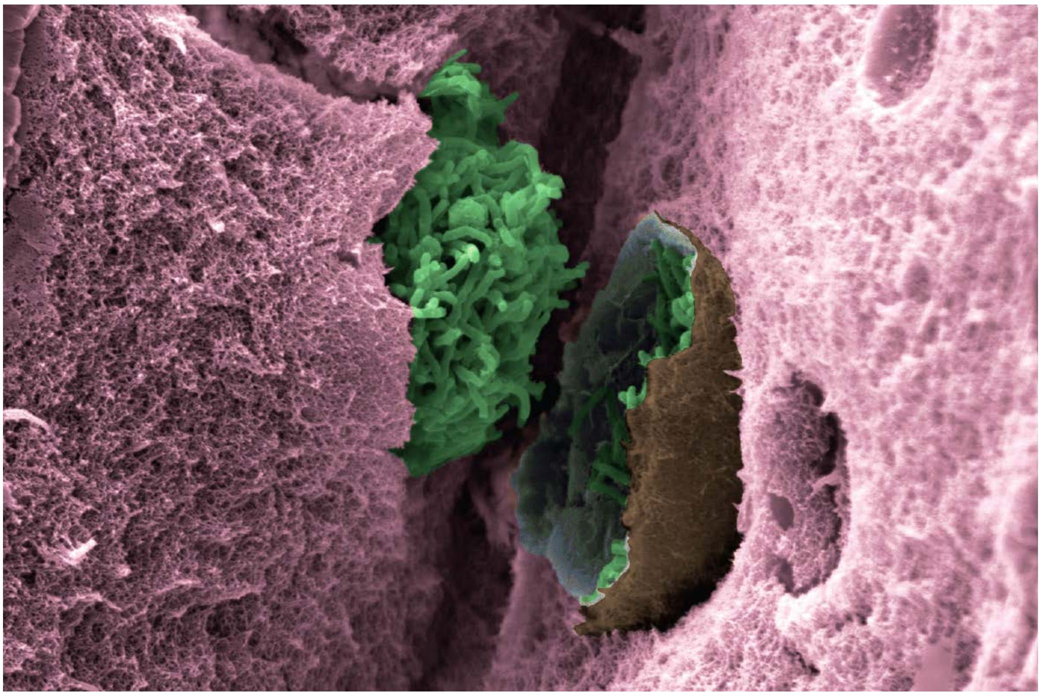

September 2020

University of Southampton

Abstract

Faculty of Medicine
Clinical & Experimental Sciences
Doctor of Philosophy

Investigating the host-pathogen interaction in tuberculosis using emerging imaging modalities

by
Eleni Konstantinopoulou

Tuberculosis is a deadly infectious disease caused by the bacterium *Mycobacterium tuberculosis* (*Mtb*). It constitutes a major cause of death worldwide with approximately 1.5 million people dying from TB every year.[1-6] Traditional animal models as well as conventional 'two-dimensional' cell cultures do not accurately mimic human tuberculosis infection *in vivo*, such as the formation of caseating granulomas and degradation of extracellular matrix.

We study a bioelectrospray-generated 3D cell culture model of tuberculosis, using diverse imaging techniques. In the 3D culture, *Mtb*-infected PBMCs (strains: H37Rv, 0414B) are mixed with an alginate-collagen gel. We investigated the host-pathogen interaction at high resolution at various stages of infection using Transmission Electron Microscopy (TEM). We used Micro-Computed Tomography (μCT) to show distribution of PBMCs in 3D in comparison to a human tuberculous lung biopsy. This was then correlated to traditional H&E, and matrix staining of the sectioned tuberculous human lung block. Using label-free microscopy [Coherent Anti-Stokes Raman Scattering (CARS), Second Harmonic Generation (SHG), Two-Photon Excitation Fluorescence (TPEF)], PBMC aggregation and collagen fibres were imaged in the microspheres.

More lipid bodies were detected by TEM in the *Mtb*-infected samples than the uninfected controls. TEM and SHG imaging revealed collagen fibres attached to the surface of PBMCs. CARS microscopy showed that infection with *Mtb,* as well as the presence of collagen in the 3D matrix, influence the number of PBMC aggregates forming within the 3D culture. Preliminary data from μCT indicate that this technique can provide quantitative data on PBMC aggregates in 3D that can be cross-correlated with human biopsies.

A correlative imaging approach between traditional and emerging imaging modalities is necessary in order to gain new insight into the host-pathogen interaction in tuberculosis.

Table of Contents

List of Figures

List of Tables

List of Accompanying Materials

A DVD containing the following supporting material:

1. Video 1 - corresponding to Figure 30
   Description: Video going through the micro-CT scan dataset of an unstained human lung biopsy from a patient with active TB.

2. Video 2 - corresponding to Figure 31
   Description: Video showing a 360° rotation of a 3D representation of the micro-CT scan of an unstained human lung biopsy.

3. Videos 3-14 - corresponding to Figure 53
   Description: SHG z-stacks of microspheres at days 1, 7 and 14 of infection. Each one will be named after the corresponding panel in Figure 54.

4. Video 15 - corresponding to Figure 64
   Description: Micro-CT scanning of a resin block revealed aggregate-bearing microspheres at day 14 after infection with the laboratory strain H37Rv. Manual segmentation was performed in Amira to visualise aggregates (blue), as well as individual cells (yellow) and microspheres (red).

Research Thesis: Declaration of Authorship

Print name: Eleni Konstantinopoulou

Title of thesis: Investigating the host-pathogen interaction in tuberculosis using emerging imaging modalities

I declare that this thesis and the work presented in it are my own and has been generated by me as the result of my own original research.

I confirm that:

1. This work was done wholly or mainly while in candidature for a research degree at this University;
2. Where any part of this thesis has previously been submitted for a degree or any other qualification at this University or any other institution, this has been clearly stated;
3. Where I have consulted the published work of others, this is always clearly attributed;
4. Where I have quoted from the work of others, the source is always given. With the exception of such quotations, this thesis is entirely my own work;
5. I have acknowledged all main sources of help;
6. Where the thesis is based on work done by myself jointly with others, I have made clear exactly what was done by others and what I have contributed myself;
7. None of this work has been published before submission

Signature: Date:

Acknowledgements

First of all, I would like to thank my supervisors, Paul Elkington, Liku Tezera and Sumeet Mahajan for their help and support throughout these last four years. Thank you for giving me the opportunity to undertake a PhD in the UK and for teaching me all the laboratory/transferrable/life skills a PhD-level student should have. I will be eternally grateful to Magda Bielecka and Kostas Bourdakos who – even though they were not formally part of my supervisory team – took the time to train me in various laboratory techniques, helped me whenever I needed it and answered all my questions!

This study would not have been possible without the invaluable support of all staff members in the Biomedical Imaging Unit (BIU), University Hospital Southampton (UHS) for training me in all microscopy techniques used in this thesis and all subsequent image analysis. Special thanks to Regan Doherty and Lizzie Angus for training me and always being there to help and answer my questions; David Chatelet for teaching me all the necessary image analysis software packages and always being available for troubleshooting (even after hours at times..!); Mat Lawson for all his help in image processing and analysis of our lung biopsy dataset (and the endless banter); and Dave Johnston and Anton Page for supporting me and my project and showing genuine interest in my progression as a PhD student. Thank you all, I could not have done this without you.

I would also like to thank Susan Wilson, the Head of the Histochemistry Research Unit (HRU) for collaborating with us in this project and to give special thanks to Jenny Norman and Jamila McRobb for training me in histological staining of tissue sections and for all the work they did for us. I am also grateful to Monette Lopez from the Wessex Investigational Sciences Hub (WISH) laboratory for performing as a service all immunohistochemistry staining included in this thesis.

I would like to thank Peter Lackie and Philipp Schneider for their patience, support and understanding during the last six months while I was writing my PhD thesis and working for them as a Research Fellow in parallel. I am extremely grateful to you for giving me this job and supporting me during these (stressful) times of PhD write-up.

Finally, I would like to thank Miltos Fotopoulos for all his help and support during my PhD, without which I wouldn’t have made it, and my parents and brother, Jason, for their love and support (and for putting up with my endless moaning)! Thank you all for being there with me every step of the way in body and/or in spirit.

List of Abbreviations

Abbreviation	Meaning	Page number
2D	Two-dimensional	15
3D	Three-dimensional	15
ASC	Adipose-derived stem cell	27
BES	Bioelectrospray	37
BF	Bright-field	51
BIU	Biomedical Imaging Unit	58
BSL-III	Biosafety level 3	30
CARS	Coherent anti-Stokes Raman scattering	23
CCD	Charged couple device	39
CN	Caseous necrosis	74
COPD	Chronic obstructive pulmonary disease	11
DDR1, 2	Discoidin domain receptor 1, 2	10
ECM	Extracellular matrix	10
EVG	Elastin van Gieson	60
FFA	Free fatty acid	28
FFPE	Formalin-fixed paraffin-embedded	31
FITC	Fluorescein isothiocyanate	105
FoV	Field of view	109
fps	frames per second	54
G	α-L-guluronic acid	19
GPVI	Glycoprotein VI	10
H&E	Haematoxylin & Eosin	60
HBSS	Hank's balanced salt solution	20
HEPES	4-(2-hydroxyethyl)-1-piperazineethanesulfonic acid	35
hESC	Human embryonic stem cell	27
HIER	Heat-induced epitope retrieval	62
HIV	Human immunodeficiency virus	3
hMSC	Human mesenchymal stem cell	29
HPV	Human papilloma virus	27
IfLS	Institute for Life Sciences	52
IGRA	Interferon-γ release assay	4
IHC	Immunohistochemistry	62
ILI	Intracytoplasmic lipid inclusion	9
INH	Isoniazid	30
IR	Infrared	21
kDa	Kilodalton	19
LAIR-1	Leukocyte-associated immunoglobulin-like receptor 1	10
LAM	Lipoarabinomannan	11
LB	Lipid body	9
LUT	Look-up table	54
LWD	Long working distance	43
M	β-D-mannuronic acid	19
MDR-TB	Multi drug-resistant tuberculosis	3

MGC	Multinucleated Giant Cell	8
Micro-CT	Micro-Computed Tomography	31
MMP	Matrix metalloproteinase	11
MOI	Multiplicity of infection	36
MPD	MicroParticle Diluent	38
MSC	Microbiological safety cabinet	37
Mtb	*Mycobacterium tuberculosis*	3
mW	milliWatt	39
NA	Numerical aperture	39
NAAT	Nucleic acid amplification test	4
NIR	Near-infrared	21
NK cell	Natural killer cell	8
NTM	Non-tuberculous mycobacteria	30
PBMC	Peripheral blood mononuclear cell	19
PBS	Polarising beam filter	50
PCA	Principal component analysis	27
RT-PCR	Reverse-transcription polymerase chain reaction	27
PD-1	Programmed cell Death protein-1	62
PD-L1	Programmed cell Death Ligand-1	62
PFA	Paraformaldehyde	38
PI	Propidium iodide	55
PIPES	Piperazine-N,N’ – bis(2-ethanesulfonic acid)	38
PMT	Photomultiplier tube	47
RR-TB	Rifampicin-resistant tuberculosis	3
SBF-SEM	Serial block-face scanning electron microscopy	146
SEM	Scanning electron microscopy	31
SERS	Surface-enhanced Raman spectroscopy	28
SHG	Second harmonic generation	19
Si	Silicon	39
SNR	Signal-to-Noise Ratio	42
SWD	Short working distance	43
TAG	Triacylglyceride	9
TB	Tuberculosis	3
TDR-TB	Totally drug-resistant tuberculosis	3
TEM	Transmission Electron Microscopy	31
TERS	Tip-enhanced Raman spectroscopy	29
TIMP	Tissue inhibitors of metalloproteinase	11
TLR	Toll-like receptor	12
TNF-α	Tumour necrosis factor α	7
TPEF	Two-photon excitation fluorescence	25
TRS	Target Retrieval Solution	62
TST	Tuberculin skin test	4
UHS	University Hospital Southampton	58
WHO	World Health Organisation	3
WISH	Wessex Investigational Sciences Hub	62
XDR-TB	Extensively drug-resistant tuberculosis	3
ZN	Ziehl-Neelsen	61

Chapter 1

-

Introduction

Chapter 1. Introduction

1.1. Tuberculosis

Tuberculosis (TB) is an infectious disease caused by an acid-fast bacillus, *Mycobacterium tuberculosis* (*Mtb*),[1,2,7] which can cause latent or active tuberculosis, depending on its physiological state.[2] It is a leading cause of death worldwide and especially in low- and middle-income countries (*Figure 1*)[2,3,7] as it is responsible for the deaths of approximately 1.5 million people every year, while almost 2 billion people in total are thought to be latently infected.[1,2,8] It is estimated that in 2018 there were 10 million new cases of tuberculosis and 8.6% all TB cases globally were people with Human Immunodeficiency Virus (HIV), according to the World Health Organisation (WHO).[4] Tuberculosis usually affects the lungs (pulmonary TB), but can also affect other vital organs (extra-pulmonary TB).[9]

FIG. 3.4

Estimated TB incidence rates, 2018

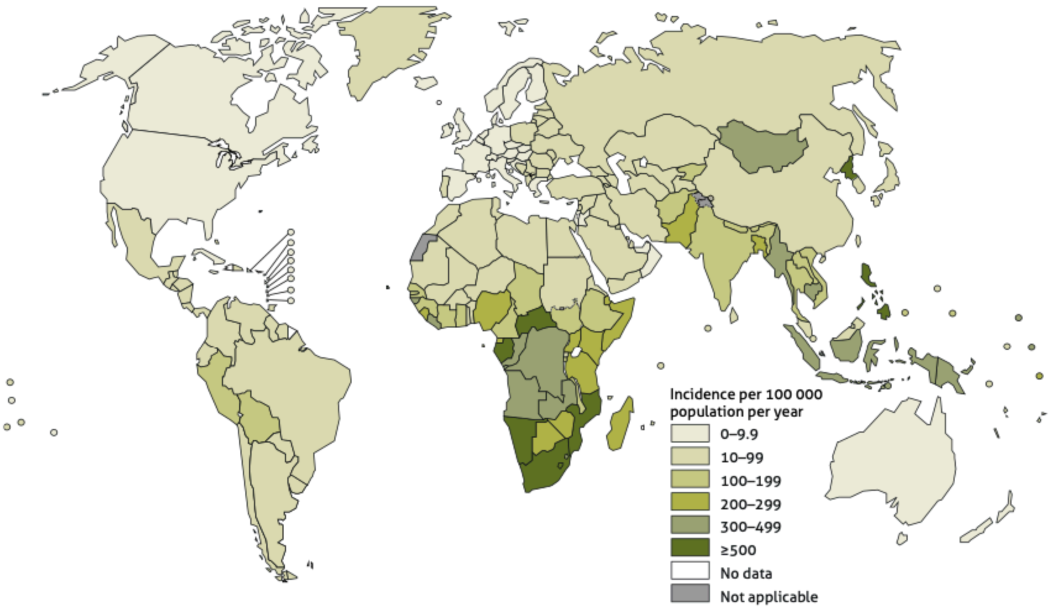

Figure 1. Estimated tuberculosis incidence rates in 2018.

According to the World Health Organization (WHO) 'Global Tuberculosis Report 2019', in 2018, the eight countries with the highest TB burden worldwide were India, China, Indonesia, the Philippines, Pakistan, Nigeria, Bangladesh and South Africa, accounting for two thirds of the total number of new TB cases. *(Source: WHO, Global Tuberculosis Report 2019)*[4]

During the last two decades, multidrug-resistant (MDR) strains of *M. tuberculosis* have emerged[10] and are currently on the rise[3,11] with about 500,000 new cases of rifampicin-resistant TB (RR-TB), 78% of which were ultimately proven to be MDR-TB in 2018.[4] Extensively drug-resistant (XDR-TB) and totally drug-resistant *Mtb* strains (TDR-TB) have also emerged and are causing major disruptions in the global efforts for lowering the burden of TB. Delays in diagnosis due to slow or inaccurate testing, lack of specialist laboratory facilities and suitably trained staff in resource-limited countries, as well as reckless use of antibiotics, can allow for more widespread transmission of potentially resistant *Mtb* strains.[12]

The first step to substantially reduce transmission of TB is to find ways to diagnose the disease more rapidly and effectively. Traditional diagnosis of TB consists of three main tests apart from the standard chest X-ray; the tuberculin skin test (TST), clinical evaluation of the symptoms, and sputum smear microscopic examination. These tests have been characterized as laborious, insensitive, and inefficient, as they are all personnel-dependent. More recent immunological and molecular tests[7,12,13] such as Interferon-γ Release Assay (IGRA)[7,12,14] have been developed but are unable to distinguish between active and latent disease. The *Mtb* nucleic acid amplification test (NAAT) can also predict drug-resistance, but it is expensive and requires the existence of a sophisticated resource setting.[7,12] The need for highly sensitive, rapid and economic point-of-care tests for TB and for drug-susceptibility to prevent transmission and inappropriate antibiotic administration is increasingly more apparent.[7,11,12]

MDR-TB is defined as resistant to at least rifampicin and isoniazid[10] and XDR-TB as resistant to rifampicin, isoniazid, all fluoroquinolones, and one of the following three injectable drugs: kanamycin, amikacin and capreomycin.[10,12] TDR-TB on the other hand is resistant to all medications available against tuberculosis.[10] Antibiotic resistance in *Mtb* is known to arise spontaneously (acquired resistance) as mutations in the bacterial genome develop. When patients with active disease caused by initially drug-susceptible *Mtb* receive treatment, drug-resistant populations of *Mycobacteria* can 'selectively' arise and prevail over the others. These drug-resistant strains can now infect an individual that has never received anti-TB treatment and cause MDR-TB (transmitted resistance).[10,12]

Recommended treatment for drug-susceptible tuberculosis involves a 6-month course of a cocktail of four first-line antibiotics; isoniazid, rifampicin, ethambutol, and pyrazinamide,[2,3] which aims to eradicate *M. tuberculosis* from the human body. The treatment for MDR-TB until early 2016 was a 20-month-long course of even more toxic and expensive drugs.[3,11] Currently, a 9- to 12-month treatment regimen is being used for patients with MDR-TB that is not resistant to second-line drugs.[3,8] Existing drugs against TB target functions characteristic of actively replicating bacteria. Drugs that target more fundamental metabolic processes of bacteria could prove more effective against both active and dormant bacteria, as well as both susceptible and resistant strains.[8] With the last class of antibiotics against TB developed over 40 years ago (with the exception of bedaquiline), the need for new, safer (less toxic), and more affordable therapeutics is highlighted.[2,8,15]

1.2. The host immune response in TB

1.2.1. Early stage immune response

After the initial event of infection, some individuals exhibit active disease, while others successfully contain it and remain asymptomatic (latent TB). These people have a 5-10% chance of developing active disease, sometimes even after decades of latency.[2]

The onset of TB infection occurs when a person inhales droplets containing *Mtb*, which are dispersed when a host with active disease coughs. In the early stages of the host immune response, the area is flooded with phagocytic cells, mainly alveolar macrophages and recruited neutrophils. It is believed that macrophages and neutrophils also express antimicrobial peptides that contribute in this first line of defence (*Figure 2*). The context of this early stage activation of macrophages and neutrophils may also influence the immune response towards either active disease or latency.[1,2,16]

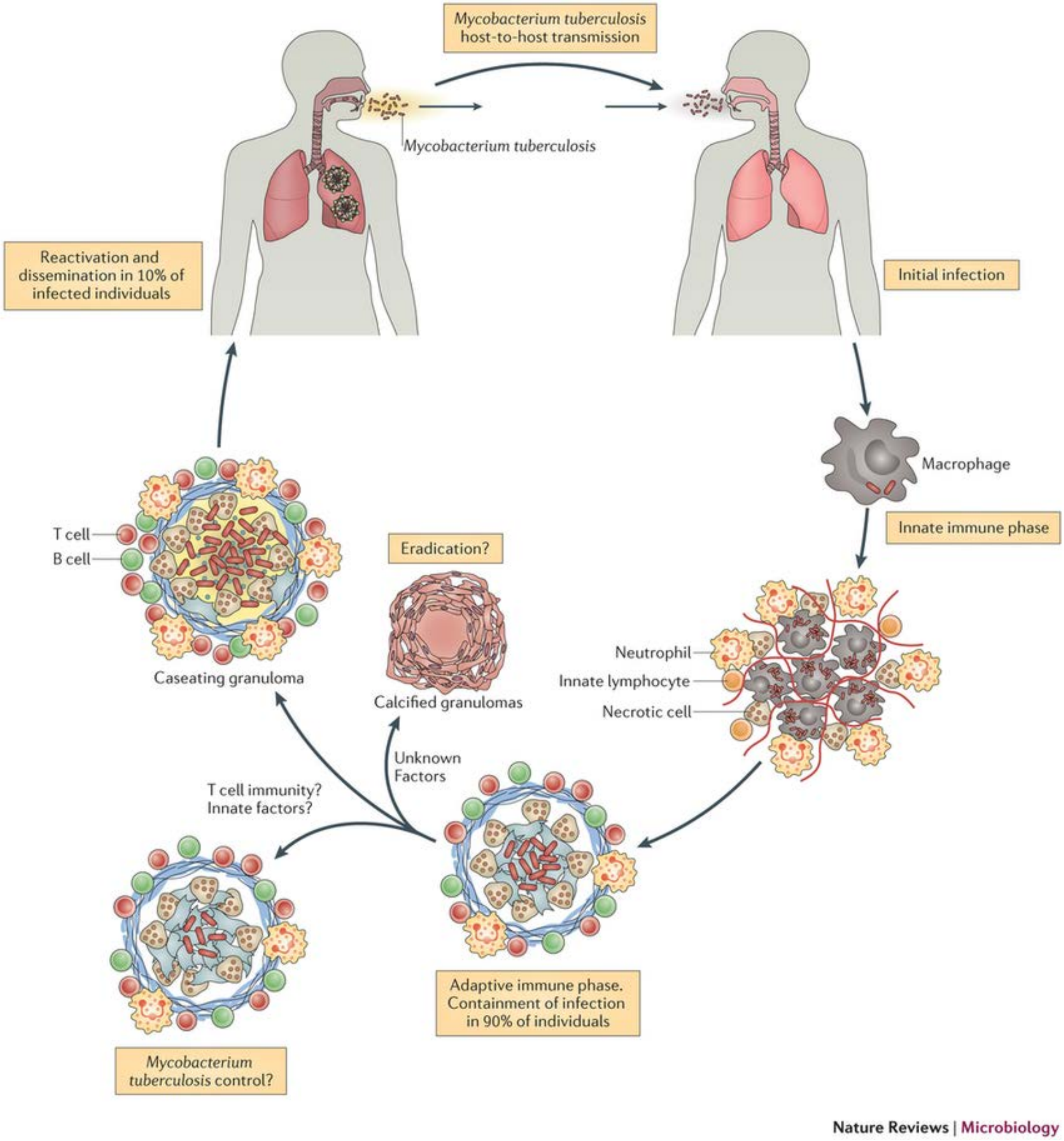

Figure 2. Life cycle of *Mycobacterium tuberculosis*.

Infection begins when a person inhales bacilli-containing droplets produced by someone with active TB who coughed. During the innate immune response stage, macrophages flood the site of infection in the lung. The second stage is the recruitment of antigen-specific T-cells, which marks the start of the adaptive immune response. B-cells, activated macrophages and other leukocytes are also recruited in the lung, which leads to the formation of a granuloma. A granuloma can stay as is and serve as containment of the infection allowing the infected individual to remain in a ‘latent’ state. In around 10% of infected people, bacteria will escape the granulomas that erupt in the airways and cause active disease and infectivity to the patient.[17] This figure, however, depicts the currently established paradigm which does not describe the role of the extracellular matrix degradation in lung cavitation. It also does not show that initial infection happens at the lung bases, whereas cavitation takes place at the lung apices. Therefore, a different infection model for TB is proposed later on in an effort to include the aforementioned parameters. (*Source:* *Nunes-Alves et al., 2014*)

After the infection event and despite the rapid response of macrophages in the infection site and subsequent phagocytosis of the bacilli, the *Mycobacteria* are not eliminated. *Mtb* is capable of suppressing the formation of the phagolysosome, i.e. the fusion of the phagosome it is in, with macrophage lysosomes, which would lead to death of *Mtb*. This is done by controlling the corresponding signalling pathways of the host macrophage. However, it was shown that some *Mtb* strains can also survive by escaping from the phagosome into the cytosol, thus ensuring their survival, though this phenomenon remains highly controversial within the field.[18,19]

Macrophages that take up invading bacilli are unable to effectively destroy them, and commonly die, either by necrosis, or by apoptosis ('programmed cell death'). This is an important distinction, since it seems that higher rates of apoptosis in macrophages have been linked to diminished pathogen viability and enhanced immunity.[2] It appears that more virulent strains of *Mtb* cause necrosis to infected macrophages, using the damaged cell membrane as a means of escape from the macrophage. However, apoptosis keeps the membrane intact, and the apoptotic macrophage becomes a target for healthy macrophages that in turn phagocytose it, further isolating it and subsequently lysing it, also killing *Mtb* in the process.[20,21] This is further supported by evidence that *Mtb* suppresses the expression of the Fas receptor, whose downstream signalling cascade activates the extrinsic apoptosis pathway,[22] in infected macrophages.[23]

1.2.2. Granuloma formation

One of the most significant pathophysiological hallmarks of tuberculosis is the formation of tuberculous granulomas. In fact, tuberculosis is the most frequent cause of granuloma formation, and the association between the two was suspected as far back as 1679.[24] Granulomas are discreet, compact structures comprised mainly of mature macrophages, and have historically been thought of as protective structures that compartmentalise pathogens in order to protect the host.[25] This observation is supported by evidence that, in some diseases, failure of the host to produce granulomas is linked to higher lethality, as is the case in *Schistosoma mansoni* infection.[26] In the same paper, Sandor *et al.* list a few examples justifying the viewpoint that granulomas are protective also in human tuberculosis. For instance, class II deficient or anti-TNF-α (Tumour Necrosis Factor α) mice, which show reduced granuloma formation, also exhibit weakened protection against infection. Meanwhile, immunodeficiencies in humans that interfere with effective granuloma formation also allow for uncontrollable proliferation and dissemination of bacteria.[26]

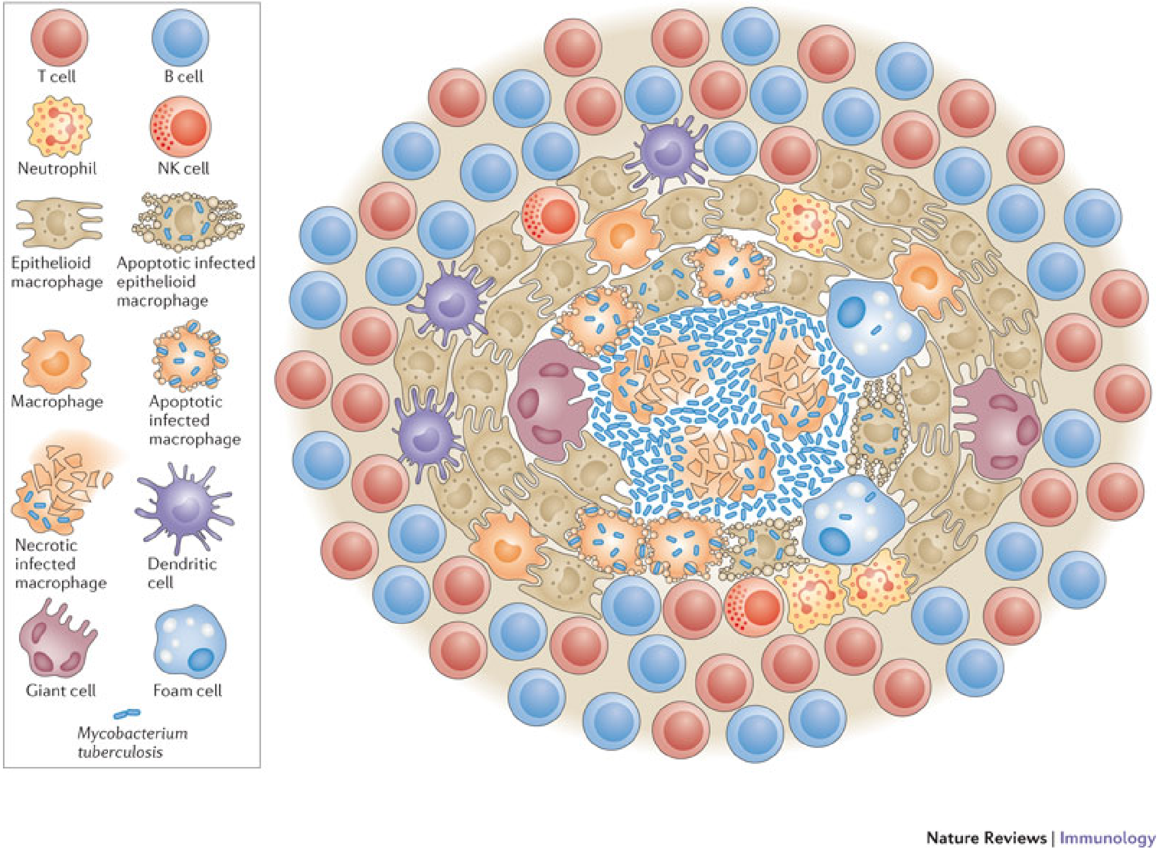

Figure 3. The cellular structure of a caseous granuloma.

The centre of the granuloma is composed of epithelioid macrophages, that can phagocytose bacteria. Some macrophages will fuse and form multinucleated giant cells or accumulate lipids and differentiate into foamy macrophages. They are usually found around the centre of a mature tuberculous granuloma. Other cell types participate in granuloma formation as well, such as T- and B-cells, neutrophils, dendritic cells, Natural Killer (NK) cells, and fibroblasts. (*Source: Ramakrishan, 2012*)[25]

However, not everyone agrees as to the protective role of granulomas in TB, and some even claim the exact opposite. A study (as well as additional studies referenced in that paper) involving *Mycobacterium marinum,* whose infection model in zebrafish closely resembles human TB, suggests that granuloma formation is beneficial to the bacteria, and aids in their growth and dissemination.[27]

Whether the role of human granulomas in TB is mostly protective for the host or the pathogen is yet to be determined; however, their structure is very well defined. Their centre is composed of *Mtb*-infected macrophages, multinucleated giant cells (MGCs), epithelioid cells, foamy macrophages, and neutrophils. This is then surrounded by a layer of lymphocytes (mainly CD4$^+$ T-cells, but also CD8$^+$ T-cells and B-cells) and fibroblasts, known as the 'lymphocytic cuff'.[2,28,29] Additionally, B-cell clusters have been observed to form within human lung granulomatous tissue, however, their function is unknown.[30]

The centre of the granuloma gradually evolves into a caseating area, which is thought to happen due to cell necrosis. It has been shown that *Mycobacteria* can not only survive in the hypoxic centre of the granuloma and its periphery, but also further away in seemingly healthy parenchyma[2] (*Figure 3*). The caseum is so named because of its cheese-like appearance on gross examination and seems to be formed due to a specialised type of necrosis, in which cell degradation is dominant relative to enzymatic cleavage. It is further distinguished into hard caseum (relatively poor in bacteria) and soft caseum (very rich in bacteria).[25]

1.2.3. Foamy macrophages and lipid metabolism in TB

Mature macrophages that participate in the formation of a tuberculous granuloma can differentiate into a variety of sub-types.[31,32] Epithelioid macrophages are one such sub-type that is characterised by zipper-like outlines. They serve to link adjacent cells in the granuloma by macrophage-macrophage adherens junctions, desmosomes and tight junctions.[33] Macrophages can also fuse and form multinucleated giant cells (MGCs)[25] which are characterised by reduced phagocytosis but conserved antigen-presentation ability. From a phenotypical point-of-view, MGCs appear to be responsible for digesting *Mtb* bacilli that were previously phagocytosed by the individual macrophages that fused to create the MGC.[34] Some granuloma macrophages accumulate lipid droplets (or lipid bodies) and differentiate into foamy macrophages.[25]

Foamy macrophages are usually found around the necrotic centre of a tuberculous granuloma. They have reduced bactericidal activity and possibly serve as a reservoir of non-replicating ('dormant') *Mycobacteria* that were phagocytosed prior to the differentiation of the macrophage into a foamy macrophage phenotype[32] (*Figure 4*). In latent TB, *Mtb* bacilli residing in foamy macrophages utilise host lipids stored in the form of lipid bodies (LBs) and form intracytoplasmic lipid inclusions (ILIs). Lipid bodies contained within foamy macrophages in pulmonary TB accumulate triacylglycerides (TAGs) preferentially over cholesteryl esters and this is disease-specific as lipid contents and formation mechanisms of LBs are different in TB from these occurring in atherosclerosis.[35] In a study by Caire-Brändli *et al* it was shown that host-derived TAGs seemed to be essential for ILI formation in *M. avium* bacilli.[36] The presence of ILIs in *Mtb* bacilli cytoplasm is considered as one of the hallmarks of dormancy.[37,38]

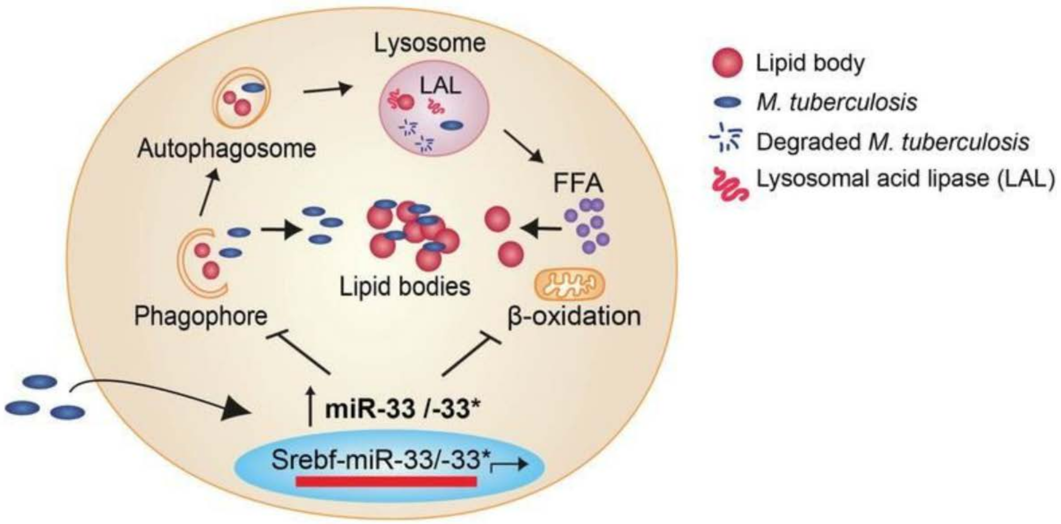

Figure 4. A proposed model for how phagocytosed *Mtb* bacilli enhance their survival in host macrophages by repressing autophagy and fatty acid oxidation.
Infection with *Mtb* induced expression of the microRNA miR-33 and its passenger strand miR33* in mouse macrophages (with similar results in human macrophages). The miR-33 molecule was found to block fatty acid oxidation resulting in a nutrient-rich lipid niche for bacilli escaping xenophagy. (*Source: Ouimet et al., 2016*)[39]

Another hallmark of tuberculosis infection is the formation of cavities in the lungs. They form when lung tissue liquefies, allowing bacteria to exit macrophages and make their dissemination by coughing of the host much easier. It is generally accepted that these cavities form by liquefaction of the caseum in the centre of granulomas.[40-44]

1.3. Extracellular matrix destruction in TB

For the purposes of this thesis, the focus is on collagen, one of the components of the extracellular matrix (ECM). There are at least 16 types of collagen in existence, of which type I, II and III account for 80 to 90% of the total amount of collagen in the human body, and are encountered in the form of thin fibrils.[45] Fibrillar collagen supports the lung extracellular matrix[46] and its structure makes it highly conducive to a phenomenon called 'Second Harmonic Generation',[47] on which a label-free imaging technique that will be introduced later is based (*Second Harmonic Generation (SHG)*).

Collagen I interacts with cells by binding to their surface through a number of different cell membrane receptors; it binds to integrins that are responsible for cell adhesion,[48] the discoidin domain receptors (DDR)1 and DDR2 that exhibit tyrosine kinase activity,[49] glycoprotein VI (GPVI) that is expressed in platelets and promotes their aggregation[50] and the leukocyte-associated immunoglobulin-like receptor 1 (LAIR-1) (or CD305) which inhibits immune cell activation *in vitro*.[51] The extracellular matrix is the non-cellular component of any given tissue, and it is composed of collagen, laminins and elastins. It not only acts as a scaffold for the cells, but also helps in the initiation of biophysical events that play a role in tissue morphogenesis, differentiation, and homeostasis. The importance of the existence of an ECM is evident, since a number of syndromes arise when there are genetic abnormalities in its components.[52] These can range from mild to severe, and include osteogenesis imperfecta (mutations in type I collagen which result in bone fragility and skeletal deformity)[53], Ehlers-Danlos syndrome (abnormalities in type I, III or V collagen that manifest with symptoms such as hypermobility of the joints, easy bruising and skin hyperextensibility and fragility among others),[54] Marfan's syndrome (deficiency in fibrillin-1 affecting primarily the cardiovascular and musculoskeletal systems with additional pulmonary and ophthalmologic symptoms)[55] and other genetic disorders. Furthermore, it also exhibits noticeable changes as a consequence of other diseases, like coronary heart disease, chronic obstructive pulmonary disease (COPD) and liver cirrhosis.[56] In the lung, the intrinsic stiffness, molecular composition, and dimensionality of ECM components contribute to its normal function, whereas pathological changes to the ECM may arise prior to cellular response and may be a sign of disease progression.[57]

This is also the case in tuberculosis, where ECM destruction leads to cavitation of the lung, which is critical for dissemination of the bacillus.[42] Given that matrix metalloproteinases (MMPs) are the only enzymes that can cleave collagen fibrils[58] which support the lung,[46] they are undoubtedly a target when investigating ECM destruction. Matrix metalloproteinases (also 'matrixins') are proteins that specialise in the digestion of ECM components. Currently, 23 genes that encode different MMPs have been identified in humans. Additionally, to avoid consequences from unregulated MMP activity, they are tightly controlled both in the transcription level and activation of pre-enzymes, but also by secretion of endogenous inhibitors, called Tissue Inhibitors of MetalloProteinases (TIMPs).[59]

Since upregulation of MMP production and activation is a logical assumption when considering lung cavitation in TB, research has been done to test this hypothesis. Indeed, mouse model studies of pulmonary TB support the notion that tuberculosis infection causes a differential MMP activation relative to controls.[41,60] In humans, MMP-1, a collagenase, is of particular interest, and is emerging as the primary disruptor of the collagen network, and also as having a central role in ECM destruction as a consequence of TB.[61] It has been shown to be upregulated in patients with TB[62] and also exhibits a correlation with higher patient severity scores, as well as a decrease in its levels in patient sputum after treatment.[63] It was also demonstrated that human macrophages secrete MMP-1 after phagocytosing live *Mtb* but not after phagocytosis of inert latex beads, which suggests that secretion of MMP is not due to the act of phagocytosis *per se,* but due to influence of the bacilli.[64]

Another study found that incubating peripheral blood monocytes with lipoarabinomannan (LAM), the major antigenic cell wall component in *Mtb*, induced the transcription of MMP-1

RNA.[65] Additionally, MMP-1 expression seems to positively correlate with increased TNF-α production due to tuberculosis infection, as a result of a signalling cascade originating from the Toll-like receptor-2 (TLR2).[66] Finally, our group in Medicine has shown that MMP-1 secretion precedes caseous necrosis in the centre of granulomas.[1] According to the current paradigm in TB immunopathology, necrotic *Mtb*-infected macrophages form a caseum at the centre of the granuloma. This tuberculous granuloma eventually erodes into an airway, leaving behind a cavity in the lung tissue. This model, however, completely overlooks the role of extracellular matrix degradation in the pathology of human TB. Thus, our group in Medicine has proposed that while cell necrosis causes caseous accumulation, the destruction of ECM by protease activity is what drives lung cavitation and consequently *Mtb* transmission[1,67] (*Figure 5*).

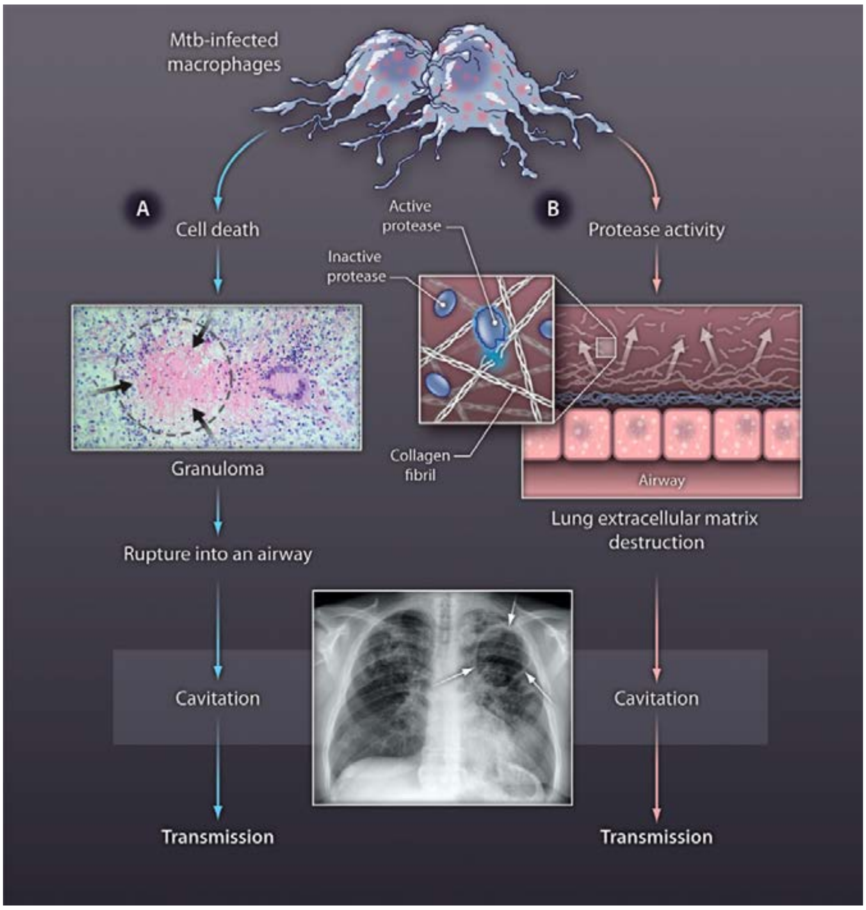

Figure 5. A proposed model of lung cavitation that contradicts the prevailing paradigm. (**A**) The **blue** arrows show the current paradigm of TB immunopathology. Infected macrophages necrotise and cause caseum formation at the granuloma centre (**black** arrows). The granuloma eventually ruptures into an airway and a cavity forms in the lung tissue (white arrows). However, this model does not take into account ECM degradation that is known to occur and its role in TB immunopathology. (**B**) Therefore, our research team propose that, while caseous necrosis occurs, there is also a parallel activation of proteolytic mechanisms to degrade the ECM (**pink** arrows), resulting in cavitation and *Mtb* transmission. (*Source: Elkington et al., 2011. Reprinted with permission from AAAS.*)[67]

For a more detailed investigation into the mechanisms involved in each stage of the disease process and to address the fundamental mechanistic processes of disease, experimental disease models are essential.

1.4. The experimental models of *Mtb* infection

1.4.1. Animal models

Human pathology of TB can range from active disease to a very heterogeneous spectrum of latent disease. However, neither this broad variety of TB pathology nor all of the individual characteristics of each stage (e.g. cavitation) have been observed in any single one of the animal models available (e.g. mouse, zebrafish, rabbit, guinea pig, and non-human primates).[2,68-70] Another limitation of using animal models is that the early immune processes that guide granuloma formation cannot be studied, since only mature and highly differentiated granulomas are accessible.[70]

The mouse is the most commonly used animal model in immunological studies of TB, as the tools and reagents necessary to study its immune response to pathogens are readily available. Many of the characteristics of human active TB can also be found in mice. Nevertheless, TB disease in mice lacks some of the disease hallmarks that exist in humans. Apart from the broad spectrum of latent disease, which does not exist in mice, other differences from human TB include poor organisation of granulomas, the absence of hypoxia in the centre of granulomas, as well as the fact that all mice eventually die from the *Mtb* infection,[2,15] as they maintain relatively high bacillary load in their lungs.[68] Other mouse models have also been developed, that are more susceptible to infection with *Mtb* and exhibit lung pathology more similar to the one reported in human TB lesions.[2]

In a zebrafish model of *Mycobacterium marinum* infection, it has been shown that phagocytosed *Mycobacteria* can attract macrophages to early stage granulomas, which can in turn leave the granuloma after becoming infected. This process could be exploited by the bacteria to spread the infection.[2] The zebrafish model has provided useful information about the mechanisms involved in the innate immune phase of *Mtb* infection in humans and how bacteria use the granuloma to disseminate.[15,27] The major advantage of the zebrafish larva as an animal model is its transparency which allows for *in vivo* microscopy studies with fluorescent probes and monitoring of the different processes from early to late disease stages. However, zebrafish larvae do not have T-cells and therefore the adaptive immune response cannot be studied.[71]

Another animal model that has been proven useful in the study of TB is the rabbit. Controlled latent infection can be observed, which can be re-activated following immunosuppression. Re-activation cannot occur spontaneously unlike in human TB.[2,69,72] As for active disease, cavitation can also be observed in the rabbit and is characterised by caseation and similar lung histopathology as in human disease.[2,72] A problem with most animal models of human TB is that they cannot achieve full bacterial clearance in the lungs, in contrast to humans. A study by Subbian *et al*. characterised a rabbit model that successfully exhibited spontaneous pulmonary clearance of *Mtb* infection and pathophysiological characteristics when infected with the *Mtb* strain CDC1551. This containment is also observed in almost 90% of *Mtb*-infected individuals.[68]

Larger animals such as different types of cattle have been used before as animal models for testing mycobacterial antigens for use as prophylactic vaccines in humans. The cattle's advantages as an animal model include ease of extracting large volumes of blood for example at different times after vaccination, as well as their similarities to human TB such as their immune response to *Mycobacteria*, which is comparable to the one in humans.[73] However, being ruminants, their physiology is different to the human one and their TB lesions do not develop cavitation.[73]

As an alternative large animal model for TB, a swine model has been introduced, which presents TB lesions very similar to human lesions. In a study by Gil *et al*., it was shown that the minipig can control *Mtb* infection by initiating a strong Th1 immune response. By encapsulating the granuloma in a fibrotic 'shell' which limits dissemination and causes necrosis to occur in the centre of the granuloma, and by its calcification the non-replicating mycobacteria are prevented from escaping the tuberculous lesion.[15]

Guinea pigs have been used as a model for human TB in studies of *Mtb* airborne transmission and efficacy of vaccines as they are very susceptible to infection with low doses of *Mtb*.[69,72] Furthermore, their immune response to *Mtb* infection bears many similarities to the human immune response. Granulocytes and eosinophils flood the site of infection followed by macrophages and lymphocytes, which ultimately form a tuberculous granuloma.[2] Hypoxic, necrotic granulomas and strong fibrosis have also been observed in guinea pigs. Possibly in an attempt to minimise bacterial dissemination and the chance of a rapid death, guinea pigs show a strong immune response at their hilar lymph nodes.[15] However, guinea pigs all develop rapidly progressing disease and die, unlike humans who usually contain infection.

The animal model that comes the closest to replicating the broad range of latency seen in humans is the non-human primate (e.g. the cynomolgus macaque). It also develops caseous hypoxic granulomas, similar to the ones observed in active human disease, as well as two other types of granulomas; the non-necrotising granuloma, which has a centre of macrophages and neutrophils surrounded by lymphocytes, and the suppurative granuloma with a neutrophil core surrounded by macrophages and MGCs with an additional outer layer of lymphocytes. The reasons for the macaques' limited use in TB research are mainly their cost, ethical concerns, and lack of the variety of tools necessary to study their immune response to *Mtb*.[2]

It is therefore evident that while every animal model offers some unique advantages to the study of TB, it also exhibits significant differences from the pathophysiology of human TB, which means that none of them alone suffices to elucidate the mechanisms of disease.

1.4.2. 2D cell culture models of TB

In cellular modelling, standard two-dimensional (2D) cell cultures have also been used as an *in vitro* model for human tuberculosis. *Mycobacteria* are quite difficult to maintain in culture, since they require a highly nutritious environment (Middlebrook 7H9 broth enriched with nutrients such as glycerol, oleic acid, albumin and dextrose) and a great deal of time to grow in culture. Notoriously, *Mycobacterium leprae* has not yet been successfully cultivated *in vitro.*[74] It is possible to shorten the culture time of *Mtb*, but extensive and tight control of a number of conditions is necessary for that to occur. The researchers achieved a reduction of 40% in *Mtb* culture time by varying the pH of the culture medium, the relative concentrations of the culture medium components and the atmosphere.[75]

However, we believe that the lack of a three-dimensional (3D) microenvironment in this traditional model is not capable of capturing all the characteristics of the disease, such as the complex 3D structure of the granulomas. Therefore, a 3D cell culture model is much needed to better understand the steps involved in tuberculosis infection.

3D Modelling VS 2D modelling

In recent years, there has been a gradual but constant shift in biomedical research from the classical 2D cell culture models towards 3D ones[76-79] (*Figure 6*). The main reason behind that shift is that, as it has been outlined above, 2D cell cultures are unable to mimic the conditions of the cell microenvironment *in vivo* and thus produce potentially misleading results regarding cell functions such as gene expression, survival and signalling pathway activation, to name a few.[77-79] In the 3D cell culture model that incorporates the extracellular matrix into the culture, cell-cell and cell-ECM communication as well as ECM destruction can be studied and this can provide researchers with more physiologically relevant results.[76,77,80]

Cells cultured in a 2D environment sense mechanical pressure only from their basal surface, whereas cells in a 3D culture sense multi-directional mechanical stresses, since their whole surface is in direct contact with the ECM which provides these mechanical stimuli.[81] What is more, traditional 2D culture is done on plastic or glass, both of which differ from live tissues in terms of stiffness, a factor that seems to have an effect on cell adhesion, morphogenesis, and stem cell differentiation. Additionally, in contrast to 2D cultures, tissues also commonly experience active mechanical forces that cause temporary cell deformation, thereby influencing their behaviour.[79]

Another difference between the two models is relevant to the diffusion of soluble molecules. In a 2D cell culture, they diffuse freely and are therefore distributed rapidly. In contrast, in a 3D cell culture, large molecules will be kept in the direct proximity of the cell by components of the ECM, that slow diffusion down significantly by binding them.[81] Furthermore, the ECM in live 3D environments commonly contributes to the appearance of effector molecule gradients. This can be emulated in 2D cell cultures, but it is difficult to maintain for the hours (or sometimes days) that are necessary for some physiological processes, such as embryonic gastrulation or blood vessel sprouting in angiogenesis to take place. For instance, the low solubility of oxygen in aqueous solutions can give rise to gradients that sharply separate areas of live cells from regions that exhibit hypoxia or cell death. Strikingly, the ECM can even actively sequester soluble factors that are only released in a tightly controlled fashion, such as proteolysis of the matrix or mechanical stresses caused by the cells themselves.[79]

The three-dimensional configuration of the extracellular matrix also influences cell migration. In 2D cell cultures, cells migrate in a well-defined manner; first extending their anterior edge, then forming adhesive interactions with the substrate, and finally retracting the posterior edge. This is in contrast to their behaviour in a 3D setting where the sequence of events is much less clear, a difference that is highlighted by the occasional need for proteolytic degradation of the ECM, or the need to squeeze through pores. Needless to say, those needs arise due to the anisotropic and fibrous nature of the ECM, which is in stark contrast to the uniformity of surfaces in typical 2D cell cultures.[79]

Other cell properties that appear different in 2D or 3D cell culture models include cell proliferation and rearrangement, gene expression, cytoskeletal organisation, and signalling pathway activation.[77,78,81,82]

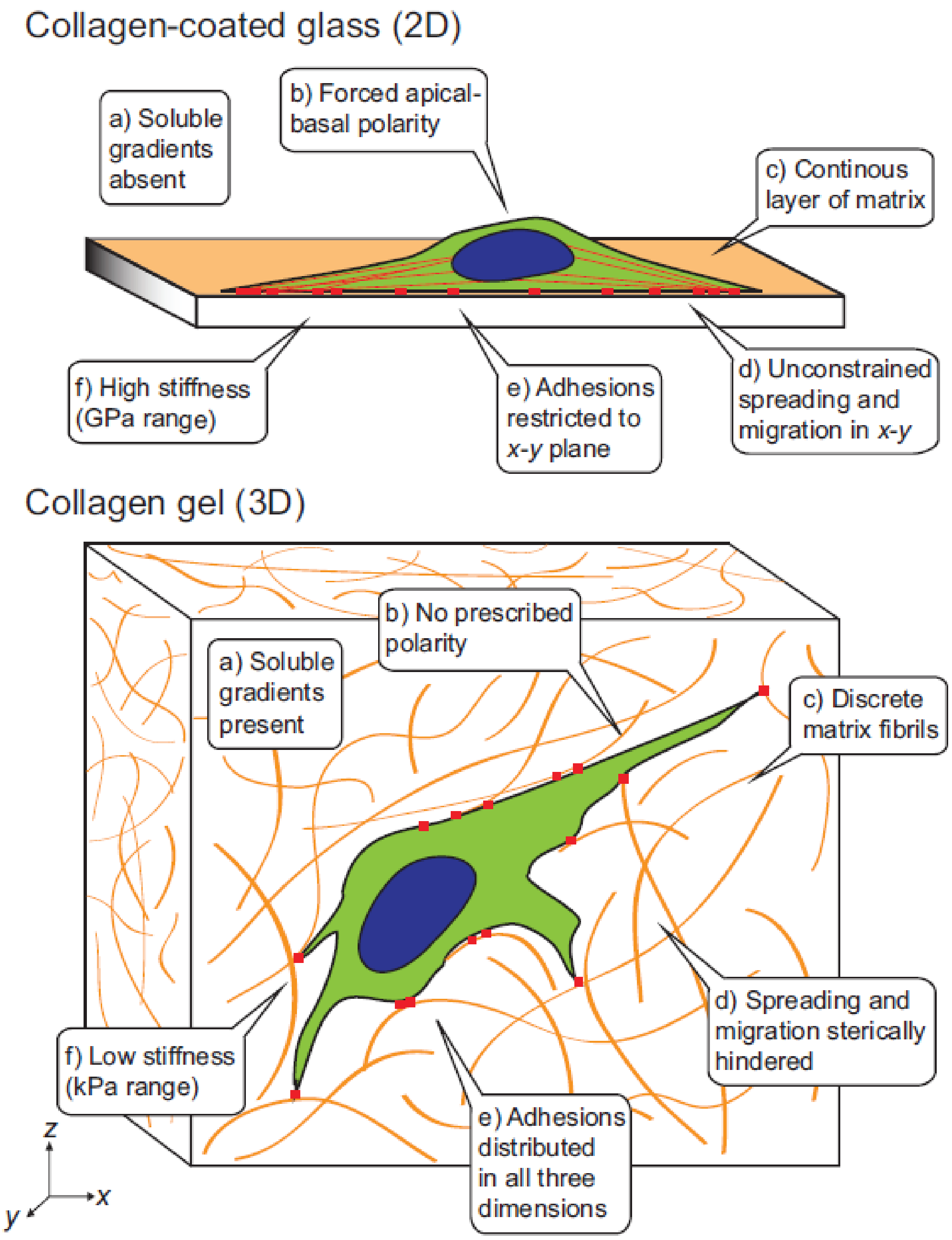

Figure 6. The environmental signals a cell receives differ between a 2D and a 3D culture. Differences between a 2D and a 3D ECM include the presence of soluble gradients, a distribution of matrix fibrils (e.g. collagen) in the 3D space that resembles the *in vivo* state and adhesion of the cell in all directions in the 3D space. (*Source: Baker et al., 2012*)[79]

Type I collagen has been shown to improve host-cell survival when added to the culture medium, and that effect is more prominent in the 3D than in the 2D cell culture model.[1] In general, cell behaviour and features are closer to the natural *in vivo* condition when they are cultured in a 3D environment as opposed to when they are cultured in two dimensions. By adding either natural or synthetic polymers in the medium, one can control the porosity, permeability, and mechanical stability of the cell matrix in a way that resembles the natural ECM *in vivo*. This provides the cells with a dynamic environment where they can proliferate, differentiate and interact with one another.[76]

1.5. 3D Cell culture models for human disease

In order to mimic the 3D configuration of the ECM, it is necessary to provide the cells with some kind of support and this can be done in a number of ways. One such way is the use of filter well inserts, devices that introduce a filter in the culture, and allow for cells to be grown on either side of it. In this way, we can assess cell communication and migration through the filter membrane. Another method requires the construction of soft gels or sponge-like scaffolds, that are made of purified extracellular matrix components, like collagen, laminin or gelatin, and then seeding the cells in these scaffolds.[83] Additionally, it is possible to make cells form small spheroids instead of monolayers, as is the case when culturing them in suspended droplets which allow the cells to aggregate in 3D space.[84] There have also been advances in techniques that allow for ‘cell printing’ of 3D structures by coating the cells with nanofilms and depositing them in layers, which ultimately form a tissue-like cell construct that is conducive to assays of cell behaviour and dynamics.[85]

Regardless of the method that is employed for construction of the 3D model, exploring cell behaviour in disease shows undeniable promise and it is a very logical direction for this exciting research avenue. Investigation of tumour properties is quite a popular subject, and examples include 3D models to assess migration and behaviour in breast cancer cell lines,[86] intracellular signalling and crosstalk to discover potential targets for intervention,[87] and marketed cancer drug efficacy in 3D models.[88]

It goes without saying that the study of cancer is not the only avenue being explored. A search into the literature revealed that 3D cell culture methods have also been employed in the study of drug candidate toxicity assessment,[89] atopic dermatitis (a chronic inflammatory condition)[90] and Alzheimer’s disease[91] among others.

1.6. A bioelectrospray-generated 3D cell culture model for TB

Our team in the Faculty of Medicine is also advocating the use of 3D models for the study of tuberculosis, and that is why members of our group developed a new 3D cell culture model. It involves the use of a bioelectrosprayer to generate spherical 3D cell cultures, ‘microspheres’, each one of which has a 500-600 μm diameter (*Figure 7*). In the experiments included in this thesis, the diameter of microspheres produced was measured to be 0.9-1 mm. An alginate gel is pushed through a syringe to the bioelectrosprayer by a syringe driver. Droplets form on the needle tip and then fall into a crosslinking $CaCl_2$ bath, where they turn into microspheres. Falling of alginate droplets inside the bath does not occur only because of gravity, but is also accelerated by the electric field that is created between the tip of the needle and the crosslinking bath, thereby controlling microsphere size.[77]

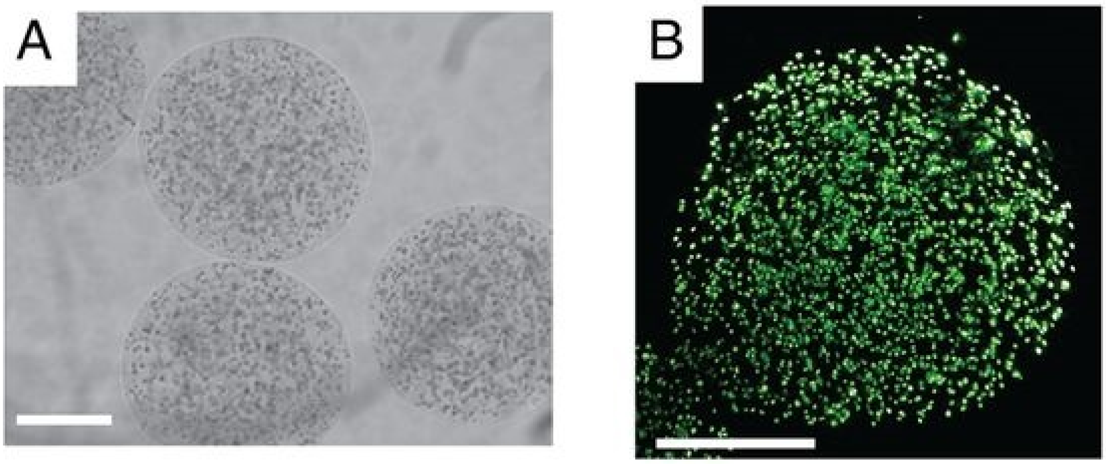

Figure 7. 3D Cell culture produced by bioelectrospray.
(**A**) Microspheres containing peripheral blood mononuclear cells (PBMCs) infected with *Mycobacterium tuberculosis* in an alginate gel generated by bioelectrospraying and imaged right away with a light microscope. (**B**) Live PBMCs stained with calcein (green fluorescence) are distributed evenly within the microsphere. Both scale bars correspond to 250 μm. (*Source: Al Shammari et al., 2015*)[1]

Sodium alginate is a naturally occurring, linear, unbranched polysaccharide produced by certain species of brown algae[92,93] (e.g. *Laminaria japonica*).[94] It is a 1,4-linked copolymer of varying ratios of two subunits; α-L-guluronic acid (G) and β-D-mannuronic acid (M) and typically has a molecular weight of approximately 100 kiloDalton (kDa) although it can vary greatly. These two subunits are organised in two types of homopolymeric (MM, GG) blocks and a heteropolymeric (MG) block.[92,93] When sodium alginate interacts with Ca^{2+} ions (especially the G-rich areas), different strands crosslink and form a 3D network-like structure. Due to its potential to form a hydrogel, it is widely used as a matrix material for various applications.[92]

Collagen is the most abundant protein in mammals and a constituent of the ECM and connective tissue, and therefore an important component of a 3D cell culture matrix.[45] The fundamental form of type I collagen is tropocollagen that consists of three coiled subunits, two α_1 and one α_2 chains, intertwined together in a triple helix. Collagen molecules have a diameter of 1.5 nm, while collagen fibrils (which contain approximately 500 individual collagen molecules) have a diameter of 30-50 nm. In tissues, collagen fibrils tend to be loosely distributed, leaving spaces of approximately 100 nm between them.[95]

A very common tool for imaging collagen within tissues is staining with the Sirius red dye. This is a linear, polar molecule that is both coloured and fluorescent and can enhance the birefringence of the fibrils, without affecting the nonlinear optical properties of collagen that render it capable of producing a Second Harmonic Generation (SHG) signal.[95,96]

Properties of the 3D microenvironment such as its chemical composition, internal architecture and stiffness can affect the way cells cultured in it behave and function.[82] Various parameters affecting microsphere size and cell viability have been investigated. These included voltage, flow rate and nozzle size, as well as gel strength when using different types of alginate and the addition of collagen to the gel. Larger inner diameter of the needle produces larger microspheres. Application of higher voltage creates microspheres smaller in diameter until a “critical voltage” beyond which microspheres do not shrink any further. Different solvents seemed to have different effects on the size of the microspheres and in the end, Hank’s Balanced Salt Solution (HBSS) was selected as a solvent that is not toxic to the cells and does not significantly affect microsphere size.[77]

The microsphere model shows great promise and our group’s latest publications highlight that. Specifically, Tezera *et al.* showed that known characteristics of TB infection manifest in our 3D cell culture model, and then investigated the host immune response to tuberculosis infection, with an emphasis on elucidating the role of individual cytokines. They also found that the addition of type I collagen in the matrix significantly improved host-cell survival as well as the ability of host PBMCs to control *Mtb* proliferation in the microspheres. It increased host-cell apoptosis, considered to be a mechanism for protection of the host and positively affected secretion of several pro-inflammatory cytokines (including IL1-β, TNF-α, IFN-γ, IL-6, IL-8 and MCP-1). Additionally, Tezera *et al*. investigated the potential of host-directed therapies and augmentation of the immune response with *ex vivo* cultured antigen-specific T cells.[97]

In another publication, Bielecka *et al.* tackled the highly relevant and urgent problem of antibiotic resistance in tuberculosis. They used the microsphere model to investigate the efficacy of standard antibiotics in a number of settings, and also employed microfluidics to mimic the *in vivo* pharmacokinetics of drugs, since their concentration in patient tissues fluctuates over time, contrary to the steady concentrations used in the laboratory. One of the most interesting findings of this paper was that pyrazinamide, an antibiotic used to treat human TB, was shown to be effective against *Mtb* in the microsphere model, consistent with what is reported in patients whereas it seems ineffective in killing *Mtb* in 2D cell cultures and Middlebrook 7H9 broth. These results highlight the potential of this system to be used as a drug-screening platform. Standard antibiotics such as isoniazid, rifampin and ethambutol successfully killed *Mtb* in all three culturing conditions. Isoniazid was shown to be more efficient in the microsphere 3D model rather than the 2D cell culture. Second-line antibiotics used in drug-resistant infections, such as linezolid, moxifloxacin and D-cycloserine tended to be most efficacious in the microspheres than the other two cell culture systems.[98]

Up until now, our bioelectrospray-engineered 3D cell culture model has been studied with traditional microscopic imaging techniques mainly based on fluorescence,[1,97] but despite their advantages (high sensitivity and 3D resolution, induced gene expression of fluorescent proteins) these techniques also have limitations. These include the requirement for sample preparation, fixation, and sometimes sectioning (time-consuming, invasive, destructive),[82,99] as well as the fact that fluorescent staining is difficult to use *in vivo*. These limitations can be overcome by a set of imaging methods, collectively called label-free techniques, which provide 'chemical imaging',[99] as they can detect molecular vibrations[100] or structural anisotropy.[101] These methods have the ability to clearly distinguish between different molecules, as each molecule gives off a 'fingerprint' Raman scattering signal[100] and can detect structures of non-centrosymmetric molecules such as collagen fibrils.[101]

1.7. Label-free imaging techniques

Label-free imaging techniques are based on either linear (e.g. Raman spectroscopy) or non-linear (e.g. Coherent Anti-Stokes Raman Scattering, Second Harmonic Generation, Two-Photon Excitation Fluorescence) optical phenomena and provide the user with chemical information about the sample under investigation. These techniques are being increasingly utilised in biomedical studies as they can overcome many of the major drawbacks of traditional microscopy.[102]

Their most important advantage for application on biological samples is that they are non-invasive, as there is no need for exogenous chemical labelling or sample processing before imaging.[102-104] The use of infrared (IR) and near-infrared (NIR) lasers offers greater sample penetration and less phototoxicity. Also, the lack of fluorescent labelling in the system eliminates the risk of photobleaching.[102,103,105] Other advantages of label-free imaging techniques include the ease with which measurements are acquired, their high reproducibility, and small volume of biomass necessary for the measurement to take place.[13] These techniques also permit *in vivo* use as the output of the laser power at the point of contact is quite low and with the use of NIR lasers, phototoxicity is reduced in the tissue optical transparency window which spans approximately from 700 cm^{-1} to 1300 cm^{-1}.[102,106] In this work, techniques primarily based on Raman scattering and second harmonic generation have been explored.

1.7.1. Raman Spectroscopy

Raman spectroscopy, is a non-invasive,[80,107] label-free imaging technique that can provide the user with information about chemical structure and physical form. Until now it has mainly been used for qualitative, semi-quantitative or quantitative analysis in the chemical and material sciences. It is in the last decade that it is starting to also be used for analysis of biological samples.[108] This technique is based on the phenomenon of spontaneous Raman scattering, first observed experimentally by Raman and Krishnan in 1928, which corresponds to inelastic photon scattering (i.e. that where scattered photons have a different wavelength than that of the incident light) after monochromatic light interacts with a vibrating molecule.[100,103,108,109] A Raman scattered photon might have either longer (Stokes Raman scattering) or shorter (Anti-Stokes Raman scattering) wavelength than that of the incident light.[110] In order for a molecular vibration to be 'Raman-active' there needs to be a change in polarisability occurring during the vibration[103] (*Figure 8*).

When light interacts with a molecule, the majority of the scattered photons (E) will have the same energy as the incident photons (E_0), as no energy exchange will have taken place (*Equation 1*). This phenomenon is called **Rayleigh** scattering (or elastic scattering) and is the most common form of light scattering.

$$E = E_0 \tag{1}$$

Approximately 1 in 10^7 (or 10^8) of scattered photons will lose some energy due to their interaction with the molecule and so will have a lower frequency (and a longer wavelength) than incident photons (*Equation 2*). The energy lost will be equal to the energy of one specific molecular vibration (E_v). This phenomenon is called **Stokes** Raman scattering.

$$E = E_0 - E_v \tag{2}$$

At room temperature, due to the thermal energy of the environment some molecules exist in a higher vibrational state. When photons interact inelastically with such a molecule, it is possible that energy will be transferred from the molecule to the photons (*Equation 3*). The energy transferred (E_v) is again equal to the energy of a molecular vibration, only this time the scattered photon gains energy. This process is called **anti-Stokes** Raman scattering and it occurs for even fewer of the scattered photons. Detecting anti-Stokes Raman scattered radiation is sometimes preferred over detecting Stokes scattering for the reason that the former is free from fluorescence which occurs at a lower energy (longer wavelength) than the incident.[103,108]

$$E = E_0 + E_v \tag{3}$$

At higher temperatures, even more molecules will exist in the higher vibrational states and anti-Stokes Raman scattering will be more frequent as opposed to Stokes Raman scattering. This is why the ratio of the Stokes and anti-Stokes Raman scattering intensities can be used to calculate temperature.[103]

The main parts of a standard Raman spectrometer are the light source (e.g. Ar/Kr, He:Ne, Nd:YAG, diode lasers), the monochromator, the sample holder and the detector. Longer wavelength lasers [e.g. near-infrared (NIR) lasers] tend to be preferred when the sample exhibits fluorescence that interferes with its Raman signal detection.[103]

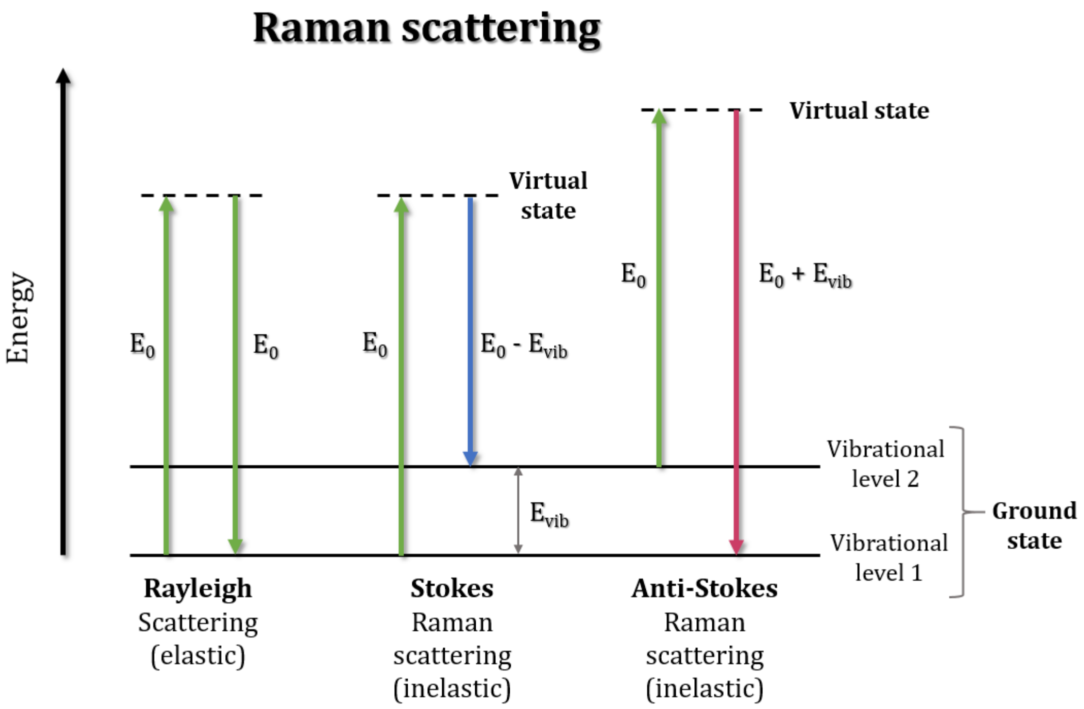

Figure 8. Raman scattering.

This phenomenon is based on the inelastic scattering of light. The incident light can lose (Stokes) or gain (anti-Stokes) energy after its interaction with molecular vibrations.

As mentioned above, only 1 in 10^7 (or 10^8) photons undergo Raman scattering so the signal produced is relatively weak.[108,110] When trying to image biological samples, where many components under investigation may exist in traces, it becomes apparent that signal enhancement is needed to successfully detect them.[100,109]

1.7.2. Coherent Anti-Stokes Raman Scattering (CARS) microscopy

One way to enhance the Raman signal is through the phenomenon of Coherent Anti-Stokes Raman Scattering, which is a four-wave mixing process. By creating coherently excited vibrational states, signals up to five orders of magnitude higher than spontaneous Raman scattering can be generated.[111] This is achieved by using two spatially and temporally overlapping excitation lasers such that the difference in frequency between them matches a vibrational frequency of molecules of interest[109,112] (*Figure 9*). The two incident monochromatic laser beams are characterised as 'pump' and 'Stokes'; the frequency of the pump beam is always higher than the frequency of the Stokes beam ($\omega_{pump} > \omega_{Stokes}$). When the difference in frequency between the two beams matches the frequency of a natural molecular vibration ($\omega_{pump} - \omega_{Stokes} = \omega_v$) there is emission of a normal Raman signal. When this system is also probed with a third laser (ω_{probe}) a strong coherent anti-Stokes Raman signal is generated at a completely new frequency (*Equation 4*).[103,113,114]

$$\omega_{CARS} = (\omega_{pump} + \omega_{probe}) - \omega_{Stokes} \tag{4}$$

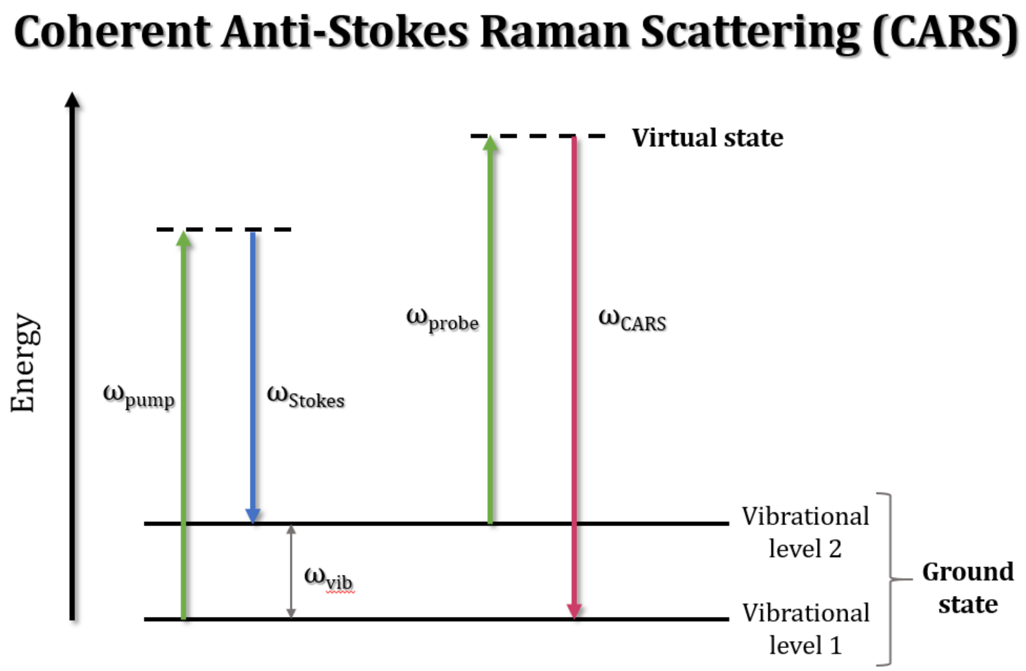

Figure 9. Coherent Anti-Stokes Raman Spectroscopy (CARS).
The difference in frequency between the pump and the Stokes laser beams corresponds to the frequency of a molecular vibration. When this vibration is probed with a third laser beam, a strong, coherent anti-Stokes Raman signal is generated.

CARS microscopy is a recently developed technique that is increasingly being applied to biomedical imaging. Since signals from molecular vibrations are probed in CARS, lipids are an ideal CARS-candidate due to the presence of a large number of CH_2 bonds. Thus most of the studies performed with CARS on biological tissues or samples are done on lipid-rich areas[100,115] (e.g. cell membranes)[82] and involve monitoring of lipid kinetics.[115] As mentioned previously, in human tuberculosis, macrophages differentiate into different types inside lung granulomas. One of these cell types is the 'foamy macrophage', that is filled with lipid-containing bodies.[32] Therefore, this cell type would be an excellent target for CARS and should provide high-contrast imaging.

1.7.3. Second Harmonic Generation (SHG)

Another label-free imaging technique usually coupled with CARS on the same optical setup is second harmonic generation microscopy. In SHG microscopy,[95] a multi-photon microscopic imaging technique,[116] the incident light propagates through the sample and causes a redistribution of internal charge.[95] After interaction of the incident photon with molecules of the sample, the detected photon is emitted with double the frequency and energy than that of the incident radiation (*Figure 10*). This transition occurs through a second-order, coherent, non-linear process.[95,104,105] What SHG imaging offers is high resolution 3D imaging, optical sectioning, deep tissue penetration (due to the use of infrared lasers), as well as significantly less phototoxicity and photobleaching compared to imaging methods using fluorescence (e.g. confocal microscopy).[104,105]

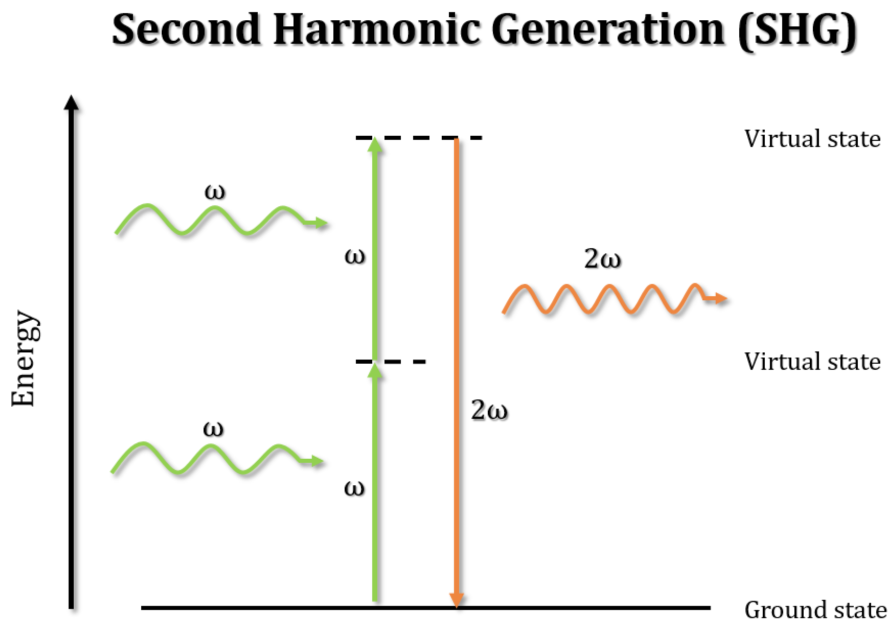

Figure 10. Second Harmonic Generation (SHG)

The detected photon has double the frequency and energy of the incident light, transformed through a coherent, non-linear process.

SHG creates optical contrast by detecting molecular orientation and structure in chiral molecules.[116] Molecules that can produce a SHG signal are non-centrosymmetric. An ideal molecular candidate for SHG is collagen[47,95] (especially types I and II)[105] which has a unique triple-helical structure and very high crystallinity.[95] However, other known extracellular matrix components like elastin and fibronectin do not have that ability, making SHG a suitable technique for selective, label-free imaging of collagen.[105] Imaging and monitoring of the ECM composition and structure is crucial in many different conditions such as diabetes and cancer.[116]

1.7.4. Two-Photon Excitation Fluorescence (TPEF)

First introduced in 1990 by Denk *et al*,[117] Two-Photon Excitation Fluorescence (TPEF) has since been routinely used for biomedical imaging. TPEF is used to excite molecular autofluorescence in a non-linear manner.[116] Detecting autofluorescence generated from excitation of molecules that are naturally in the sample (e.g. collagen, elastin etc.) is paramount when trying to discriminate between healthy and diseased tissue.[118] Most of these naturally occurring fluorophores absorb in the UV and hence are not conventionally probed, to avoid sample destruction. However, two-photon excitation overcomes this limitation. The illumination source in TPEF is a laser pulse of a very short pulse width (usually in the order of nanoseconds to femtoseconds). Two laser photons are simultaneously absorbed by a molecule, which is then excited and a single higher energy photon is emitted. Unlike SHG, energy loss occurs during this process, so the emitted photon has an energy lower than the sum of the energy of the two incident photons[117] (*Figure 11*).

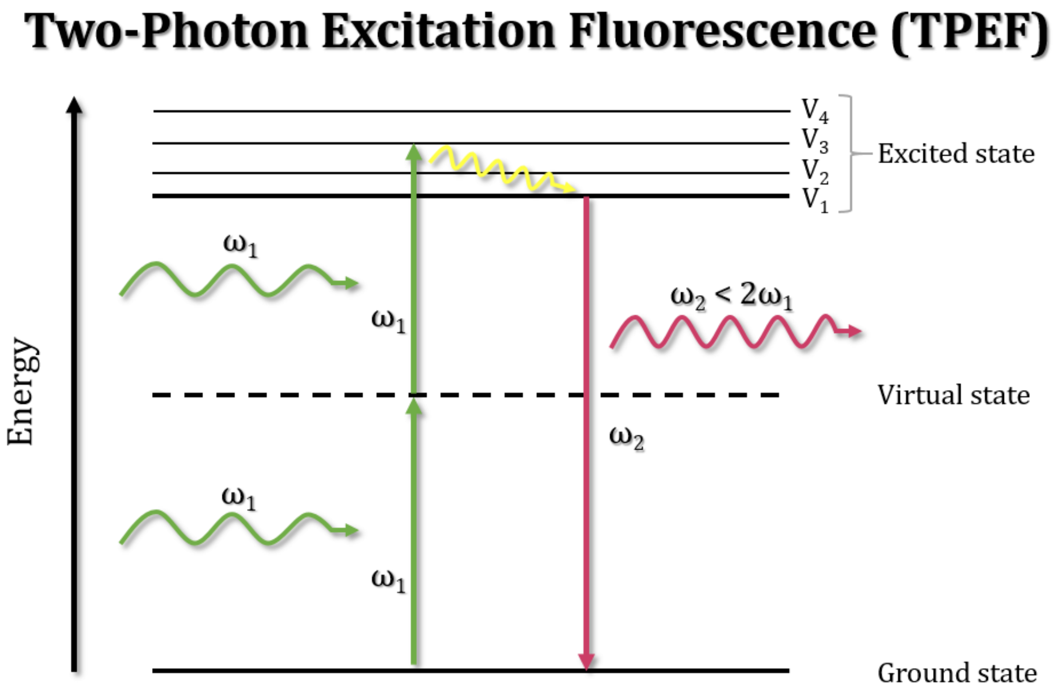

Figure 11. Two-Photon Excitation Fluorescence (TPEF).

The frequency of the emitted photon is lower than twice the frequency of the incident photon ($\omega_2 < 2\omega_1$), as there is energy loss when the photon relaxes to vibrational level 1 (V_1) from V_3 of the excited state, before its final relaxation to the ground state.

As a non-linear microscopic technique, it is inherently suitable for tissue fluorescence[119] and live-cell imaging[104] because of its greater penetration depth and lower specimen photodamage compared to single-photon-excitation confocal imaging. This technique has also been used to non-invasively obtain tissue structural information in human epidermis and dermis.[119] One of its most important limitations, however, is that extracting quantitative, molecule-specific information when doing intensity-based measurements is quite challenging, as the detected signal may be originating from more than one endogenous autofluorescent molecules of the sample.[118] Combining the two complementary techniques, TPEF and SHG, on the same setup would provide information about the cellular interaction with their microenvironment (ECM) which is of utmost importance in the pathology of various health conditions.[116]

1.8. Biomedical applications of label-free spectroscopy and imaging

Raman-based chemical imaging techniques have been applied in the biomedical field for diagnostics (e.g. cancer, microbial infection),[102,120,121] identification of different cell types or different microbial species/strains,[13,122] and skeletal regeneration studies,[123] amongst others. Second harmonic generation microscopy has served as a very valuable tool in characterising and detecting chemical and structural changes in collagen-containing matrices or tissues.[47,101] Two-Photon Excitation Fluorescence has been used in many applications in detecting the autofluorescence of components of biological samples *in vivo* with high resolution.[124,125]

One such application is in stem cell research, where a major issue is the post-transplantation proliferation of undesired stem cell phenotypes in the receiving tissue which can lead to tumour formation. Therefore, it is very important to monitor the differentiation of stem cells in a non-invasive, rapid and effective way.[102] A study by Pascut *et al.* showed that Raman spectroscopy can be used to detect the different phenotypes of cardiomyocytes derived from human embryonic stem cells (hESCs), so that desired phenotypes are selected. The different phenotypes were confirmed using immunostaining.[120] In another study by Mitchell *et al.,* the differentiation of adipose-derived stem cells (ASCs) over time was characterized using Raman spectroscopy and confirmed by quantitative Reverse-Transcription Polymerase Chain Reaction (RT-PCR). The researchers showed that biochemical changes related to adipocyte differentiation could be detected with Raman spectroscopy as early as 3 days into the process.[126] In both studies the different phenotypes in Raman spectra were defined by Principal Component Analysis (PCA).[120,126]

Furthermore, when it comes to cancer research, diagnosis of tissue malignancy in its early or precursor stages is essential for better patient outcome.[121] Additionally, defining the boundaries of a tumour to be removed is based on tissue morphology and vasculature, which is a technology-assisted (e.g. mammography) decision made by the surgeon. Quite often though, these boundaries are misjudged as cells near the tumour outline might have cancer-related biochemical changes but not exhibit any visible morphological changes.[127] Jess *et al.* applied Raman spectroscopy on normal human keratinocytes and a cervical carcinoma derived cell line (CaSki) infected with the human papilloma virus (HPV), a common cause for cervical cancer. They showed that Raman spectroscopy can distinguish not only between normal keratinocytes and CaSki cells, but also between normal and immortalized human keratinocytes. This indicates the potential of Raman spectroscopy for use in screening for HPV-associated cervical neoplasia.[121]

Moreover, Raman spectroscopy has been shown to be capable of meeting the need for a rapid and accurate method of microbial identification, since diagnosis can be significantly delayed when cell culture of a microorganism is required to identify it.[13,122] Most studies involving microbial detection are based on a different Raman-based technique, namely Surface-Enhanced Raman Spectroscopy (SERS), which offers strong signal enhancement. Studies performed on this subject include detection of bacterial cell wall changes induced by antibiotics.[128]

CARS is especially relevant for studies that revolve around kinetics or action of lipids since, as previously mentioned, lipids are highly CARS-active. One such study from Le *et al.* showed that excess of free fatty acids (FFAs) induces lipid accumulation in M109 lung cancer cells from Balb/c mice. They found a positive correlation between intracellular lipid content and cancer metastasis. Using CARS they detected lipid accumulation inside both primary and metastasized cancer cells and also revealed the presence of circulating lipid-rich tumour cells.[129]

Another field where CARS has become popular is the *in vivo* monitoring of the myelin sheath of nerves for application in various demyelinating diseases (e.g. multiple sclerosis).[125,130-133] Myelin is an excellent candidate for CARS imaging as it is mainly (~70% w/w) comprised of lipids.[131] A study by Huff *et al.* showed that CARS can be used for *in vivo* imaging of the myelin sheath in sciatic nerve tissue by making a small surgical incision to uncover the nerve. Combined with other multi-photon techniques, such as SHG, CARS has the potential to evolve into a tool for neurological studies in demyelinating neuropathies.[130] Wang *et al.* used CARS in combination with TPEF to image axon myelin *in vivo,* in live spinal cord white matter of guinea pigs and characterise the molecular orientation of myelin lipids. They showed the potential of CARS to be used in elucidating the mechanisms of demyelinating diseases without subjecting tissue to invasive sample preparation, staining, and fixing procedures.[125] While the majority of biological applications involve imaging lipids with CARS, other biomolecules such as DNA[134] and proteins[135] have also been imaged. Additionally, spectral CARS imaging can allow simultaneous imaging of different molecules without any type of labelling.[136]

SHG – either alone or in conjunction with TPEF – is currently being used relatively routinely in studies of the extracellular matrix. These techniques offer high-resolution 3D imaging of tissue.[116,124] Researchers in Japan proposed that a quantitative SHG imaging technique combined with TPEF could be utilised as a label-free diagnostic test for osteoarthritis (OA) by imaging articular cartilage. They applied the technology *ex vivo* in a mouse model for OA and successfully measured the degeneration of the components of articular cartilage.[137]

To summarise, label-free imaging is starting to be used in an array of biomedical arenas. Therefore, my interest is in combining these methodologies with a 3D cell culture model to gain new insight into the host-pathogen interaction in human TB.

1.9. Applications of label-free imaging techniques to 3D cell cultures

Raman spectroscopy has been performed on 3D cell cultures to investigate human bone growth,[138,139] co-cultures of fibroblasts with tumour cells,[140] articular cartilage,[141] mammary gland epithelial cells,[107] various cancer cell lines,[142] and other cell types.

A representative example of a label-free technique overcoming limitations of current methods is a study by Yue *et al*; in this work, a compound Raman microscope was used to investigate whether the different lipid ordering between the apical and basal membranes of breast epithelial cells in a 3D culture can serve as a tool to distinguish between these two and as a screening tool for factors that make breast epithelium more prone to cancer. Immunostaining could not overcome the variation between samples, whereas the compound microscope the group used could. It incorporates a CARS system for rapid tissue imaging and a confocal Raman spectrometer for points of particular interest in the sample. It was shown that this system could in fact be effectively used for tracking changes in the apical polarity of acini. Additionally, a disruption to the apical polarity of acini caused by the ω6 fatty acid, a breast cancer risk factor, was successfully observed using these tools.[107]

It has also been demonstrated that collagen gels can be used as a 3D environment for cells that are to be imaged with Raman spectroscopy,[82,142,143] as they provide consistent spectra and higher cell viability compared to other media.[82] A study by Bonnier *et al*. demonstrated that Raman spectroscopy can be a powerful tool for live-cell imaging in 3D cell cultures (human lung adenocarcinoma and human epithelial keratinocyte cell lines cultured in collagen gels) as well as for imaging fixed cells.[142] Another study by Brauchle *et al.* detected differences between healthy and diseased (squamous cell carcinoma) 3D *in vitro* skin models using Raman spectroscopy.[144]

In a study by Mortati *et al.* CARS and SHG were used to investigate the interaction between human mesenchymal stem cells (hMSCs) and the fibrin hydrogel 3D scaffold in which they were growing. By the simultaneous monitoring of cell morphology (using CARS) and of collagen production (using SHG) in the 3D scaffold, even after the first few hours of culture, differentiation of the hMSCs was observed.[82] Therefore, there is a growing interest in combining these label-free techniques with 3D cell culture models for human disease to achieve simultaneous monitoring of cells and their environment.

1.10. Applications of label-free imaging techniques to tuberculosis

Since the recent advancements in Raman spectroscopy instrumentation for signal enhancement, as in the case of tip-enhanced Raman spectroscopy (TERS), SERS or CARS, the techniques have been shown to be powerful tools in identifying and characterizing bacterial colonies or even single cells.[145,146] The first study that attempted to identify different *Mtb* strains as well as strains from Non-Tuberculous Mycobacterial (NTM) species using Raman spectroscopy was published in 2008 by Buijtels *et al.* in the *Journal of Clinical Microbiology*. The method achieved a fully accurate (100%) distinction between *Mtb* and NTM species (for all 63 *Mycobacterium* species), while the overall correct identification of *Mycobacterium* species was 95.2%. The most significant differences in Raman spectra of mycobacteria were based on the intensity of the 1150 cm^{-1} and 1520 cm^{-1} peaks that correspond to carotenoids. Three of these species, *Mycobacterium xenopi, M. lentiflavum* and *M. gordonae* had very intense carotenoid peaks due to their pigmentation. The researchers also showed that heat-inactivated mycobacteria did not have a substantially altered spectrum, so the technique can be used outside a Biosafety Level-3 (BSL-III) facility.[13]

Resonance Raman spectroscopy has also been used in biochemical studies to investigate the mechanisms of antibiotic resistance of *Mtb* to isoniazid (INH). KatG is a heme-containing, class I peroxidase in *Mtb* that is implicated in the activation of INH, a first-line drug for TB. Mutations in this gene have been linked with *M. tuberculosis* resistance to INH.[147,148] Kapetanaki *et al.* characterised the conformational changes that occur in the KatG heme pocket when the gene that encodes KatG is mutated.[147] Another study by Chouchane *et al.* used this method to demonstrate that there are significant mechanistic differences in the way the mycobacterial KatG and homologous peroxidases from plants or the yeast cytochrome *c* peroxidase react with substrates and peroxides. Reaction of KatG with excess of three different substrates (i.e. 3-chloroperoxybenzoic acid, peroxyacetic acid and *tert*-butylhydroperoxide) caused the formation of an intermediate form of KatG similar to the ‘Compound I’ form of its homologous horseradish peroxidase (HRP). In the presence of INH, this KatG Compound I was reduced to the ferric enzyme with no intermediate formation of Compound II being detected. This was contrary to findings regarding HRP Compound I, which was also reduced by INH but with the stable generation of HRP Compound II.[148]

To the best of my knowledge, SHG and CARS have yet to be utilised in a setting examining tuberculosis. CARS, TPEF, and SHG show potential in monitoring cell aggregation and ECM remodelling in our 3D model of human tuberculosis infection. Therefore, one of the aims of this project is to combine these novel, advanced imaging techniques with the recently developed 3D cell culture model generated by bioelectrospray to study the host-pathogen interaction in human tuberculosis.

1.11. Hypothesis

My hypothesis is that combining different emerging and traditional imaging techniques can provide new insight into the host-pathogen interaction in human TB, thereby advancing our understanding of the disease.

1.12. Objectives

- To investigate the potential of label-free spectroscopy and microscopy to characterise the microsphere model
- To gain new insight into the host-pathogen interaction in tuberculosis using traditional microscopy (TEM, SEM, confocal) on infected microspheres
- To examine a human tuberculous lung biopsy in 3D and then enrich the 3D volume with cellular and molecular information acquired by standard histology and immunohistochemistry on said biopsy

1.13. Plan of Investigation

<u>To image the 3D 'microsphere' cell culture model[77] with:</u>

- **Label-free spectroscopy/microscopy** (PBMC aggregation, changes in ECM composition)[149-152]
    - Raman spectroscopy (chemical characterisation of microsphere matrix)
    - CARS (PBMC aggregation in the microsphere)
    - SHG (collagen in the microsphere matrix)
    - TPEF (autofluorescence of microsphere matrix and PBMCs)
- **Traditional microscopy**
    - Confocal (PBMC aggregate formation)
    - Transmission Electron Microscopy (TEM) (host-pathogen interaction in TB – phagocytosed bacilli)
    - Scanning Electron Microscopy (SEM) (overview of the microsphere and texture of its matrix)
- **Micro-Computed Tomography (micro-CT)** (exact location PBMC aggregates in infected microspheres)

<u>To image a formalin-fixed paraffin-embedded (FFPE) human tuberculous lung biopsy with:</u>

- **Micro- CT** (3D non-destructive imaging of the unstained biopsy)
- **Traditional histology** (cellular and molecular information about the ECM)
    - H&E (major cell types comprising a granuloma)
    - EVG (extracellular matrix – elastin & collagen)

  - ◊ ZN (acid-fast staining for *Mtb* bacilli)

- **Immunohistochemistry** (distribution of specific immune cell types in the granuloma)
  - ◊ CD4 (helper T-cells)
  - ◊ CD8 (cytotoxic T-cells)
  - ◊ CD103 (intra-epithelial lymphocytes)
  - ◊ Granzyme B (cytotoxic activity)
  - ◊ Ki-67 (cell proliferation)
  - ◊ PD-1 (macrophages, dendritic cells)
  - ◊ PD-L1 (macrophages, dendritic cells)

Chapter 2

-

Materials & Methods

Chapter 2. Materials & Methods

2.1. Preparation of alginate suspension and alginate-collagen matrix

First, 3% w/v alginate suspension in HBSS is prepared. In a falcon tube, 1.5 g of alginate (PRONOVA UP MVG Product ♯4200106 from Novamatrix) is mixed with 50 ml of HBSS. The alginate suspension is vortexed for 3 minutes and then due to its high viscosity is left overnight in a vertical shaker at 4°C to mix well.

To prepare the alginate-collagen matrix, 0.05 M NaOH in 0.2 M 4-(2-hydroxyethyl)-1-piperazineethanesulfonic acid (HEPES), 7.5% $NaHCO_3$ (Life Technologies Cat. ♯25080-60), and human collagen ~3 mg/ml (Advanced Biomatrix Cat. ♯5007-A) are prepared. To make 50 ml of the NaOH/HEPES buffer, 2.5 ml of NaOH (Sigma Cat. ♯52770) are mixed with 10 ml HEPES and then 37.5 ml of endotoxin-free water are added. In the matrix, the final concentrations are as follows: 3% alginate (50% of the total mix), NaOH/HEPES (4.5% of the total mix), 7.5% $NaHCO_3$ (9% of the total mix), collagen type I (36.5% of the total mix, ~1 mg/ml). Before adding the collagen, the mixture is sterilised by passing through a 0.22 μm filter.

2.2. Isolation & preparation of PBMCs for bioelectrospray

Fresh human whole blood (from healthy volunteers) in heparin tubes is mixed with an equal volume of warm (37°C) Hank's Balanced Salt Solution without Ca^{2+}/Mg^{2+} (HBSS, 1x) and layered on top of 15 ml of Ficoll-Paque Plus (GE Healthcare, UK) in a falcon tube. Alternatively, the contents of leukocyte cones from healthy blood donors are mixed with 140 ml of HBSS to generate 4 falcon tubes containing 35 ml of cell suspension each. The tube is then centrifuged at 480 g, at 22°C (acceleration 5, brake off) for 30 minutes. After centrifugation, the desired layer that contains the PBMCs is extracted into a new falcon tube. The tube is filled with cold (4°C) HBSS and centrifuged at 330 g at 4°C (acceleration 5, brake on) for 8 minutes. This washing step is repeated twice and the final pellet is re-suspended in 30 ml of HBSS without Ca^{2+}/Mg^{2+} (1x) and 15 μl of the suspension are placed on a haemocytometer to count the cells. The tube is then centrifuged one last time at 330 g, at 4°C (acceleration 5, brake on) for 8 minutes, the supernatant is discarded, and the pellet is re-suspended in HBSS without Ca^{2+}/Mg^{2+}. The cell suspension is then mixed with the alginate mix in a way that the final concentration of PBMCs in the alginate matrix is $5x10^6$ cells/ml. Samples are then bioelectrosprayed (2.4.).

2.3. PBMC infection with *Mycobacterium tuberculosis*

For experiments involving *Mtb*-infection, immediately after cell counting, the appropriate number of isolated PBMCs is pipetted off and then pelleted by centrifuging at 330 g, for 8 minutes, at 4°C, in a 50 ml Falcon tube. The supernatant is then discarded, 30 ml of complete RPMI medium (Amp, Glu) with foetal calf serum are added, and the pellet is resuspended. Afterwards, PBMCs are infected with *Mtb* using a Multiplicity of Infection (MOI) of 0.1. Infected PBMCs are then transferred into a 75 cm^2 flask and left overnight in a 37°C, 5% CO_2 incubator. Empirical evidence from Dr. Tezera's and Dr. Bielecka's experiments showed that the MOI of 0.1 is low enough to allow for the cell culture to go on for 3-4 weeks without *Mtb* proliferating excessively and overtaking the microsphere; and high enough to be able to simulate early stages of infection in the human lung (e.g. early granuloma formation by aggregation of PBMCs around infected macrophages). This MOI value was specific to the proliferation rate of our *Mtb* strains. If this cell culture model is to be used to study infection by a different infectious agent, preliminary experiments will need to be performed in order to calculate the 'ideal' MOI for that agent.

The following day, the cells are prepared for encapsulation. The flask contents (30 ml) are taken out of the incubator and carefully transferred from the flask to a 50 ml Falcon tube. The flasks are then washed with 10 ml of HBSS without Ca^{2+}/Mg^{2+}, after which 5 ml of 5 mM EDTA (or Versene, Thermo Fisher Scientific) are added to the flask, followed by incubation for 8-10 minutes at 37°C in a 5% CO_2 incubator. When that time elapsed, 5 ml of complete RPMI medium are added, in order to neutralise the effect of the detachment solution. Then, the bottom surface of the flask is carefully and lightly scraped with a scraper, to re-suspend all remaining cells. Next, the 10 ml contents are returned to the same Falcon tube, already containing the medium (total 40 ml). Finally, the flask is rinsed with 10 ml of complete RPMI medium, which is then added to the Falcon tube. Afterwards, the cells are pelleted by centrifugation at 330 g for 8 minutes and the supernatant is subsequently discarded carefully. The cell pellet is then resuspended (e.g. 50 µl per $5x10^6$ cells). Five ml of alginate-collagen mix are prepared in a 7 ml Bijou and the appropriate number of cells are added to the mix accordingly (usually $25x10^6$ cells per 5 ml of alginate-collagen) and mixed well. Finally, the Bijou vials are kept at 4°C in the refrigerator or in ice, until the time of the bioelectrospraying of the cell-alginate suspension. Control uninfected cells were treated identically, but without the infection step.

Infection of PBMCs with *Mycobacterium tuberculosis* strains H37Rv and 0414B was carried out by trained personnel, namely Dr. M. Bielecka and Dr. L. Tezera, in the BSLIII laboratory.

2.4. Bioelectrospray (BES) process

The bioelectrosprayer setup comprises of a Nisco electrostatic encapsulator v1 with a washed and alcohol sterilised arm, a syringe driver, a sterile silicone tube (50 cm) (VWR Cat. ♯228-0705) and a Female Luer Thread Style Connector (The West Group Limited Cat. ♯FTLL210-J1A). The machine (*Figure 12*) is set at the rear of the Class I Microbiological Safety Cabinet (MSC) in a BSLIII laboratory.

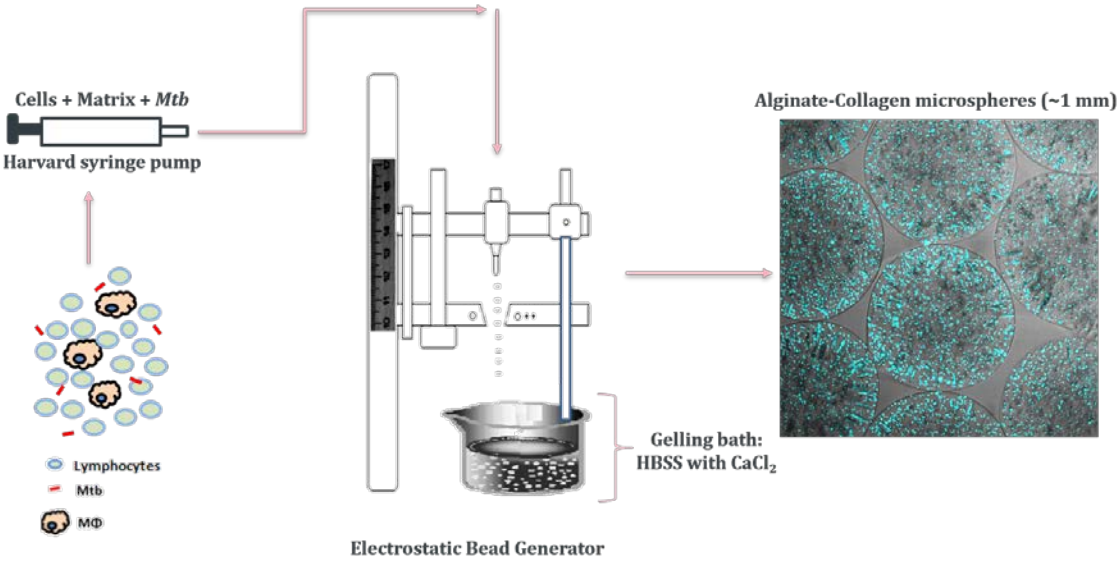

Figure 12. Bioelectrospray method and setup.

PBMCs are infected with *Mycobacterium tuberculosis* and mixed with an alginate-collagen gel. This mixture is then transferred into a syringe (which is placed on a syringe driver) and then passes through the machine (Electrostatic Bead Generator). The droplets that form at the needle tip fall into a cross-linking bath aided by an electric field and gel into microspheres of 0.9-1 mm in diameter.

First, the sterile silicone tube and the nozzle are connected to the arm of the encapsulator. A 20 ml syringe filled with HBSS without Ca^{2+}/Mg^{2+} is placed in the syringe driver and connected to the tube, so that 50 ml of HBSS pass through the tube to wash all parts of the system. The preferred flow rate is 10 ml/h. After that, a 5 ml syringe is filled with the cell-matrix mixture and placed in the syringe driver to run next. The standard voltage for the bioelectrosprayer is 6.5 kV and the stirring speed is at 70%. The droplets that form on the needle tip fall into the cross-linking bath (150 mM $CaCl_2$ in HBSS), which is placed underneath the encapsulator in a 150 ml borosilicate glass with spout (VWR Cat. ♯216-0068) with a magnetic stirrer (1 cm length).

After bioelectrospraying, the microspheres are transferred to a 50 ml falcon tube and are left to settle. After that, $CaCl_2$ is removed and - for microspheres without PBMCs - the tube is filled with HBSS with Ca^{2+}/Mg^{2+} and stored at 4°C for further use. Microspheres containing PBMCs are placed in RPMI with human serum instead and incubated at 37°C for the desired length of time.

2.5. Sample fixation

2.5.1. For label-free imaging

Microspheres with live PBMCs are fixed after bioelectrospraying in 4% PFA for 1 h at 25°C and then overnight at 4°C. PFA is then removed the next morning and replaced with HBSS with Ca^{2+}/Mg^{2+} after washing with it twice to prepare the samples for label-free imaging. Samples are then kept at 4°C until further use. Infected 3D cell cultures are prepared for imaging after overnight fixation with 4% paraformaldehyde (PFA) at 25°C and after being transferred to HBSS with Ca^{2+}/Mg^{2+} the following day.

2.5.2. For electron microscopy

Microspheres are fixed for 1 h at room temperature and then overnight at 4°C. Fixatives used for TEM imaging are either 3% glutaraldehyde and 4% formaldehyde in 0.1M PIPES [piperazine-N,N' – bis(2-ethanesulfonic acid)] buffer (pH: 7.2) or 3% glutaraldehyde in 0.1M cacodylate buffer (pH: 7.4) with an osmolarity of approximately 850 mOsm plus 2mM $CaCl_2$ (2.14.). The second fixative is also used to fix microspheres prior to SEM imaging.

2.6. Luminex assay

Supernatants were collected from microsphere experiments at day 7 and 14 after BES and sterile filtered. We measured MMP production in microspheres infected with *Mtb*. MMPs measured were human MMP-1, -2, -3, -7, -8, -9, -10, and MMP-12. Samples are first diluted (1:3) in calibrator diluent and standard is prepared according to package instructions; 450 µl of standard are placed in 'tube S1', 200 µl of diluent are placed in tubes 'S2' to 'S8' and serial dilutions are performed by transferring 100 µl from one tube to the next. In every well, 80 µl of diluent RD5-37 are added followed by 40 µl of standard or sample.

To prepare the microparticle suspension, 5.2 ml of MicroParticle Diluent (MPD) are placed in a 15 ml Falcon tube. Microparticle (blue-cap) vials are then centrifuged at 1,000 g and 4°C for 30 seconds. After spinning, microparticles are lightly vortexed and 20 µl of each kind (one for each MMP) are added to the same Falcon tube. A new plate with filters is washed by adding 100 µl of wash liquid in each well. A vacuum is applied for 2 seconds to remove all liquid. In each well on the new plate, 50 µl of microparticle suspension and 50 µl of standard or sample are added and the plate is then covered with foil and shaken at full speed for 30 seconds and then at 600 rpm for 2 hours.

To prepare the biotinylated secondary antibody, 5.2 ml of Biotin antibody diluent are transferred into a 15 ml Falcon tube covered with foil. The antibody-containing vials are spun at 1,000 g and 4°C for 30 seconds and then lightly vortexed. Twenty μl from each vial are placed in the 15 ml Falcon tube. After shaking for two hours, the plate is washed with wash buffer 3 times by adding 100 μl in each well and then vacuuming it off. Subsequently, 50 μl of microparticle/antibody/diluent mixture are added to each well, plate is covered with foil and left to shake for 1 more hour as previously described.

For the next step, a 1:100 diluted streptavidin-PE solution needs to be prepared. Vials containing streptavidin-PE are centrifuged at 1,000 g and 4°C for 30 seconds and then lightly vortexed. Then, 60 μl of streptavidin-PE are added in 6 ml of wash buffer in a Falcon tube. After one hour, the plate is washed 3 times by adding 100 μl of wash buffer and vacuuming it off for 2 seconds. Fifty μl of the diluted streptavidin-PE are added to each well and the plate is covered with foil and left to shake in the incubator for another 30 minutes. Plate is then washed 3 times using wash buffer as described above. A volume of 80 μl of wash buffer are added to each well so that the microparticles are re-suspended. The plate is then covered with foil, placed on the rocker to shake for another 2 minutes and then in the Luminex machine for analysis.

2.7. Raman spectroscopy

2.7.1. Renishaw InVia Raman microscope

For all Raman measurements, the Renishaw InVia Raman Microscope in Chemistry (B30, Highfield campus, University of Southampton) was used, which is coupled to a Leica DM 2500M microscope (*Figure 13*). The system features a 785 nm edge line laser [100 milliWatt (mW) maximum power], a Master Renishaw charged couple device (CCD) detector, a 1200 l/mm (633/780) grating and a slit opening of 65.2 μm. The spectrometer was controlled via software “Renishaw WiRE 4.1”. The 785 nm laser beam passes through a collimator, which narrows it down, and then, directed by a series of mirrors, passes through the short-working-distance x50/0.75 NA objective lens and falls onto the sample. The Stokes Raman-scattered radiation from the sample passes through the objective and is reflected by a mirror, which directs it towards an edge filter that clears it of Rayleigh and anti-Stokes Raman-scattered radiation. It then passes through a 65.2 μm slit and falls onto a 1200 l/mm grating (which separates the different scattered wavelengths) and finally the CCD detector.

The spectrometer is calibrated at the beginning of each session with a standard silicon (Si) sample (most prominent peak at ~520 cm^{-1}). Static spectra were acquired for all samples in the fingerprint region ranging from 592 cm^{-1} to 1704 cm^{-1} (central wavenumber at 1180 cm^{-1}), as well as the C-H bending region ranging from 2606 cm^{-1} to 3356 cm^{-1} (central wavenumber at 3000 cm^{-1}). All samples are placed on a Quartz cover slip and imaged using a Leica x50/0.75 Numerical Aperture (NA), short working distance objective lens (unless otherwise specified). Each spectrum shown is the average of spectra acquired from at least three different points in a single microsphere. Every acquisition was made with 50% laser power, a 30 second exposure time and 7 accumulations (unless otherwise specified).

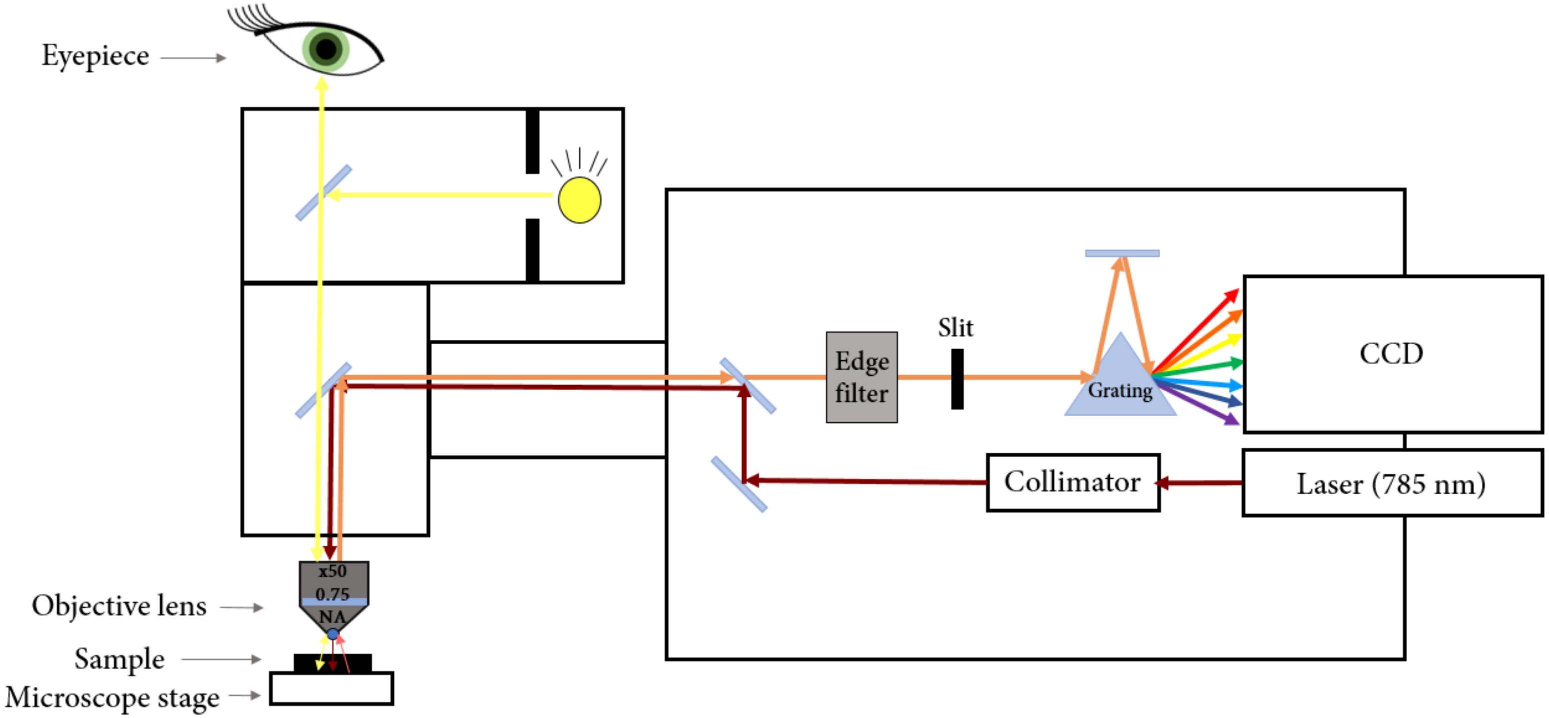

Figure 13. Renishaw InVia Raman microscope housed in Chemistry, Highfield campus, University of Southampton.

The laser (**red**) passes through a collimator and then directed by a series of mirrors passes through the objective lens and onto the sample. Stokes Raman scattered radiation (**orange**) from the sample passes through the objective and is reflected by a mirror, which sends it to an edge filter. It then passes through the slit and falls on a grating (which separates the different scattered wavelengths) and finally the detector (CCD). **Yellow** arrows indicate the white light path used to focus on the sample during standard bright-field function of the microscope.

2.7.2. Calibration of the Raman spectrometer

The Raman spectrometer needs to be calibrated before each use. In this case, a Si standard sample fixed on top of a glass slide is used for calibration. Using a x50/0.75 NA objective, I focus onto the Si sample and acquire a static Raman spectrum. Silicon is known to have its main peak at around 520-521 cm^{-1} (*Figure 14*). If the Si peak lies outside the acceptable range, then the detected Raman offset will be applied to all subsequent measurements and they will display with the adjusted value. Measuring a Si sample before each set of acquisitions helps to safely compare the wavenumber and intensity of a given peak between Raman spectra acquired on different days. The intensity and wavenumber of that peak is then used to manually normalise these spectra.

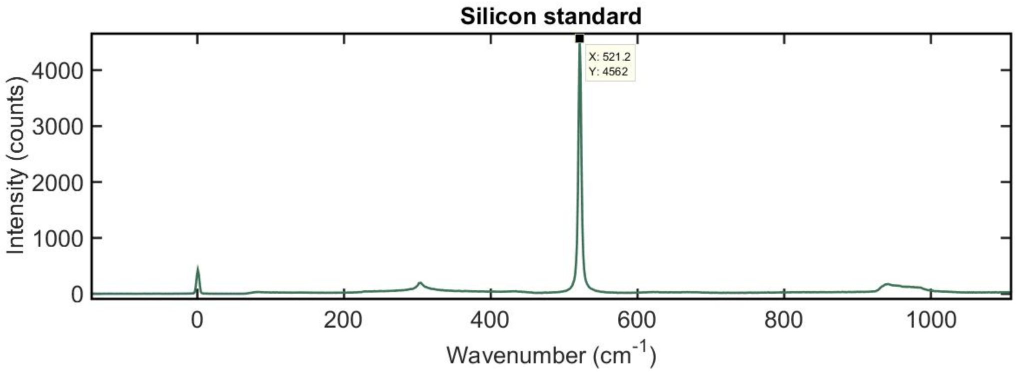

Figure 14. The Renishaw Raman spectrometer was calibrated using a silicon sample as a standard.
Central wavenumber of the spectrum at 520 cm^{-1}. Total exposure: 10 mW·sec. Silicon presents its main peak at 521.2 cm^{-1} and by calibrating with it we ensure that the spectra acquired are corrected for day-to-day differences in system performance.

2.7.3. Optimisation of Raman acquisition parameters

Optimisation of Raman spectroscopy was needed before successfully applying it to our microsphere model. A balance is always required between signal-to-noise ratio (SNR) and photodamage for all optical measurements. Therefore, the optimal acquisition parameters (such as NA of objective lens, laser power, exposure time) needed to be adjusted. Results corresponding to these optimisation experiments are described below.

Selection of an objective lens

Besides magnification, the objective lens also controls the spot size (resolution) which affects the power density of photons incident on a sample. The higher the numerical aperture, the smaller the spot size (higher power density), but also the higher the collection angle for acquiring signals. There were two x50 air objective lenses available on the Raman microscope system; one of them is a long-working-distance (LWD) objective with a NA of 0.50, and the other one is a short-working-distance (SWD) objective with a NA of 0.75. Due to the biological nature of our samples, their Raman signal is very weak. After testing both objectives combined with the laser power values available (10%, 50%, 100%) I found that much higher signal intensities can be acquired when using the SWD x50/0.75 NA air objective than the LWD x50/0.50 NA one (*Figure 15*). Therefore, I used the x50/0.75 NA objective for all subsequent measurements with the exception of some initial experiments where this objective was not available (if a different objective was used, that will be reflected in the figure legend).

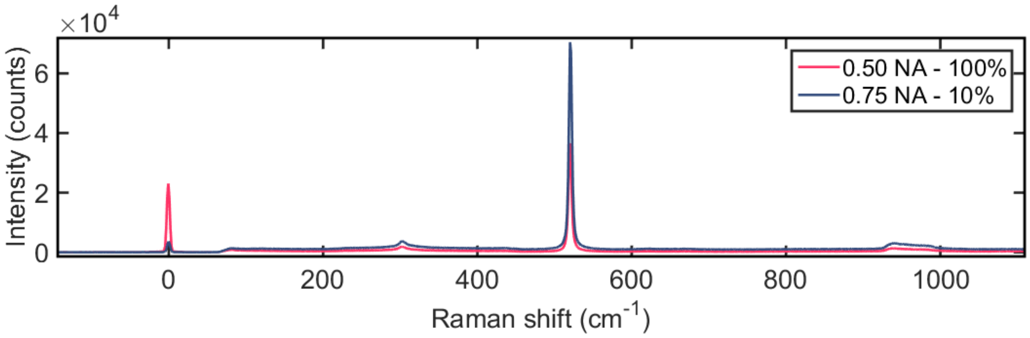

Figure 15. Comparison between objectives.

When the SWD x50/0.75 NA objective is used with just 10% laser power (**blue**) it offers similar signal intensities to when the LWD x50/0.50 objective is used with 100% laser power (**pink**). This indicates that we can acquire much higher signal intensities with the SWD x50/0.75 NA objective lens. Combined with the inherently low Raman signal of our samples, the SWD x50/0.75 NA objective lens was selected for all subsequent measurements.

Total exposure to laser (laser power, accumulations, exposure time)

A broad range of exposure time, number of accumulations and laser power combinations were tried (500-15,000 mW·sec) to determine which one provided the best SNR while at the same time did not burn the sample. The total amount of sample exposure to the incident laser light is calculated in this work as shown in *Equation 5*.

$$Total\ exposure = (Exposure\ time)\ x\ (Laser\ power)\ x\ (Number\ of\ accumulations) \qquad (5)$$

The optimal combination was found to be at around 12,000-15,000 mW·sec as shown in *Figure 16.* For the sake of image clarity not all combinations investigated are shown in this figure.

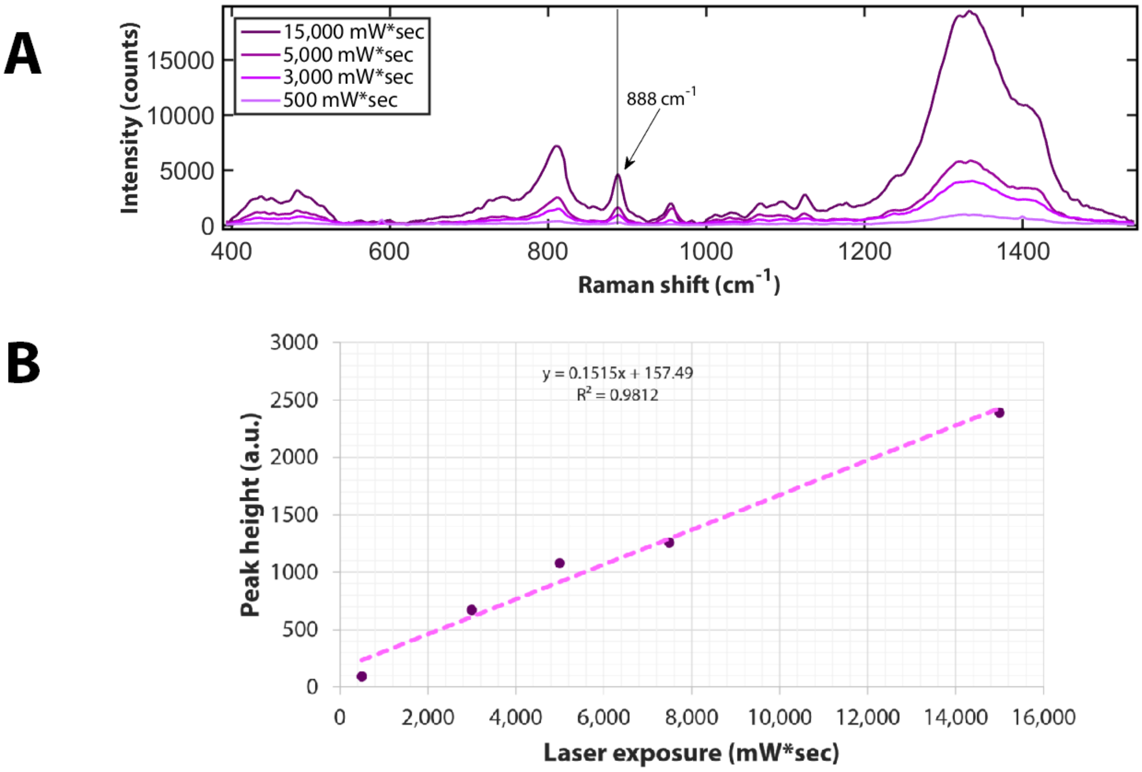

Figure 16. Effect of total exposure to laser on SNR.
(**A**) Raman spectra of alginate microspheres showing that the optimal SNR is provided by a total laser exposure of 15,000 mW·sec (plotted in IRootLab). (**B**) Scatter plot that shows the linear relationship between peak height and total sample exposure to the laser (plotted in Excel).

2.8. Processing of Raman spectra

For all Raman spectra cosmic rays are removed manually using WiRE 4.1 software. After cosmic ray removal, the spectra are normalised for laser power and exposure time, as well as for the number of accumulations by dividing all intensities with these three values in Microsoft Excel. Spectra are also normalised with the Si peak; their intensities are divided by its intensity. Subsequently, all spectra are pre-processed in '*IRootLab*', which is a Matlab toolbox.[153] Pre-processing includes rubberband-like baseline correction, noise smoothing using "wavelet de-noising" and normalisation using the maximum peak. All intensity values in each spectrum were normalised by the height of the peak with the most intense Raman signal in the spectrum as an extra layer of consistency between different measurements. Every spectrum is acquired at least 3 times and each time with at least 5 accumulations on each occasion.

2.8.1. Optimisation of background subtraction method

Different background subtraction methods are available in IRootLab. All methods available were explored, but the ones more relevant to our spectra were the polynomial and the rubberband-like baseline correction.

Different orders of polynomial were investigated as shown in *Figure 17*, however, they all created artefacts in the spectrum. This method tries to fit a polynomial curve whose order is specified by the user. Due to computing power limitations, the maximum polynomial order that could be applied to the spectra was the 9th. A polynomial curve of a much higher order might have been able to fit these data, but even the 9th order one created large artefacts in the Raman spectra.

The most effective background subtraction for our spectra was found to be the rubberband-like baseline correction. This algorithm first identifies the areas of minimum intensity (local minima) between two peaks in the spectrum. It then connects the local minima with a line, as if it was attaching a rubber-band to them and then everything below the line is removed as background.

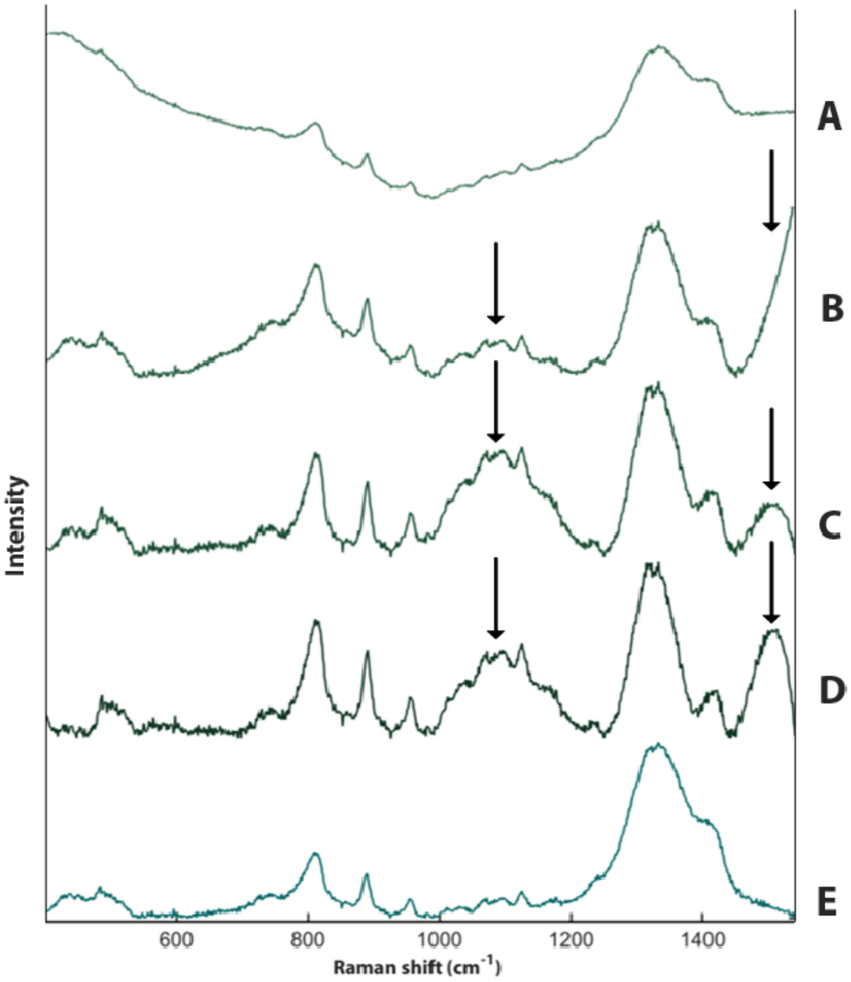

Figure 17. Different background subtraction methods.

(**A**) Raw spectrum of alginate microspheres. (**B**) 5th Order polynomial baseline correction applied. (**C**) 7th Order polynomial baseline correction applied. (**D**) 9th Order polynomial baseline correction applied. (**E**) Rubberband-like baseline correction applied. Polynomial baseline correction created artefacts (indicated by **black arrows**) in the spectra (e.g. area roughly between 1000 cm^{-1} and 1200 cm^{-1} and pseudo-peak at around 1500 cm^{-1}). The method that removed most of the background without creating artefacts is the rubberband-like baseline correction.

2.8.2. Optimisation of noise smoothing function

De-noising of a spectrum can be performed in a number of ways in Matlab. Wavelet de-noising was selected as the method of choice as it is known for removing the noise while preserving the sharp features in it (i.e. peaks) without smoothing these out. Fourier-based de-noising uses a low-pass filter to remove noise but in the process would smooth out the peaks in the spectrum. Wavelet de-noising represents the real signal in a few wavelet coefficients. Noise tends to be represented by small wavelet coefficients, which get eliminated. In our case, large wavelet coefficients are Raman peaks originating from the sample or its environment.

After background subtraction, noise smoothing of the Raman spectra in this thesis is performed using the wavelet de-noising function of IRootLab (Matlab). Different levels of decomposition were explored, as shown in *Figure 18*. The one that removed noise completely was the 6-decomposition-level wavelet de-noising. In certain instances, though, it also removed some real features of the spectrum (e.g. very small peaks), so a lower number of decomposition levels were used (5), and wherever this is the case it is clearly stated in the figure caption.

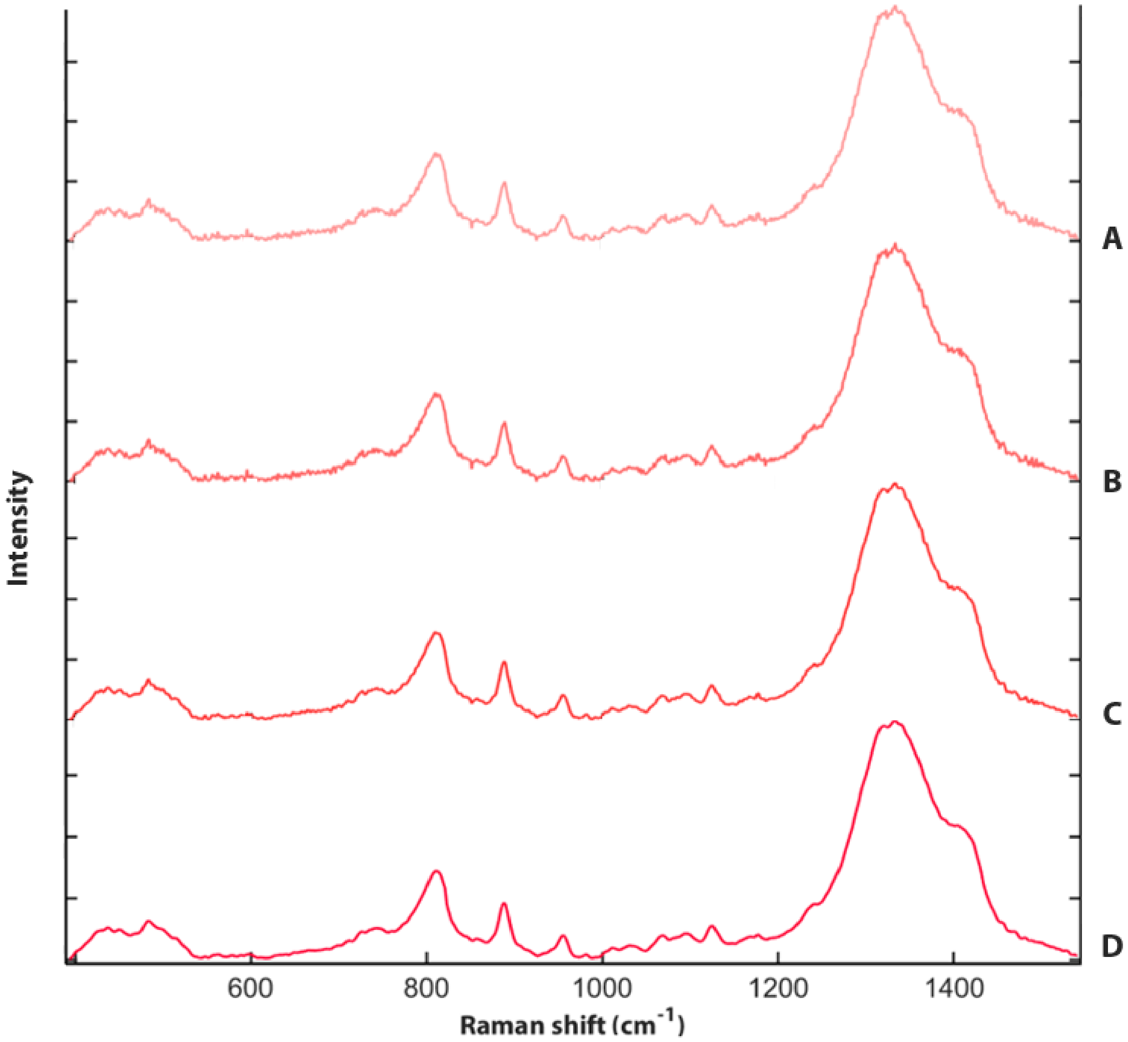

Figure 18. Wavelet de-noising of different decomposition levels.

(**A**) Spectrum with no de-noising. (**B**) Wavelet de-noising of 4, (**C**) 5, (**D**) or 6 decomposition levels applied. The best noise removal is provided by wavelet de-noising of 6 decomposition levels but in some cases very small peaks tend to disappear (not shown). In those cases, 5 decomposition levels provided a similar level of noise removal without eliminating these sensitive features of the spectra.

2.9. Coherent Anti-Stokes Raman Scattering (CARS) microscopy

2.9.1. The CARS setup

The CARS system used for these measurements has been custom-built by researchers in the Bionanophotonics group in the Institute of Life Sciences (B85, Highfield campus, University of Southampton) (*Figure 19*). It comprises of two lasers; the Stokes laser beam, which is fixed at 1031 nm and the pump laser beam, which is tuneable, and its wavelength can go from 650 nm up to the order of μm. The system is coupled to an inverted Nikon Eclipse Ti-U microscope and two detectors (PhotoMultiplier Tubes, PMTs); one for CARS and one for SHG. The two laser beams are combined by a beam combiner (short pass dichroic - cut off: 850 nm) and then continue to the scanner that uses them to scan the sample. From the scanner and through the upper turret of the microscope, where an excitation filter [short pass dichroic – cut off: 750 nm (Chroma, 750spxrxt)] is installed, it passes through the microscope objective lens (x20/0.75 NA, air objective) to the sample. Scattered radiation from the sample returns and passes through the excitation filter to the microscope prism. From there it is directed to a long pass interference dichroic beam splitter (Semrock, DI02-R442) which separates the different signals and directs the SHG signal to a PMT detector (Hamamatsu, H10722-20) and the CARS signal to a different PMT (Hamamatsu, H10722-20). A band pass filter is used in the SHG channel and a filter stack comprising a short pass interference filter (Semrock, BrightLine Fluorescence Filter 775/SP) and a band pass interference filter (Semrock, BrightLine 643/20) is used in the CARS channel. A lens with a focal length of 30 mm [Achromatic Doublet, ARC: 650-1050 nm (Thorlabs, AC254-030-B-ML)] is used to focus the signal. The pump beam’s settings are controlled via APE O.P.O. software installed on a laptop. Acquisition parameters are controlled via Matlab2012b (‘scanimage’).

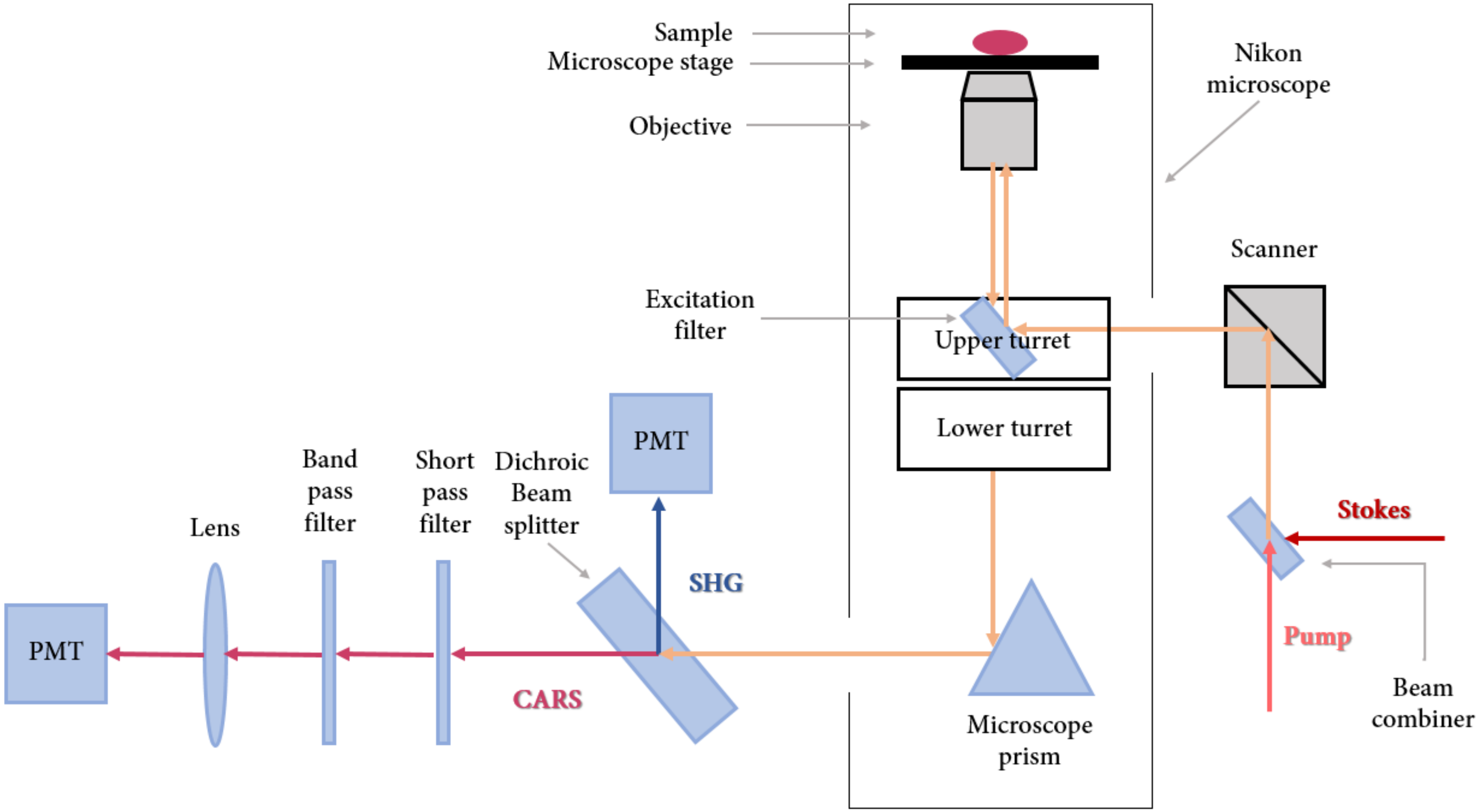

Figure 19. Custom-built CARS setup in IfLS, Highfield campus, University of Southampton.

The Stokes and pump laser beams are combined by a beam combiner and then reach the scanner that uses them to scan the sample. The combined lasers fall on an excitation filter and are redirected to pass through the objective lens, onto the sample. Scattered photons from the sample go through the objective and back through the excitation filter, and reach the microscope prism which sends them to a dichroic beam splitter. The SHG signal is diverted to a PMT for detection, whereas the CARS signal continues through a series of short and band pass filters to a different PMT for detection. For clarity, the SHG channel detection system is shown without the filter and lens setup.

The pump laser wavelength that corresponds to the CARS wavenumber of interest is calculated each time using *Equations 6, 7, 8*:

$$\lambda_{CARS} = \frac{1}{\frac{2}{\lambda_{pump}} - \frac{1}{\lambda_{Stokes}}} \tag{6}$$

$$\omega_{CARS} = \frac{1}{\lambda_{pump}} - \frac{1}{\lambda_{Stokes}} \tag{7}$$

$$\lambda_{CARS} < \lambda_{pump} < \lambda_{Stokes} \tag{8}$$

The laser power for each acquisition is measured (for the pump beam) after the clean-up filter and (for the Stokes beam) after the polarizing beam splitter (PBS). Laser power is also measured after the objective lens to monitor system performance and more specifically to determine the exact percentage of the output laser power that reaches the sample.

Glass microscope slides have to be placed face-down on the microscope for CARS/SHG imaging, so the sample needs to be sealed with a glass cover slip to prevent spillage. The microspheres have a diameter of approximately 1 mm which prevents the cover slip from being placed directly on top of them and seal properly. Therefore, two small ‘wells’ were manually created on top of each glass slide using parafilm, so that the cover slip placed on top would completely seal the well. Cover slips are fixed on the wells with nail polish.

2.9.2. Optimisation of CARS acquisition parameters

Due to the unique nature of our sample, various CARS acquisition parameters first needed to be optimised for the system to start detecting the weak signal of our microspheres.

Target frequency for combined CARS/SHG imaging

CARS imaging at the two standard wavenumbers for lipids (2850 cm^{-1}) and proteins (2960 cm^{-1}) showed that it is possible to clearly visualise PBMCs in the microspheres (*Figure 20*). Overlaying this image with an SHG image of the same field of view gives information about the collagen fibrils distribution in relation to the cells. Other frequencies were imaged as well (data not shown), such as 3030 cm^{-1} (a common frequency in sugars) and 2930 cm^{-1} (common in proteins) but the frequency which offered the best contrast for the cells and collagen was 2845-2850 cm^{-1}.

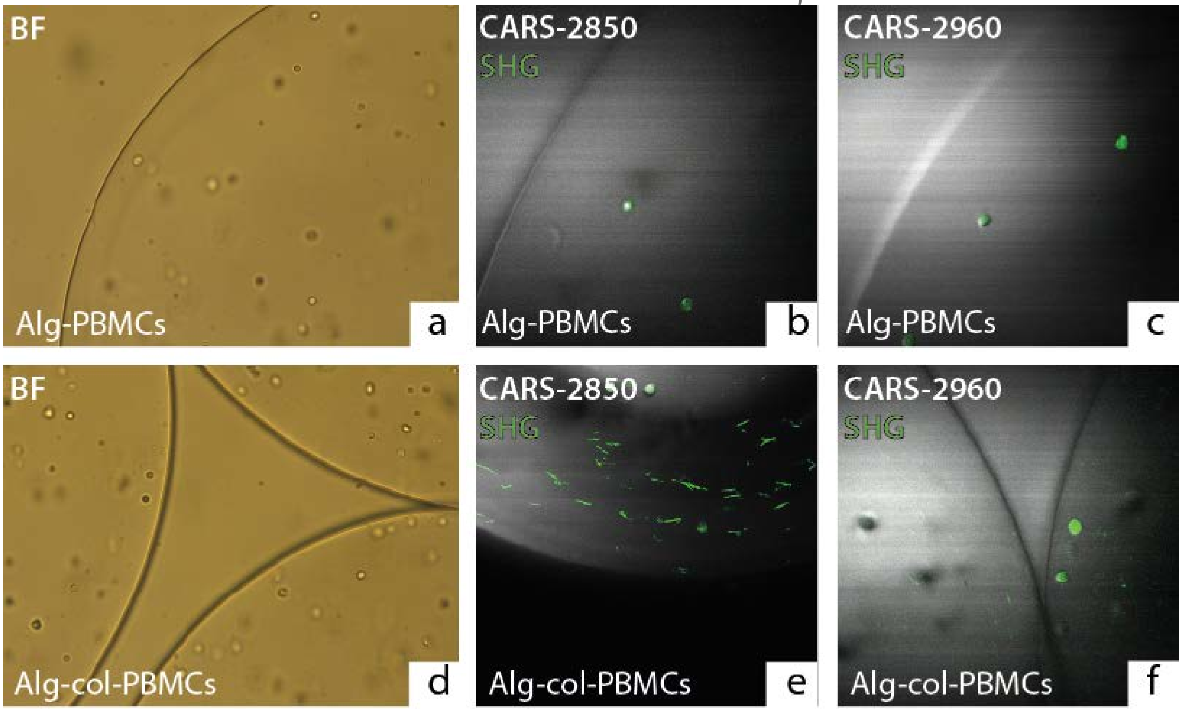

Figure 20. CARS and SHG of PBMCs in alginate and alginate-collagen microspheres imaged at 2850 cm^{-1} (for lipid) and 2960 cm^{-1} (for protein) after 4 days of incubation at 37°C. SHG channel (cells and collagen fibrils) is shown in **green** (LUT applied in Fiji) and CARS channel in grey. (**a**) Bright-field (BF) image, (**b**) overlay of CARS (at 2850 cm^{-1}) and SHG images, and (**c**) overlay of CARS (at 2960 cm^{-1}) and SHG images of alginate-PBMC microspheres. (**d**) BF, (**e**) overlay of CARS (at 2850 cm^{-1}) and SHG, (**f**) overlay of CARS (at 2960 cm^{-1}) and SHG images of alginate-collagen-PBMC microspheres. Collagen and cells are best imaged at 2850 cm^{-1} with CARS. Scale bar = 50 μm. The camera used for BF imaging is different to the detectors for CARS and SHG and they view different parts of the sample. The CARS and SHG detectors are viewing a smaller FoV that corresponds roughly to the upper right hand area of the BF camera's FoV, only rotated by approximately 90º clockwise.

Step size (z-stacks)

Different slice thicknesses (i.e. distance between two consecutive z-stack slices) were investigated, ranging from 1-5 μm. A distance of 5 μm is adequate to detect all the cells with CARS, but to image all collagen fibrils a distance of 1 μm is acquired.

Additional zoom

The CARS/SHG and SHG/TPEF systems used offer optical zoom up to x7 in addition to the objective's magnification. With no additional magnification the laser illumination does not adequately cover the entire field of view. To achieve an almost uniform illumination in the entire field of view, additional magnification is required. I tried all the different available magnifications to find the one that covered the biggest area of the microsphere, while at the same time provided enough detail in cell imaging (*Figure 21*). The optimal magnification by these criteria was found to be x3.

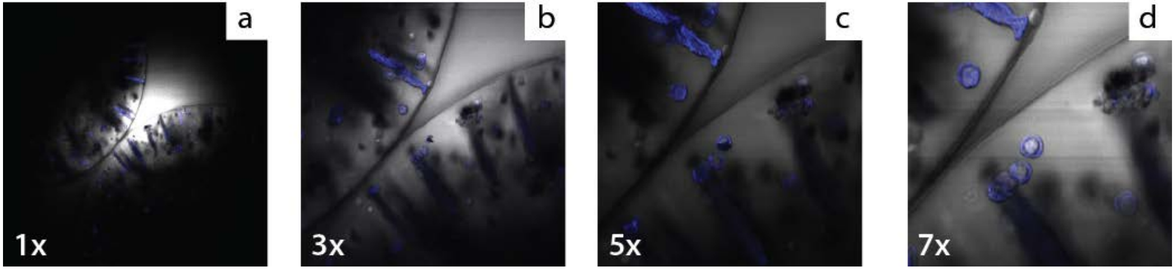

Figure 21. Additional zoom of 3 times offers the largest field of view, in which the cells can be clearly visualised.

Overlay of CARS (**grayscale**) and SHG (**blue**) image of alginate-collagen microspheres with PBMCs. (**a**) No additional magnification (1x) as well as 2x (not shown) magnification results in intense illumination of the centre of the field of view and very poor illumination of its periphery. (**b**) An additional magnification of 3 times offers clear imaging of the cells, while at the same time allows for imaging to cover a large area of the microsphere. (**c**, **d**) Increasing the magnification further (up to 7x) results in increasingly detailed imaging of the cells, but also increasingly limited FoV. Therefore, a 3x additional magnification is used in subsequent acquisitions.

2.10. Second Harmonic Generation (SHG) microscopy and Two-Photon-Excitation Fluorescence (TPEF)

A multiphoton imaging setup for SHG and TPEF has also been custom-built by researchers in the Bionanophotonics group (Institute for Life Sciences - IfLS, UoS) and coupled to an upright microscope (*Figure 22*). It features a tuneable 100-fsec-pulse laser. For Two-Photon-Excitation Fluorescence detection, a range of different filters is available; 410 nm, 430 nm, 520 nm, 650 nm and 785 nm. Apart from that, the system also comprises of a Galvo scanner (Cambridge technology 6220H), a PMT for detection of the SHG signal (Hamamatsu H10722-20), another PMT for detection of the TPEF signal (Hamamatsu H10722-01), and a microscope stage controller. Laser settings are controlled via the software “Spectra system” and the acquisition parameters for the SHG and TPEF are controlled via Matlab2012b (“scanimage”). For all images presented here the laser wavelength was set at 800 nm and the microscope objective used for all measurements is L20x/0.50 NA Water. The laser power was measured after the objective after each acquisition.

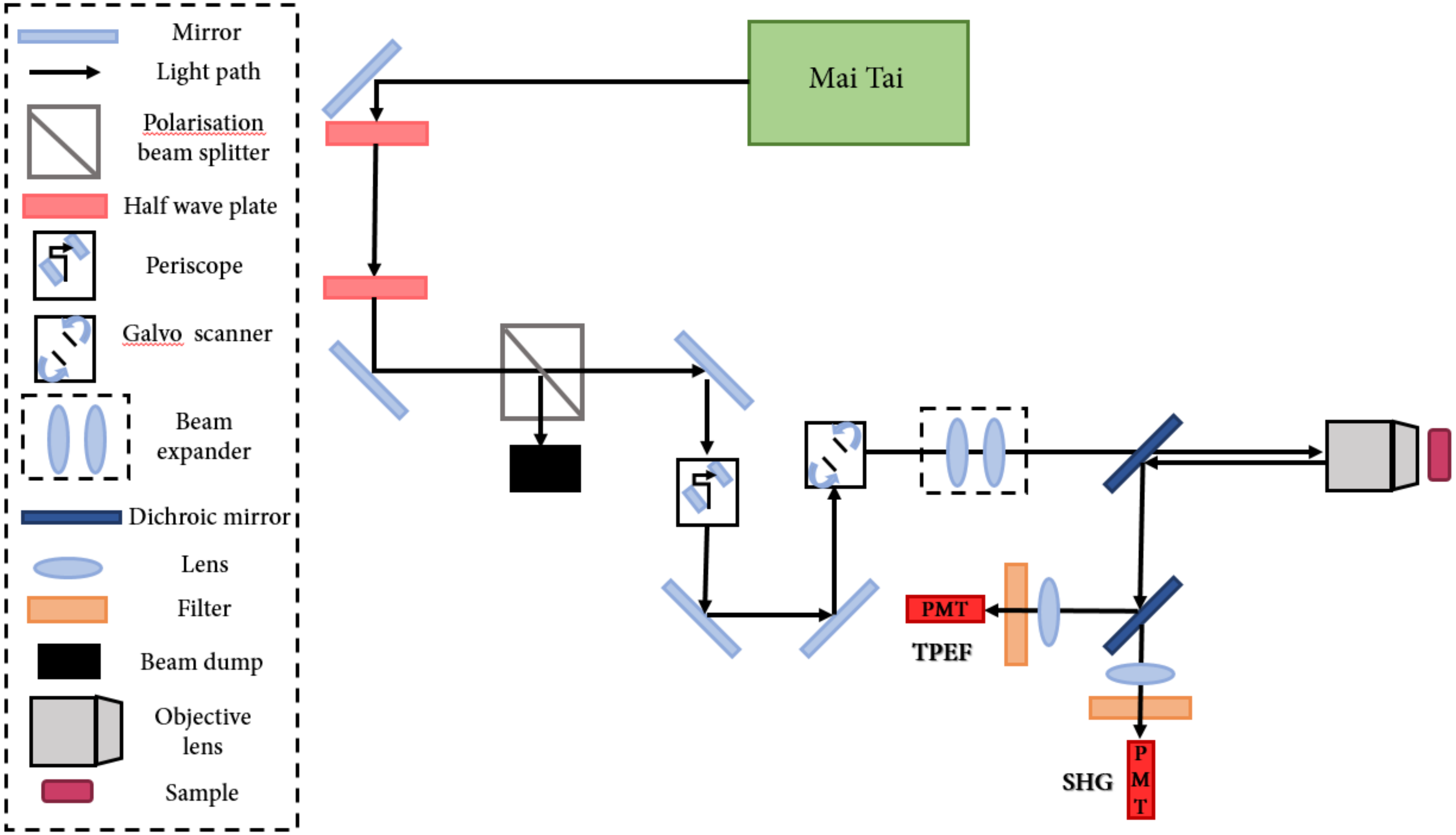

Figure 22. Custom-built SHG setup housed in IfLS, Highfield campus, University of Southampton.

The MaiTai generates the laser which is redirected by a series of mirrors to the scanner, then a periscope and then the beam expander. From there and through a dichroic mirror the beam passes through the microscope objective lens and falls onto the sample. Light emitted from the sample comes back through the objective and falls onto a second dichroic mirror, which then diverts the TPEF signal to a PMT detector and lets the SHG signal pass through to a different PMT.

2.11. Image processing of CARS, SHG acquisitions in Fiji

Initially, the brightness and contrast of the images are manually adjusted. Wherever a pseudocolour is applied, this is done by applying a Look-Up Table (LUT) in Fiji.

Collagen fibrils in SHG images are much brighter than the background, so the only image processing needed is noise removal using the ‘Despeckle’ function of Fiji. LUTs applied to the SHG channel in different figures are ‘Blue’, ‘Fire’, ‘Green’ and ‘Cyan’, always specified in the figure legend. Z-stacks of SHG acquisitions are presented in the form of a z-projection of the maximum intensity in Fiji. 3D projections of SHG z-stacks rotating by 360° around the Y-axis at 10 frames per second (fps) are presented as AVI videos and are included in *Chapter 4.* .

A typical characteristic of most CARS images acquired is the inadequate contrast between cells and their background (microsphere matrix) which renders automatic object-counting tools of Fiji unable to successfully detect and count PBMCs and their aggregates in microspheres. Whilst trying to enable automatic cell counting and/or improve image clarity, I applied a range of different filters available in the software. The ‘Median’ filter replaces each pixel with the median intensity of its neighbouring pixels and is used to reduce noise in the image. The ‘Mean’ filter does the same but using the mean intensity of the neighbouring pixels instead of the median. The ‘Minimum’ and ‘Maximum’ filters replace each pixel with the lowest or highest intensity value of its neighbouring pixels, respectively. ‘Unsharp mask’ is used to sharpen the image and works by subtracting a Gaussian blur of the image with a user-specified standard deviation and then rescaling it. The ‘Variance’ filter replaces each pixel with the variance of its pixel neighbourhood and therefore enhances edges (e.g. edges of PBMCs).

The effect of some of these filters is depicted in *Figure 23* below. The ‘Unsharp Mask’ filter in Fiji (*Figure 23d*) sharpens the image slightly in a way that cellular outlines and morphology are more apparent but makes no difference in the performance of automatic Fiji object-counting tools. The ‘Variance’ filter makes certain cells brighter than the background enabling the ‘3D object-counting’ tool of Fiji in some individual slices of the CARS z-stacks but not in an adequate number of slices to allow for extraction of any meaningful measurements in 3D. Image quality deteriorates with each of the other available filters in Fiji.

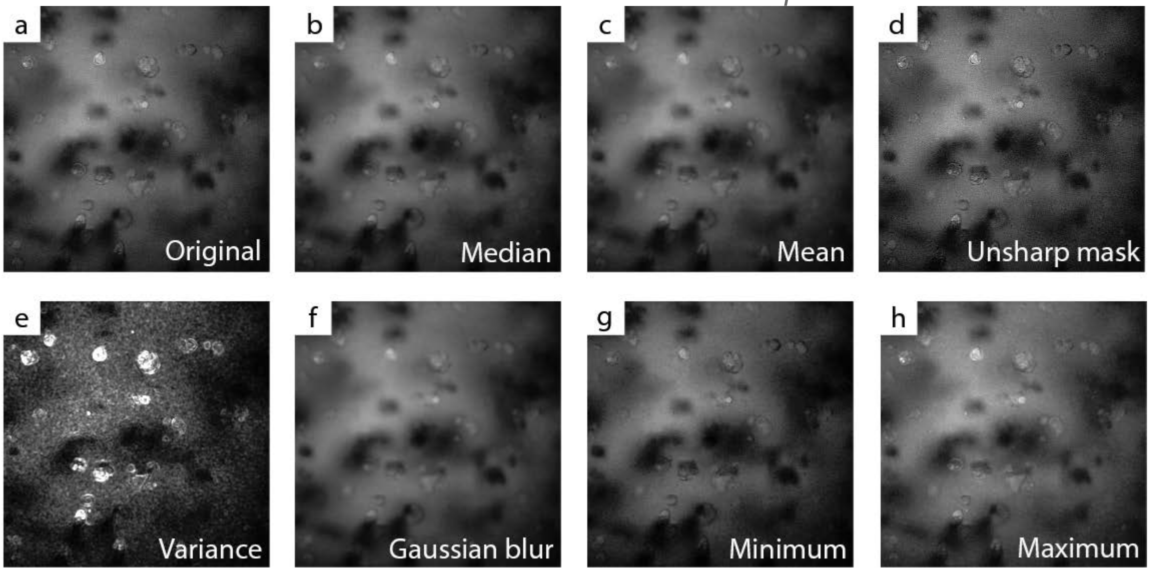

Figure 23. Application of different ImageJ/Fiji image filters.

(**a**) Original CARS image of microspheres with PBMCs infected with *Mycobacterium tuberculosis* with no filter applied. The cells cannot be automatically thresholded against the background based on their intensity. (**b**) 'Median' with a 2-pixel radius. (**c**) 'Mean' with a 2-pixel radius. (**d**) 'Unsharp mask' with a 1-pixel radius and a mask weight of 0.6 enhances image contrast. (**e**) 'Variance' with a 2-pixel radius makes the cells brighter than the background and enables 3D object-counting tool of Fiji in some images. (**f**) 'Gaussian blur' with a 2-pixel radius. (**g**) 'Minimum' with a 1-pixel radius. (**h**) 'Maximum' with a 1-pixel radius. To summarise, the 'Unsharp mask' filter (**d**) slightly sharpens the image and the 'Variance' filter (**e**) enhances contrast between cells and background in a way that enables thresholding and therefore automatic object counting in some of the images.

2.12. Propidium Iodide (PI) fluorescent staining

Propidium iodide (PI) intercalates between DNA or RNA bases and stains dead cells, as live cell membranes are impermeable to it. Its maximum fluorescence is at 617 nm and has an excitation peak at 535 nm. Fluorescent staining of the microspheres with PI is performed with a 1:50 ratio. In a Bijou vial covered on the exterior with aluminium foil, 1.5 ml of microspheres are placed in HBSS with Ca^{2+} and Mg^{2+} without phenol red and 30 µl of PI fluorescent stain are added. The vial is lightly shaken and the spheres can either be imaged right away or be kept in the fridge. The light of the MSC is kept off throughout this process due to the fluorescent properties of the stain.

2.13. Confocal microscopy

Alginate-collagen microspheres with *Mtb*-infected PBMCs are created using a combination of 1/3 DQ-collagen and 2/3 human type I collagen dissolved in HCl. DQ-collagen fluoresces green when cleaved by collagenases. Microspheres are cultured for 14 days before harvesting and imaging with confocal microscopy. Propidium iodide which fluoresces red is used as a nucleic acid stain to stain dead cells in the microspheres.

2.14. Transmission Electron Microscopy (TEM)

2.14.1. Sample processing

Microspheres are harvested from the incubators at pre-defined time points and are fixed for 1 h at room temperature and then overnight at 4°C. Fixatives used are either 3% glutaraldehyde and 4% formaldehyde in 0.1M PIPES [piperazine-N,N’ – bis(2-ethanesulfonic acid)] buffer (pH: 7.2) (**fixative A**) or 3% glutaraldehyde in 0.1M cacodylate buffer (pH: 7.4) with an osmolarity of approximately 850 mOsm plus 2mM $CaCl_2$ (**fixative B**). Fixed samples are then washed with the respective buffer depending on the fixative used (**A** or **B**), and post-fixed with 2% osmium tetroxide in **buffer A** (0.1M PIPES buffer at pH 7.2) or **B** (0.1M cacodylate plus 2mM $CaCl_2$ plus 2.3M sucrose). Osmium as a heavy metal also acts as a stain for cell membranes. After a distilled water wash, samples are stained with 2% uranyl acetate$_{(aq)}$, which predominantly stains nucleic acids. Another distilled water wash follows, before samples are dehydrated through a series of ethanol submersion steps of progressively higher concentrations. Ethanol solution concentrations used are: 30%, 50%, 70%, 95%, 100% (absolute ethanol). The absolute ethanol step is performed twice and then samples are immersed in acetonitrile, which facilitates the passage from ethanol to resin since the last two ingredients do not mix satisfactorily. Samples remain in a 50:50 acetonitrile/resin mixture overnight, followed by a stay in fresh resin for 6 h and are subsequently transferred into embedding capsules containing fresh resin. Spurr resin is used for samples fixed using **fixative A** and TAAB resin for those fixed in **fixative B**. The embedding process is finalised by placing the samples at a temperature of 60°C for 16 h in order for the resin to cross-link, polymerise and harden enough so it can be thinly sectioned.

2.14.2. Ultramicrotomy

Before cutting ultra-thin (0.1-0.15 μm) sections off our sample, thicker (0.5 μm) sections are cut and stained with toluidine blue to ensure that the sample is cut at the right depth. Each resin block is placed in the chuck of the microtome and secured. Using a razor, the block-face is scraped until the specimen is revealed and cut into the shape if a trapezium. A freshly cut, glass knife is then placed on the knife holder of the microtome and the sample is shaved until the entire block-face is perfectly polished and a full section is coming off with every cut. Using a new glass knife with a plastic ‘boat’ attached to it, 0.5-μm-thick sections are cut and placed in a drop of distilled water on a glass slide. A cotton dab dipped in chloroform is hovered above the freshly cut sections on water, in order to stretch them completely.

The next step is to stain sections with toluidine blue. The glass slide with the sections is placed on a hot plate set at 100°C for 20 minutes until it's completely dry. While still on the hot plate, it is flooded with filtered 1% toluidine blue in 1% borax solution to stain the different sample components (e.g. cell nuclei are stained blue) and make them visible under a bright-field microscope. After 1-2 minutes on the hot plate, a green ring starts to form around the stain. The glass slide is carefully removed from the hot plate, washed under running tap water until all excess stain is removed from the sections. Stain that has been bound cannot be washed off. The glass slide is then dried gently using filter paper and returned to the hot plate for 10 minutes to dry off completely before mounting. After that, the slide is removed from the hot plate and left to cool off. When it is cool enough, a small volume of mountant (DPX) is placed between the glass slide and a cover slip to seal the sections and protect them from dust and mechanical damage.

After ensuring the sample is cut at the desired depth, a new glass knife with a plastic 'boat' is placed on the microtome and ultra-thin (0.12 μm thick) sections are taken. These are then counterstained with lead citrate and imaged with a TEM microscope.

2.14.3. TEM imaging

TEM images are obtained using a FEI Tecnai T12 Transmission Electron Microscope (*Figure 24*) equipped with a Morada G2 digital camera up to 11 Megapixels. This microscope offers voltage up to 120 kV (80 kV were used) and a magnification of up to 500,000x. The camera is controlled via software package Radius (Olympus). Image brightness and contrast are adjusted in the same software before saving each image file as an 8-bit and a 16-bit image compressed into one TIFF file. After a certain software update, images were saved as a single RGB Color TIFF file.

Figure 24. FEI Tecnai T12 Transmission Electron Microscope in the Biomedical Imaging Unit (BIU) facility at University Hospital Southampton (UHS). (*Source: Biomedical Imaging Unit website, Equipment and Facilities - TEM*)

2.14.4. Calculation of nucleus-to-cytoplasm ratio and lipid body (LB) size

Every cell present on each TEM section is photographed and its nucleus-to-cytoplasm ratio is calculated. In Amira 6.4.0, the area of cytoplasm, nucleus, and lipid bodies (where applicable) are highlighted with different colours (*Figure 25*) and their area is measured in μm^2.

Each TIFF image file is first opened in Fiji to determine its pixel size. Using the line selection tool, the scale bar (burned on the TEM image by default) is selected and by clicking the option 'Analyze' on the main toolbar and then 'Set Scale' on the menu that opens, a new window pops up. The 'Distance in pixels' shows the length of the selected scale bar in pixels. The 'Known distance' field is populated with the number in micrometres as indicated by the scale bar. 'Pixel aspect ratio' is kept at '1.0' and the 'Unit of length' is changed to 'micron'. I click 'OK' to close that window and then on the main toolbar, 'Image' is selected followed by 'Properties'. A new window opens that shows the pixel size in micrometres.

The image is saved, closed, and then opened again in an Amira project file ('Open Data' – select image – click 'Open' – input pixel/voxel size – click 'OK'). In the 'Segmentation' tab, three 'Materials' are added corresponding to the cytoplasm (red), nucleus (blue) and lipid bodies (yellow). These three areas are manually annotated in the image using the 'Pen' tool and added to their respective 'Material'. In the 'Project' tab, by right-clicking on the '.labels' object we select: Measure & Analyze → Individual measures → Label analysis → Create. The 'XY Interpretation' box is ticked and 'basic 2D' is selected in the 'Measures' section of the settings to measure area. By clicking 'Apply' a table appears that indicates the total area of each of our 'materials' in the unit specified (in our case, μm^2). The first line of the table represents the area of the material ‘Inside’ (which is disregarded), and the rest represent our materials in the order in which they were added to the ‘.labels’ object.

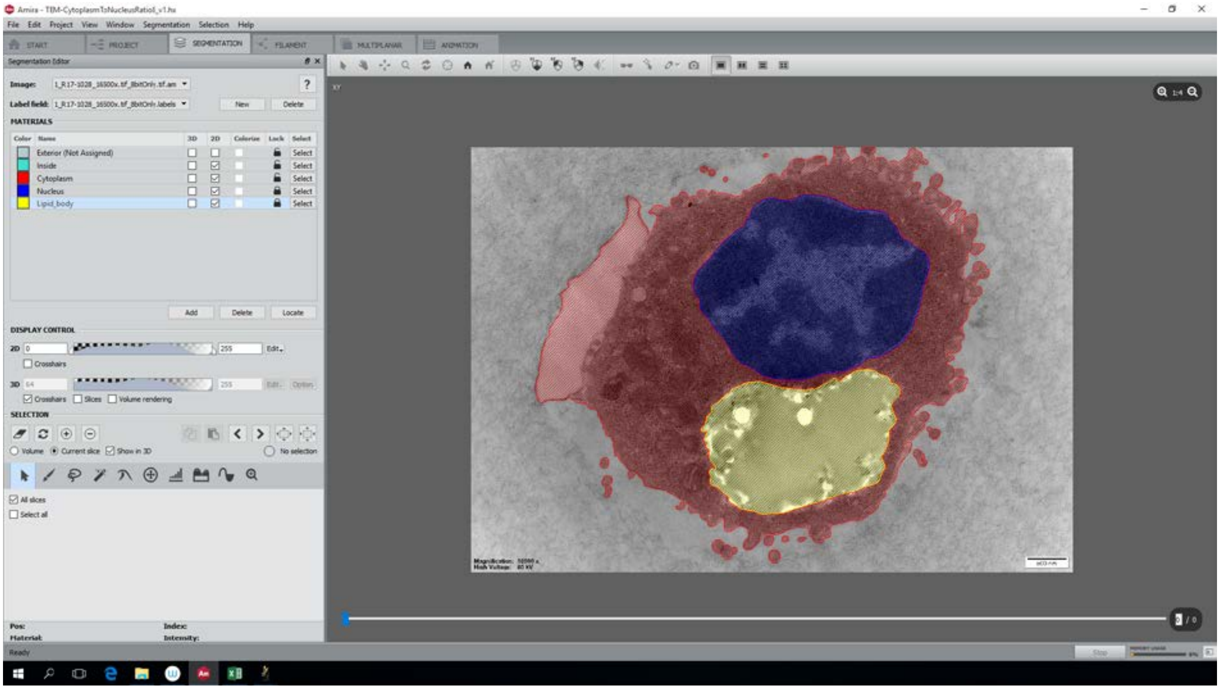

Image: 1_R17-1028_16500x.tif_8bitOnly.tif.am

Label field: 1_R17-1028_16500x.tif_8bitOnly.labels

MATERIALS

Color	Name	3D	2D	Colorize	Lock	Select
	Exterior (Not Assigned)	☐	☐			Select
	Inside	☐	☑			Select
🟥	Cytoplasm	☐	☑			Select
🟦	Nucleus	☐	☑			Select
🟨	Lipid_body	☐	☑			Select

Figure 25. TEM picture of a cell in software ‘Amira’.

The cytoplasm area is manually segmented in **red** and the nucleus in **blue**. Lipid bodies are segmented in **yellow**.

2.15. Scanning Electron Microscopy (SEM)

2.15.1. Sample processing

Microspheres are fixed for 1 h at room temperature and then overnight at 4°C with **fixative B** (*TEM sample processing*). Fixed samples are then rinsed with **buffer B** (*TEM sample processing*) and post-fixed with 2% osmium tetroxide in **buffer B**. After a distilled water wash, samples are dehydrated through a series of ethanol submersion steps of progressively higher ethanol concentrations [30%, 50%, 70%, 95%, and 100% (absolute ethanol)]. The absolute ethanol step is performed twice.

Once the final ethanol step is complete, microspheres are placed in a metal holder with a grid. The lid is screwed on top of the metal holder and the entire holder is placed in a sealed glass vial filled with absolute ethanol until SEM imaging. Samples are subjected to critical-point-drying using a Balzers CPD 030 critical point drier. Dried microspheres are placed on a stub covered with two-sided tape and coated with a mixture of the non-oxidising metals gold (Au) and palladium (Pd) using a Polaron E5100 sputter coater.

2.15.2. SEM imaging

SEM images are acquired using a FEI Quanta 200 Scanning Electron Microscope (*Figure 26*). This system offers power of up to 30 kV and up to 100,000x magnification. Power used for acquisitions is 10 kV. Images acquired are then pseudocoloured in GIMP (free image-manipulation software) to highlight different features (alginate-pink, collagen-yellow, *Mtb* bacilli-green).

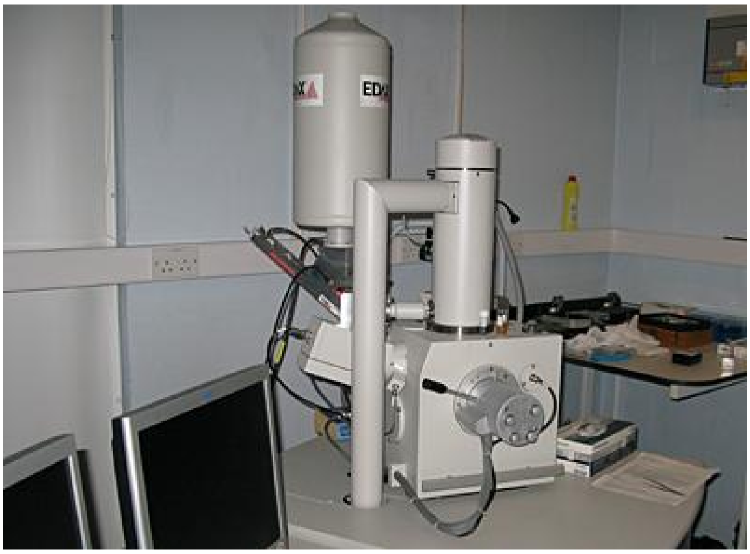

Figure 26. FEI Quanta 200 Scanning Electron Microscope (SEM) located in the Biomedical Imaging Unit (BIU) facility at University Hospital Southampton (UHS).
(*Source: Biomedical Imaging Unit website, Equipment and facilities – SEM*)

2.16. Histology of human lung biopsy

A human lung biopsy from a TB patient at surgery had previously been formalin-fixed, embedded in paraffin, and stored for approximately 4 years. The block was identified as ideal as it was the only *Mtb*-culture-positive lung biopsy from a patient not yet on treatment for TB. The block was first imaged by micro-CT (*Microfocus X ray Computed Tomography (µCT) imaging*) and then sectioned and stained for various molecules. Initially, 101 serial sections were taken off the biopsy onto slides, of which the 1st and every tenth after that were stained with H&E (*Haematoxylin & Eosin (H&E) staining*). The second section and every tenth after that were stained with Elastin van Gieson (EVG) to visualise elastin and collagen fibres of the extracellular matrix. (*Staining of elastin with Elastic Van Gieson (EVG)*). Finally, the third section and every tenth after that were stained with Ziehl-Neelsen (or acid-fast) stain for *Mtb* bacilli (*Staining of Mtb bacilli with Ziehl Neelsen (ZN or acid fast)*).

2.16.1. Haematoxylin & Eosin (H&E) staining

The first section and every tenth after that were stained with H&E, which stains nuclei as blue/black, cytoplasm and extracellular matrix as pink/red. The tissue first needs to be deparaffinised before staining begins. Unstained lung tissue sections are placed back-to-back in each slot on a rack and then submerged into clearing agent (XTF Clearing agent, Cell Path, SEA-2000-00A) for 10 minutes. The rack is then submerged in one more clearing solution bath for 10 minutes and subsequently washed with absolute alcohol (Industrial methylated spirit, Fisher Scientific, #11492874) twice, for 5 minutes each time. Slides are then placed in 70% alcohol (prepared using: Industrial methylated spirit, Fisher Scientific, #11492874) and then hydrated in distilled water.

Sections are first stained with Mayer's haematoxylin for 5 minutes followed by a wash under running tap water for 5 minutes. They are then stained with eosin for 5 minutes and briefly rinsed with water. Subsequently, the sections are dehydrated through a series of alcohols, submerged in clearing agent and finally mounted in Pertex.

2.16.2. Staining of elastin with Elastic Van Gieson (EVG)

The second section and every tenth section after that were stained with EVG, which stains elastin as black, collagen as red, cell nuclei as black, and other tissue elements as yellow.

After deparaffinisation and re-hydration, the slides are stained with freshly prepared Verhoeff's solution (20ml of 5% alcoholic haematoxylin, 8ml of 10% ferric oxide, and 8ml of Weigert's iodine solution) for 30 minutes. At that stage the entire glass slide is completely black. Slides are then washed 3 times using tap water and then treated with freshly prepared 10% ferric chloride (10 g of ferric chloride in 100 ml distilled water) to differentiate the tissue for 1-2 minutes until the colour of the glass slide returns to normal, elastic fibres in the tissue remain black and tissue background is grey. Washing with tap water stops the differentiation process when tissue staining reaches desired intensity. Subsequently, slides are treated with 5% sodium thiosulfate for 1 minute and washed under running tap water for 5 minutes. The sections are then counterstained with Van Gieson's solution (TCS Biosciences, HS 780-100) for 3 minutes, dehydrated through 3 washes in clearing agent (XTF Clearing agent, Cell Path, SEA-2000-00A) and mounted using ExPert XTF Mounting medium (Cell Path, SEA-1904-00A).

2.16.3. Staining of *Mtb* bacilli with Ziehl-Neelsen (ZN or acid-fast)

The third section and every tenth section after that were stained with Ziehl-Neelsen (or acid-fast stain) for visualising *Mtb*-bacilli present in TB lung granulomas. The tissue is first deparaffinised and hydrated as described before. Slides are then placed in carbol fuchsin for 10 minutes followed by a rinse in 70% alcohol and a 2-minute wash under running tap water. Tissue is then differentiated in 1% acid alcohol for 30 seconds. The last two steps are repeated (if needed) until the background is a pale pink. Sections are then washed in running water for 5 minutes. Commercially available blue counterstain is applied, freshly diluted 1:20 with reverse-osmosis water and then a 1-minute wash in running tap water followed. Sections are then de-hydrated again and mounted with a glass cover slip using Xpert mounting media.

2.17. Immunohistochemistry (IHC) of human lung biopsy

One more section was taken off the biopsy and immunostained for various molecules one at a time through repeated cycles of stripping and staining. This staining was performed by Monette Lopez for us as a service in the Wessex Investigational Sciences Hub (WISH) laboratory on the automated digital pathology system.

The section is first deparaffinised, hydrated and then pre-treated with heat-induced epitope retrieval (HIER) FLEX Target Retrieval Solution (TRS), High pH (*Dako Denmark A/*S, code: K8004). It is then blocked for endogenous peroxidase activity for 5 min using FLEX Peroxidase-blocking reagent (*Dako Denmark A/*S, code: SM801). EnVision^{TM} FLEX Wash Buffer (20x) (Code: K8006) is used to wash between the steps. During the next step, the section is treated with the respective antibody. Next, Dako EnVision^{TM} FLEX/HRP detection reagent (code: SM802) is applied for 20 min along with Dako AEC Red Substrate Chromogen for 30 min for detection. Nuclear counterstaining (blue) is achieved using Dako EnVision™ FLEX Hematoxylin (code: SM806).

CD4 immunostaining is with FLEX Monoclonal primary mouse anti-human-CD4 antibody (*Dako Denmark A/*S, clone: 4B12, isotype: IgG1 kappa, Code: M7310) diluted from concentrated (1:40-1:80). CD8 immunostaining is performed using FLEX Monoclonal primary mouse anti-human-CD8 antibody (*Dako Denmark A/*S, clone: C8/144B, isotype: IgG1 kappa, Code: IR623) at a dilution of 1:40-1:80. For CD103 immunostaining monoclonal primary rabbit anti-human-CD103 (or anti-Integrin alpha E) antibody (RabMAb, abcam, clone: EPR4166(2), isotype: IgG, Code: ab129202) diluted by 1:500 is used. Monoclonal primary mouse anti-human-Ki-67 antibody (*Dako Denmark A/S*, clone: MIB-1, isotype: IgG1 kappa, Code: IR626/IS626) at a dilution of (1:150) is used for Ki-67 immunostaining. Granzyme B immunostaining is performed with FLEX monoclonal primary mouse anti-human-Granzyme B antibody (*Dako Denmark A/*S, clone: GrB-7, isotype: IgG2a kappa, Code: M7235) diluted from concentrated (1:25-1:50). PD-1 (Programmed cell Death protein-1) immunostaining is with monoclonal primary mouse anti-human-PD-1 antibody (*Dako Denmark A/*S, clone: NAT105, isotype: IgG1 kappa, Code: ab52587) diluted by 1:50. Finally, staining for PD-L1 (Programmed cell Death-Ligand 1) is performed using FLEX Monoclonal primary rabbit anti-human PD-L1 antibody (*Cell Signaling Technology*, E1L3N™, isotype: IgG, Code: 13684) at a dilution of 1:200.

2.18. Microfocus X-ray Computed Tomography (μCT) imaging

For μCT imaging, the Nikon Med-X micro-CT scanner was used, which is the first prototype of Nikon's new series of scanners (*Figure 27*) and is optimised for biomedically relevant low-contrast specimens, such as unstained biological tissues. It is equipped with a 130 kVp X-ray source, a 2 x 2k flat panel detector and can image samples up to 0.3 cm in size and 15 kg in weight. This machine can offer up to ~3 μm spatial resolution. To put this into perspective, a typical clinical X-ray CT scanner offers spatial resolution in the order of 0.25-1.50 mm.

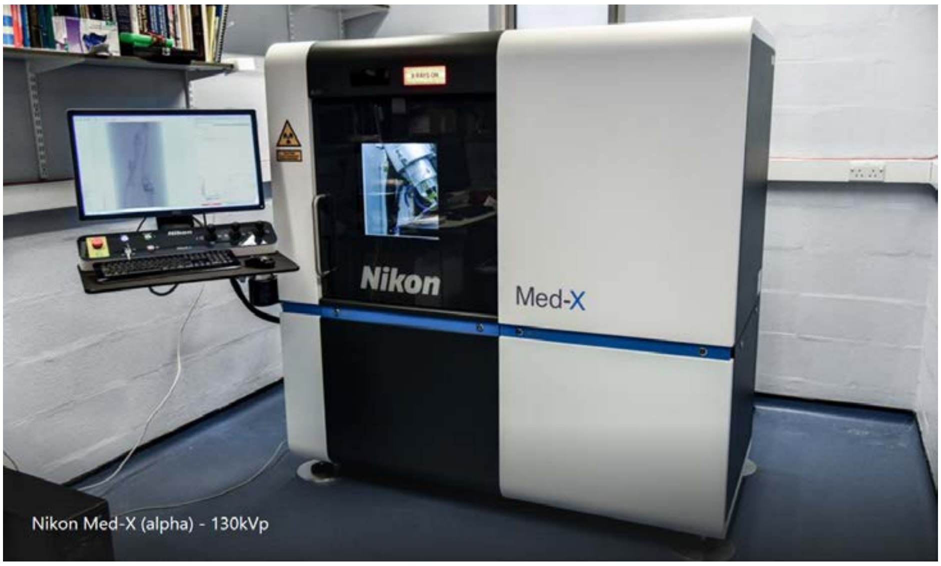

Figure 27. Nikon Med-X (alpha) micro-CT scanner (μ-VIS X-ray imaging centre, University of Southampton)

The Nikon Med-X prototype for microfocus X-ray Computed Tomography imaging (micro-CT) in the University Hospital Southampton (UHS) managed by the μ-VIS X-Ray Imaging Centre, which is based in Engineering, Highfield campus, University of Southampton.

(*Source: μ-VIS X-ray Imaging Centre website - Equipment*)

An unstained FFPE lung biopsy from a patient with active TB was scanned in Med-X using an acceleration voltage of 55 kV_p, a 131 μA current, and 2000 ms exposure time. Total scan time was approximately 6 h and 30 min. A total of 2501 projections were acquired over a 360°-rotation and 4 frames per projection were averaged in order to improve SNR. Source-to-detector distance was 992 mm and source-to-object distance was 21.3 mm resulting in a voxel (3D pixel) size of 4.3 μm.

A resin block of day 14 of infection, alginate-collagen microspheres containing H37Rv-infected PBMCs was first stained with heavy metals (intended for TEM imaging) and then scanned in Med-X at an acceleration voltage of 40 kV_p, a current of 172 μA, and an exposure time of 3500 ms. Total scan time was approximately 7 h. A total of 3141 projections were acquired over the 360°-rotation with 2 frames averaged per projection.

Source-to-detector distance was at 992 mm and source-to-object distance at 13.5 mm producing a voxel size of 2.7 μm.

2.19. 3D image processing of micro-CT scans in Amira

2.19.1. Unstained FFPE lung biopsy micro-CT scan

Three-dimensional image processing is performed in FEI Amira software (version 6.4.0) for 3D segmentation and analysis and in Fiji using an Amira workstation located in the BIU, UHS. The workstations feature a Wacom Cintiq 22HD touch-screen monitor (resolution 1920x1080 pixels), a 24-core Xeon processor, 192 GB of RAM, and a Nvidia Quadro K4200 4GB graphics card.

The 3D lung biopsy dataset is first 'resliced' in Fiji so that the entire block-face is visible on each slice. The orientation with which the lung block is sectioned for histological staining inevitably deviates slightly from the orientation of the 'Resliced' μCT z-stack. Another reason for deviations between the two is that the mechanical force of the razor alone can distort the shape of the lung biopsy sections compared to the uncut block which is what we see in the μCT scan. Therefore, the z-stack also needed to be manually aligned in Amira to match the histology sections' orientation as closely as possible (*Figure 28*).

The 32-bit raw dataset is first converted to 16-bit in Fiji and then opened in Amira (Open Data – Select file – Open – Read complete volume into memory – 16-bit unsigned – Dimensions: 1491, 2000, 441 – big endian – x fastest – Voxel size: 4.3). The 'Slice' tool is then attached to the dataset (Fit to points – Contrast: 0.7333 – Plane parameters: 3 points – Options: show dragger at all 3 points – Plane definition: ON – Display options: Expand). Each dragger is placed on a distinct feature of the biopsy (a blood vessel, an airway etc.). A 'Resample Transformed Image' is attached to our file. The main file is selected as 'Data' and the 'Slice' as 'Reference' (Interpolation: Lanczos – Mode: cropped – Padding value: 0). Transformed file is saved as 'Raw'.

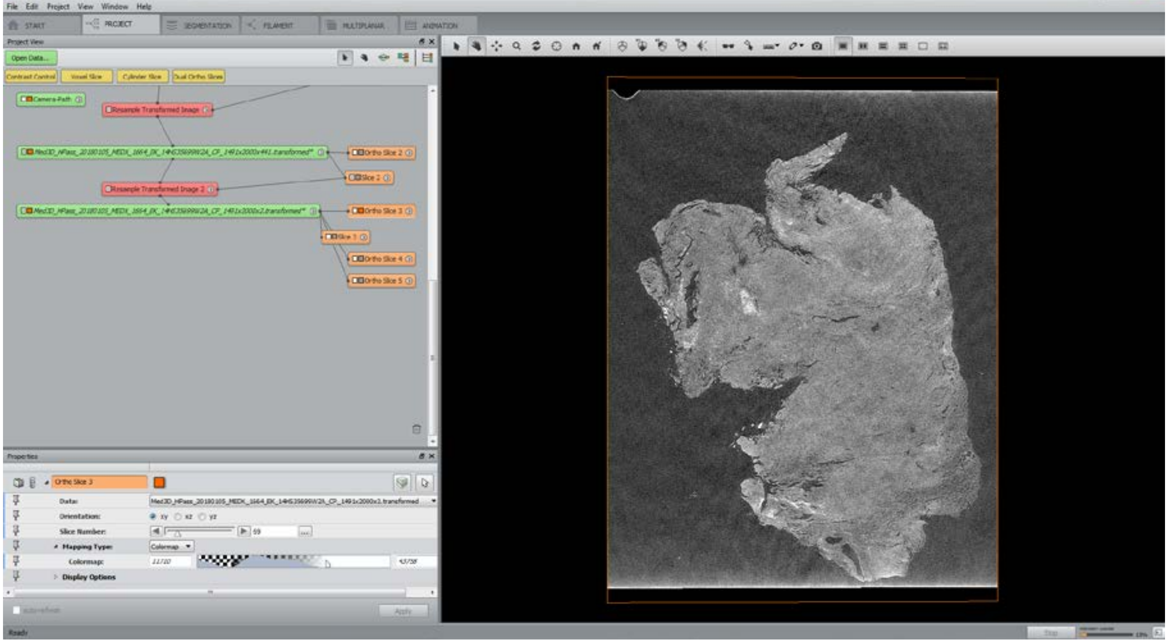

Figure 28. 3D Image processing of lung biopsy micro-CT scan in Amira.

Screenshot taken from the Amira 6.4.0 workflow showing the steps in aligning the block-face of the μCT scan to the H&E-stained sections as closely as possible.

2.19.2. Heavy-metal-stained, resin-embedded microspheres micro-CT scan

In the 3D dataset of the microsphere-containing resin block, microspheres containing aggregates are manually segmented as red, PBMC aggregates as blue and single PBMCs as yellow. Three-dimensional rendering of the segmented features occurs using the relevant features of Amira software.

A z-stack is first opened in Amira 6.4.0 and all the different structures in the microspheres are segmented within the ‘Segmentation’ tab. A new label field has to be created for this z-stack (‘New’ - ‘OK’) and then within this label field, three new ‘Materials’ are added by clicking ‘Add’ in the ‘Materials’ section. The materials are renamed (by double-clicking on their name) as ‘sphere’ (red) for the aggregate-containing microsphere matrix, ‘PBMC_aggregate’ (blue) for any PBMC aggregates in the microspheres and ‘single_PBMCs’ (yellow) for the single PBMCs in the microsphere. One ‘material’ is selected at any given time and then using the ‘Brush’ tool the desired area is highlighted and added to the respective ‘material’ by clicking the ‘+’ sign under ‘Selection’ (*Figure 29*).

In order to visualise the finished product of my segmentation, I made three replicates of the label field, labelled each one of them as one of the materials and then attached a ‘Surface View’ to each new label field (R-click – ‘Surface View’). A smoothing factor of ‘5’ was applied to smooth the curved outer surfaces for aesthetic purposes and the ‘Surface View’ corresponding to the microsphere matrix was rendered partly transparent to reveal single PBMCs and aggregates within the microsphere.

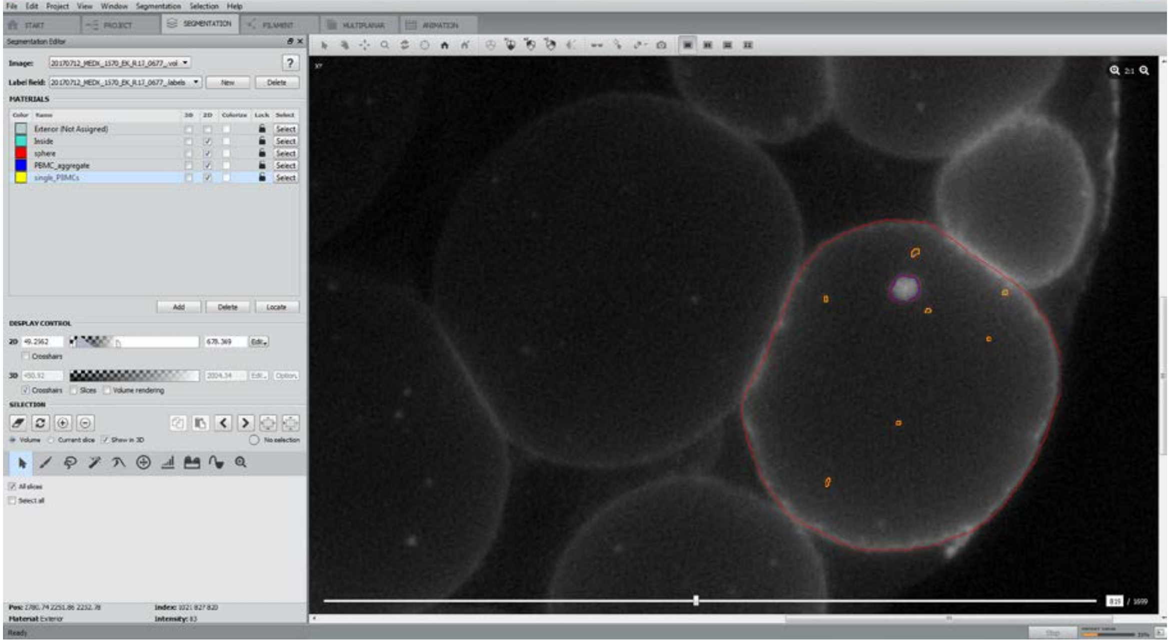

Image: 20170712_MEDX_1570_EK_R17_0677_vol

Label field: 20170712_MEDX_1570_EK_R17_0677_labels

Color	Name	3D	2D	Colorize	Lock	Select
⬜	Exterior (Not Assigned)	☐	☐	☐	🔒	Select
🟦	Inside	☐	☑	☐	🔒	Select
🟥	sphere	☐	☑	☐	🔒	Select
🟦	PBMC_aggregate	☐	☑	☐	🔒	Select
🟨	single_PBMCs	☐	☑	☐	🔒	Select

Figure 29. 3D Image processing of microspheres micro-CT scan in Amira.

Screenshot from Amira workflow showing the steps in segmenting single PBMCs (**yellow**), PBMC aggregates (**blue**) and microspheres (**red**).

Chapter 3

-

A systematic study of a human TB lung biopsy

Chapter 3. A systematic study of a human TB lung biopsy

The aim of the following sequence of experiments was to systematically characterise a human tuberculous lung biopsy, derived from a patient during routine clinical care before any antibiotic treatment was administered. The biopsy features well-formed tuberculous granulomas, and the methods employed to study it include both traditional histological staining as well as the emerging technology of micro-CT scanning. The overall aim of this chapter is to define the characteristics of active human TB in the lung using novel and standard imaging, before proceeding to describe the events of early *Mtb*-infection in our *in vitro* 3D cell culture model in subsequent chapters.

3.1. Non-destructive X-ray imaging of lung biopsy using microfocus X-ray Computed Tomography (micro-CT)

The lung biopsy that I studied in this chapter had been removed as part of routine clinical care for work-up for suspected lung cancer but was identified as showing caseous necrosis and the sample subsequently cultured fully-sensitive *Mtb*. Therefore, it provides a relatively unique clinical specimen to study tuberculosis just as it is developing in the lung. First, I aimed to characterize the overall biopsy, and so it was imaged with micro-CT (*Figure 30*), a technique which uses X-rays to produce a 3D image of a sample in a non-destructive manner. Micro-CT is an emerging methodology and this was the first time it was used on unstained, tuberculous, human lung tissue, to the best of our knowledge. The undeniable advantage of this technique is that it provides a faithful 3D representation of the sample, without the loss of information typically associated with the acquisition of optical sections (*Figure 31*).

The sample was scanned in the first prototype of Nikon’s Med-X micro-CT scanner series and the acquisition lasted 6 h and 30 min resulting in a voxel size of 4.3 μm (2.18.). Subsequent image processing took place in Amira (Avizo) software, whereas alignment and registration of H&E sections onto the micro-CT stack was performed in Fiji.

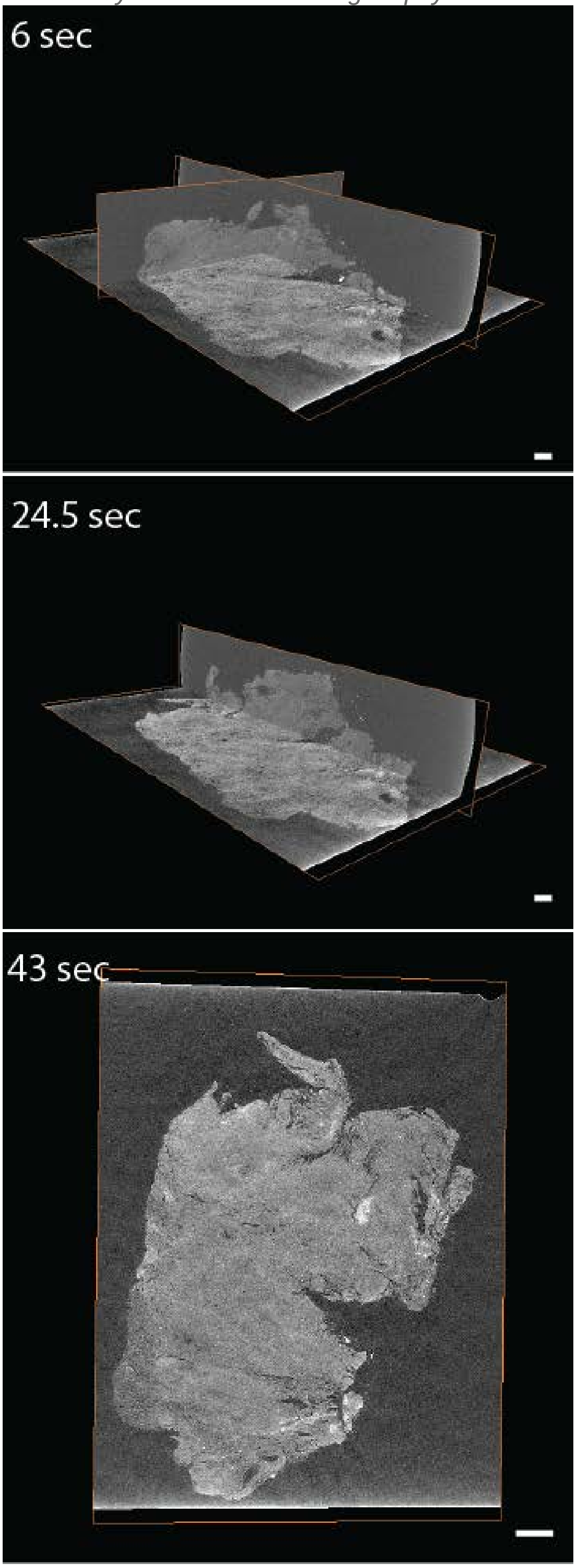

Figure 30. Video of a virtual slice-through of an unstained human lung biopsy micro-CT scan. Video going through the micro-CT scan dataset of the lung biopsy from a patient with active TB (***List of Accompanying Materials***). Still images from the video are selected at 6, 24.5, and 43 seconds. (Scale bar = 800 µm)

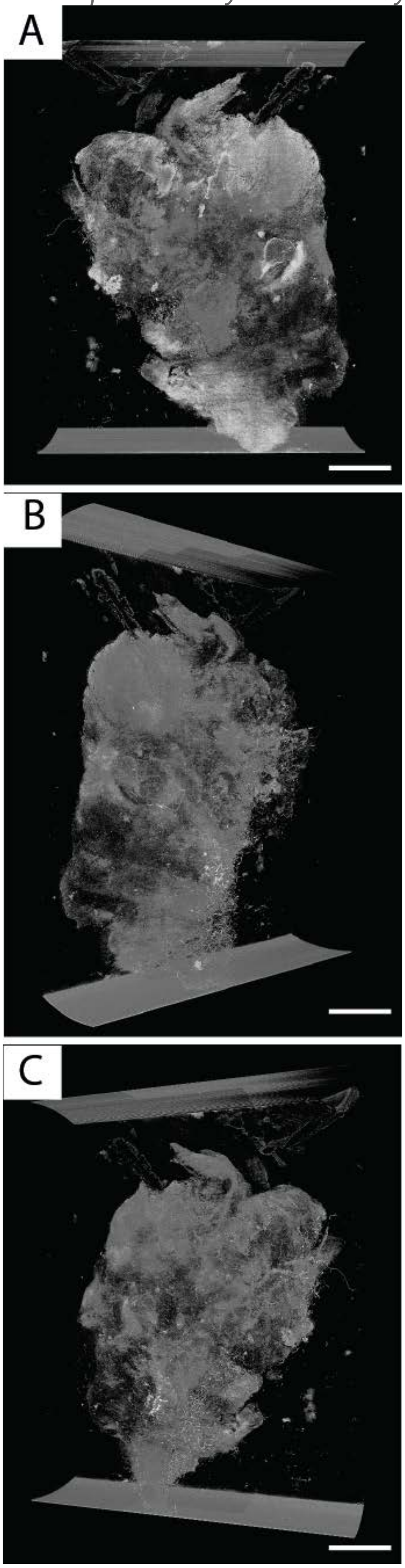

Figure 31. Video of a 3D rendering of an unstained human lung biopsy micro-CT scan rotating by 360°.

Still images from the video were selected at different stages of the rotation (A-0°, B-140°, C-200°). (Scale bar = 2 mm) (***List of Accompanying Materials***)

3.2. Traditional histological staining for tissue components

3.2.1. Haematoxylin & Eosin (H&E)

Next, to correlate the micro-CT appearances with more traditional histological analyses, 100 sequential sections of the biopsy were taken, of which the 1st and every 10th section after that were stained with H&E (*Figure 32*). Haematoxylin stains cell nuclei blue and eosin stains other tissue components, such as the cytoplasm, pink. H&E is the standard pathological stain and can help determine the state of a tissue (i.e. healthy, diseased) as well as identify certain cell types due to their morphology and staining pattern.

A typical human TB granuloma (*Figure 33*) consists of a caseous, necrotic centre with infiltrating macrophages, around which other macrophages, neutrophils and lymphocytes (T-cells and B-cells) aggregate. We also observe MGCs in the granuloma, as well as ‘pockets’ of B-cells with a unknown function around it. This demonstrates the high level of cellular complexity which is not visible in the micro-CT by the analysis done so far.

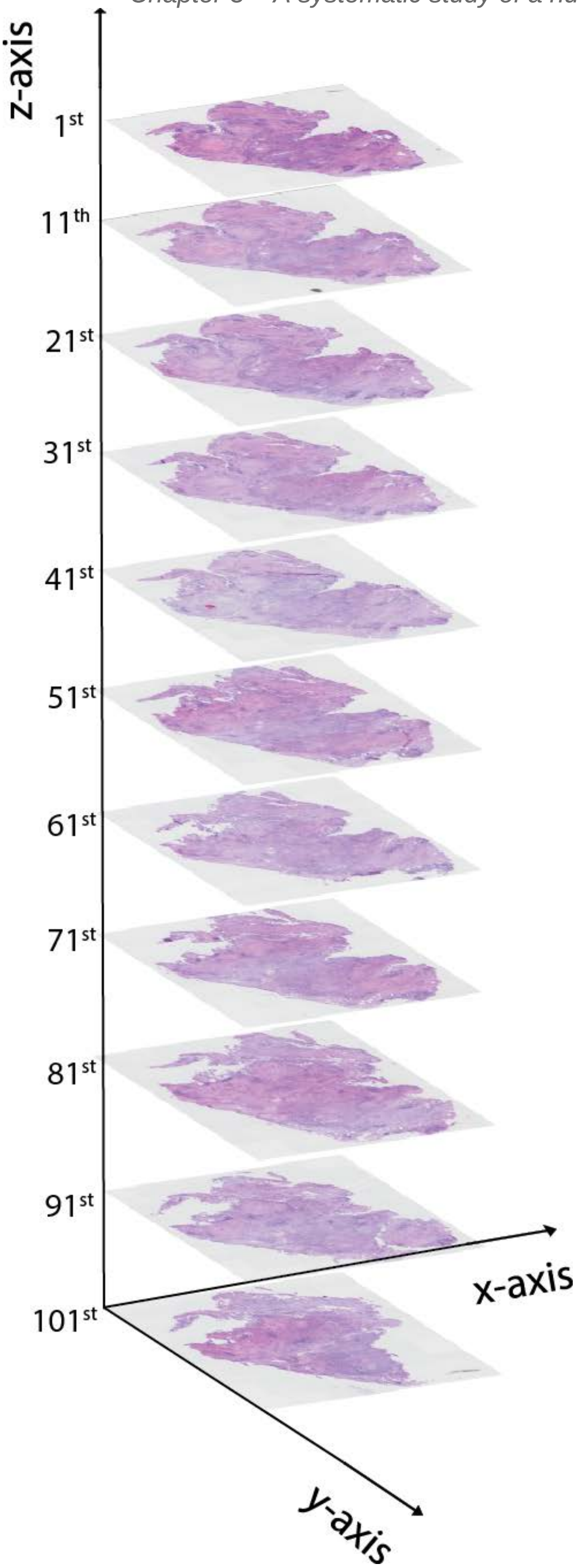

Figure 32. A section 3D stack of the human lung biopsy sections selected for H&E staining. The 1st, 11th, 21st, […], and 101st sections were stained with H&E which stains cell nuclei blue and eosinophilic elements of the tissue (e.g. cytoplasm, proteins) pink. The composite here shows how the micro-CT can be reconstructed enriched with a 3D stack of H&E images for cross-correlation.

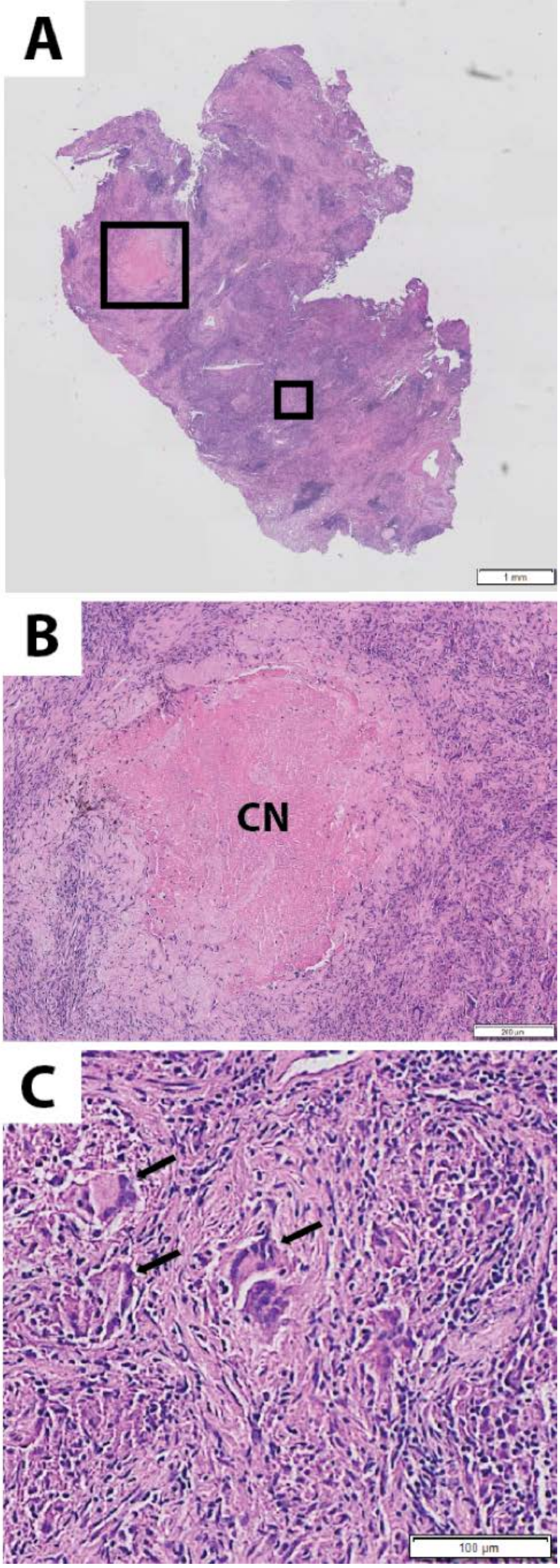

Figure 33. H&E staining of the human TB lung biopsy at low, medium and high power.

Low power view of first section of the tuberculous human lung biopsy containing multiple granulomas stained with H&E (**A**) Large and small **black** squares correspond to the FoV in panels B and C, respectively. In the next panel (**B**), we see part of a large granuloma on the same section at a higher magnification depicting the typical inflammatory infiltrate. **CN**: caseous necrosis. (**C**) **Black** arrows point to MGCs at an even higher magnification.

3.2.2. Elastic van Gieson (EVG)

Subsequently, having characterized the cellular composition by H&E, I was interested to investigate the extracellular matrix composition. The 2nd section and every 10th section after that were stained with EVG, which stains elastic fibres as black, collagen as red, and other tissue components as yellow, so that I could study matrix composition within TB granulomas (*Figure 34*).

EVG staining revealed that this piece of human lung tissue is fibrotic with extensive presence of elastic and collagen fibres (*Figure 35*). The localisation patterns of these two types of fibres is also interesting, as in *Figure 35B* we detect a 'shell' of elastic fibres (**black** lines) marking the outlines of caseous necrotic areas (**grey** patches) at the centre of the granuloma. Outside this elastin 'shell', there are collagen fibres (**pink** lines) intertwined with more elastic fibres. Moving even further away from the necrotic centre of the granuloma, the presence of collagen fibres becomes even stronger and thick collagen fibre bundles surround the entire granuloma. Therefore, there is a progression from collagen absence centrally to fibrosis peripherally.

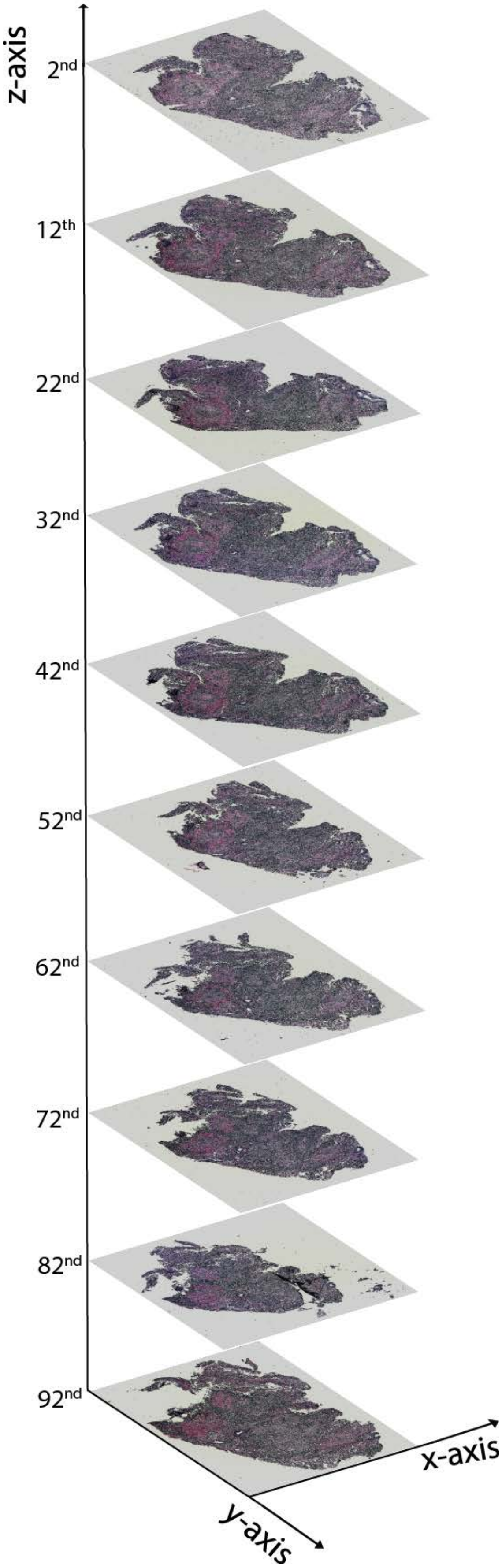

Figure 34. A section 3D stack of the human lung biopsy sections selected for EVG staining. The 2nd, 12th, 22nd, 32nd, […] and 92nd sections of the biopsy were stained with EVG which stains elastic fibres black, collagen red and other tissue elements yellow. The image shows areas of collagen predominance and widespread elastin.

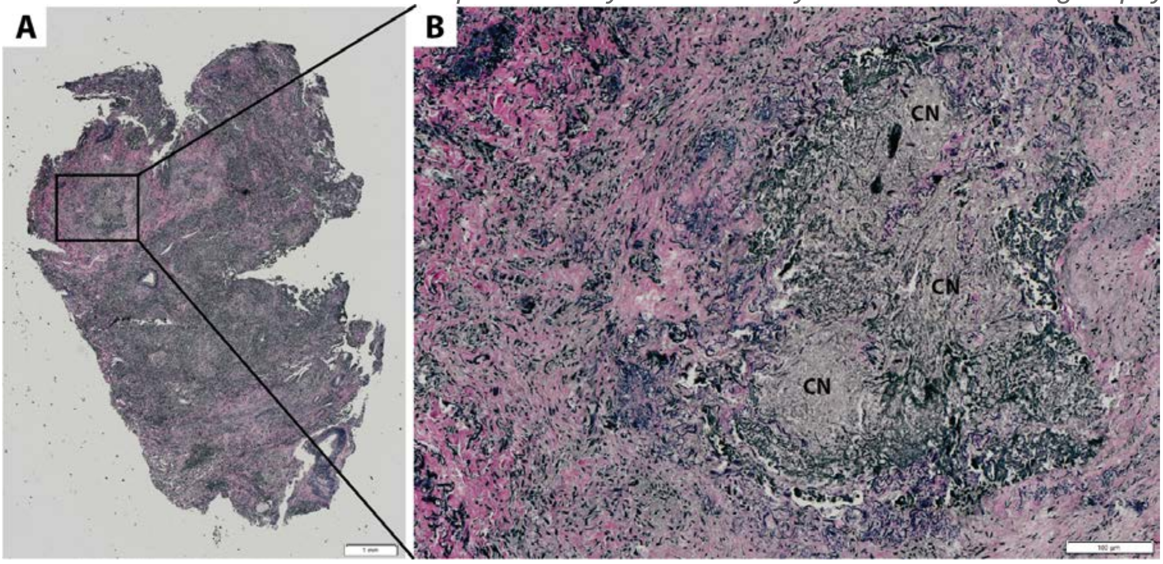

Figure 35. EVG staining of the human TB lung biopsy at low and high power.
Panel **A** shows the first section of the human lung biopsy that was stained with EVG, namely the 2nd section overall. EVG staining revealed a high degree of fibrosis with a strong presence of elastic and collagen fibres. In panel **B**, the area of the caseating granuloma is shown in higher magnification. The homogeneous grey patches in the centre of the granuloma are areas of caseous necrosis (**CN**). Around them, there is a 'shell' of elastic fibres (**black** lines). Further away from the caseous necrotic centre, one can see extensive collagen fibres (**pink** lines) intertwined with more elastic fibres which are absent from the centre of the granuloma.

3.2.3. Ziehl-Neelsen (Acid-Fast)

Having characterized the cellular and extracellular matrix composition of the granuloma, I also stained *Mtb* bacilli using Ziehl-Neelsen (ZN or acid-fast) staining to confirm their presence in the granuloma and to investigate their location and numbers. For that purpose, the 3rd section and every 10th section after that were stained with the acid-fast stain, that labels *Mtb* bacilli as red and then incubation in acid de-stains the rest of the slide, which is then counter-stained as blue.

All ten ZN-stained sections were scanned at a magnification of x20 using an Olympus dotSlide Virtual Microscopy System to locate *Mtb* bacilli in the granulomatous tissue. Bacteria found were extremely sparse, as in some sections only one bacillus (*Figure 36*) or even no bacilli were detected. Considering the extent of inflammation in the tissue sections, this finding seemed contradictory at a first glance. However, it is known that in human TB there is low bacterial load until cavitation occurs, when bacteria replicate freely in the lung tissue cavity.[154,155]

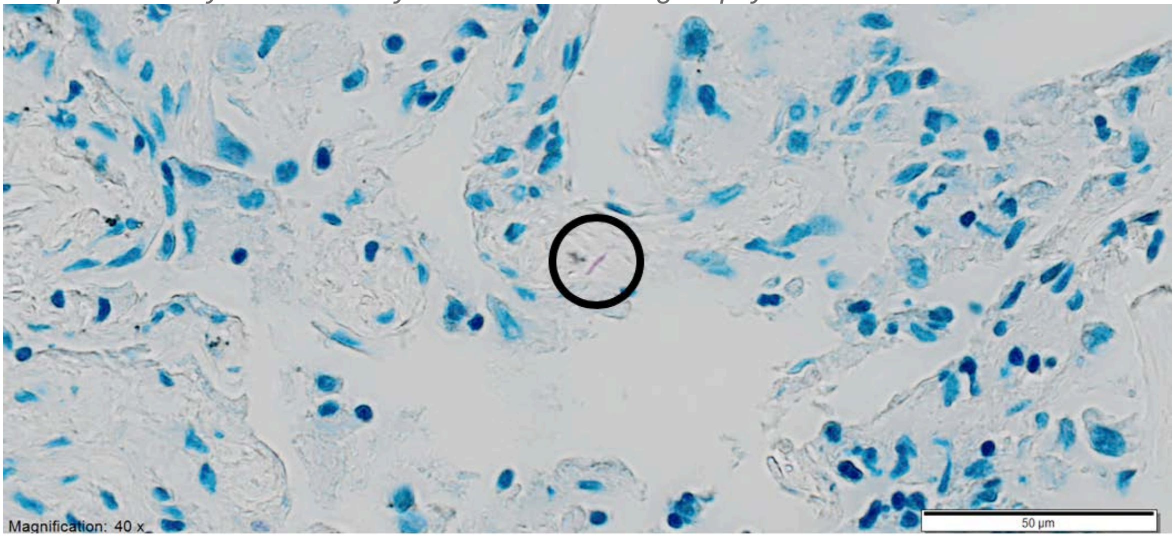

Figure 36. Ziehl-Neelsen staining of the human TB lung biopsy sections showed that *Mtb* bacilli are very sparse within the affected lung tissue.

A single *Mtb* bacillus (inside the **black circle**) found in one of ten ZN-stained sections (scanned at a magnification of x20) of TB granulomatous human lung tissue.

3.3. Immunohistochemistry (IHC) for specific cell markers

After performing the matrix stain, we performed immunohistochemistry staining for various cells markers to gain more information about the localisation of different immune cell subtypes present in the granuloma (*Figure 37*). This staining was conducted by Monette Lopez in the WISH laboratory using protocols developed as part of the experimental cancer research programme and I performed the image analysis. The aim was to further characterize the immune cell repertoire within the granuloma, comparing standard immune staining such as CD4 and CD8 with emerging markers such as programmed-cell death protein-1 receptor (PD-1) and its ligand (PD-L1).[156]

$CD4^+$ cells were extensively distributed around the granuloma (mainly T-helper cells), while weaker staining was observed around its necrotic centre (*Figure 37B*). Relatively fewer $CD8^+$-T-cells were observed within the granuloma (*Figure 37C*), with cytotoxic T-cells around the periphery but definitely immunoreactive. CD103 staining was very sparse (*Figure 37D*), which indicates a heavily reduced population of intra-epithelial lymphocytes that are normally located between mucosal epithelial cells. Granzyme B is a marker of cell cytotoxicity that primarily labels cytotoxic T-cells and NK cells. Staining for this molecule showed the presence of cytotoxic activity mainly within the necrotic centre of the granuloma (*Figure 37E*), but also in other areas of the granuloma and surrounding tissue. Staining for Ki-67, a marker for cell proliferation, was sporadic in and around the granuloma (*Figure 37F*). Almost no PD-1, which is a transmembrane receptor induced during programmed cell death, was found within the centre of the granuloma, however some staining was observed around it (*Figure 37G*). Finally, very strong PD-L1 (Programmed Death Ligand-1) staining was observed in the necrotic centre, as well as other areas in and around it, in the macrophage dominated areas (*Figure 37H*). When PD-L1 (predominantly expressed in macrophages) binds to its receptor (PD-1), it inhibits T-cell activation and leads to tumour growth.[157]

Therefore, this analysis by immunohistochemistry showed that the dominant T-cell type was $CD4^+$, but there is a definite $CD8^+$-T-cell population, and there are minimal intra-epithelial lymphocytes. Expression of the proliferation marker Ki-67 is low, whereas Granzyme B is expressed throughout the granuloma. The PD-1/PD-L1 axis is expressed, with high PD-L1 in the macrophage areas and PD-1 in the T-cell dominated rim. Further analysis to perform co-localisation will determine the cell type expressing PD-1, and staining with a macrophage marker such as CD68 would be necessary to definitely prove that macrophages are expressing PD-L1, though morphometric appearances certainly suggest this.

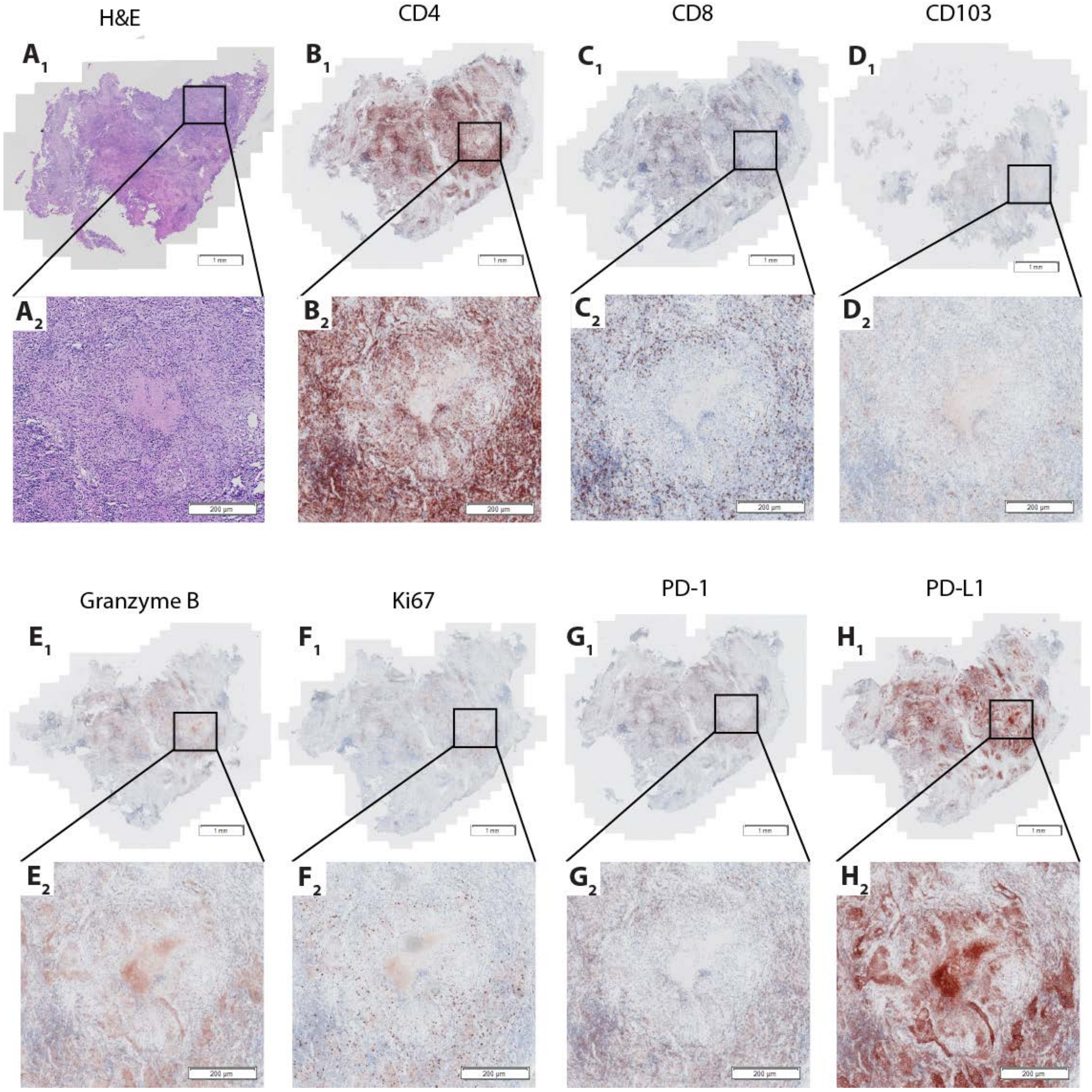

Figure 37. Immunohistochemistry staining of a tuberculous human lung biopsy for various immunological markers.

Panels **A$_1$-H$_1$** show the entire stained section, whereas panels **A$_2$-H$_2$** show a granuloma in higher magnification. H&E staining is provided for reference (**A$_{1\text{-}2}$**). There is a strong presence of CD4$^+$ T-cells (**B$_{1\text{-}2}$**) and a moderate presence of cytotoxic CD8$^+$ T-cells (**C$_{1\text{-}2}$**) around the granuloma. CD103 staining showed a lack of intra-epithelial lymphocytes in the granulomatous area (**D$_{1\text{-}2}$**). Cytotoxic activity was observed within the necrotic centre of the granuloma as well as in its outer layers and around it, when staining with Granzyme B (**E$_{1\text{-}2}$**). Staining for Ki-67 showed low levels of cell proliferation in and around the granuloma (**F$_{1\text{-}2}$**). No PD-1 was found in the centre of the granuloma but was present in the periphery around it (**G$_{1\text{-}2}$**),whereas its ligand, PD-L1, was shown to have a strong presence both in and around the granuloma (**H$_{1\text{-}2}$**).

3.4. Discussion

In this chapter, I utilised the emerging methodology of micro-CT to image a human lung biopsy from a patient with previously undiagnosed culture-positive pulmonary TB. I optimised the image processing pathway and generated both still images and videos to identify the 3D structure of an unsectioned, unstained lung biopsy taken during the course of routine clinical care. Next, I performed serial sections and stained every 10th section in order to compare the micro-CT images to standard histological staining such as H&E and EVG. Image processing for registration of the histology sections onto the micro-CT stack was performed manually and was quite laborious and time-consuming as it had to be repeated for each individual section. I performed the initial steps in this cross-validation (data not shown), but further analysis is needed to yield more information about how the micro-CT findings relate to the traditional histological sections.

Whilst human CT scanning has been present since the 1970s and is a standard test to investigate for human disease such as cancer, imaging of very small histological sections has only recently become available due to technical advances. I was lucky to have access to the first of Nikon's prototype micro-CT scanner that is set up for imaging unstained tissue blocks. The scan time of our lung biopsy was 48 hours, showing the time it takes to collect a high-resolution 3D image of an entire sample of this size. A future goal for this methodology is for it to be used intraoperatively to complement traditional histological imaging. However, one of the problems about imaging a solid lesion such as a tuberculous lung biopsy is the relative lack of contrast between different tissue components as they are all cellular. It is relatively easy to distinguish structures when there are air pockets, such as in the lung, or a hollow lumen, such as in the gut. Therefore, my work identified some of the emerging challenges.

Despite this, I was able to identify several of the histological features on the micro-CT (data not shown, as analysis was not complete at the time) which I then confirmed by H&E staining. I was able to visualise areas of caseous necrosis and also areas of calcification which could potentially be of use as 'anchor' points in subsequent image analysis. The strength of the system is that one can visualise an entire 3D structure without going through the destructive and invasive steps of histological processing and image reconstruction, and also, that one can gain an impression of how different granulomas relate to each other within a 3D composition. Ideally, my next steps would be to determine how the Hounsfield Unit values within the micro-CT relate to the more standard stains such EVG, so I can then start to more accurately map out the caseous, cellular and collagen-rich areas within the micro-CT stack. This will be one of my goals in the postdoctoral position that I have taken up in the Biomedical Imaging Unit.

The analysis of these section 3D stacks showed that a human lung granuloma is much more complicated than the cartoons depicted in scientific journals (*Figure 3*). A typical review paper will suggest that there is a simple, clearly defined structure with a caseous centre, surrounded by lipid-laden macrophages and then by more peripheral T-cells and fibroblasts.[25,158,159] In reality, a human lung granuloma is a much more complex and disorganised melee of inflammatory cells, necrosis and fibrosis. Therefore, any emerging interventions, such as host-directed therapy, need to be considered within the complexity of such a 3D structure as opposed to the more simplistic scientific paradigms. This conclusion justifies the approach I took of combining the traditional and emerging imaging modalities.

I specifically investigate the extracellular matrix by Elastic van Gieson staining because this has been one of the research interests of the group.[1,61,160] I showed that while collagen was absent from the caseous necrosis but present in its periphery, as previously described,[161] elastin was quite widely present throughout the granuloma. The historical literature suggests that the process of cavitation occurs because of liquefaction of the tuberculous granuloma, and this was thought to be due to elastin breakdown.[162] Although this work is all from classical studies in the rabbit model of TB, which may not fully reflect human disease, my findings seem to support the notion that elastin may hold the granuloma together initially and elastin breakdown may be a key step in the formation of cavities. Our group has previously reported that collagen degradation is an early event in TB pathogenesis and precedes cell death, so my findings on collagen distribution are consistent with this conclusion.[1]

I also performed immunohistochemical analysis for specific markers in order to try to integrate and correlate micro-CT imaging, standard histological stains and immunohistochemical stains. I showed that $CD4^+$ cells were widely present throughout the granuloma, and there was a definite presence of $CD8^+$ cells, as previously described.[163] The interesting finding was that PD-L1, the macrophage-expressed ligand for T-cell PD-1, was very extensively expressed across the granuloma. This suggests that in the context of TB, the persistent stimulus leads to the host macrophages upregulating the ligand which will downregulate T-cell activity. Whilst in the traditional paradigms of human TB this would lead to an inadequate immune response, the recent description of TB reactivation after immune-checkpoint inhibition treatment for cancer would suggest this is actually a homeostatic mechanism whereby PD-L1 is protecting the lung.[164,165] Therefore, over-activation of the immune system in the context of PD-1 for inhibition of the cancer may be just as harmful as inactivation of the immune system by immunosuppression such as HIV or anti-TNF treatment.[2]

Next, I performed Ziehl Neelsen staining to quantitate TB presence. It is striking that there are relatively few bacteria identified causing extensive inflammation. It has been well described that there is a high bacterial load in mouse models,[166] whereas relatively sparse bacteria in human TB until cavitation occurs.[167] How so few bacteria cause inflammation of such extent is poorly defined, and emerging concepts within the field are that this may be either an autoimmune reaction[168] or a loss-of-tolerance process leading to this inflammation.[169] Therefore, simply combining standard staining with immunostaining helps support different concepts of human TB immunopathology and further confirms how few mycobacteria cause such extensive inflammation.

The systematic study of the human lung biopsy by emerging and traditional tissue imaging approaches offers insight into tuberculosis infection in humans. It represents, however, a mere snapshot of the disease taken at the point that lung pathology was developing. In order to elucidate the early stages and mechanisms of TB infection *in vitro*, we need to also investigate advanced cell culture models so that we can dissect the pathological process. We have developed a ‘microsphere’ 3D cell culture model in our group over the last 8 years.[97,98] In the next chapter, I will describe how I applied label-free imaging techniques to image *Mtb* infection in the microspheres to develop assays that can be used to study the effect of different interventions.

Chapter 4

-

Label-free spectroscopy and imaging of microspheres

Chapter 4. Label-free spectroscopy and imaging of microspheres

The overarching theme of my thesis is to compare emerging and established imaging methods to study TB. Having imaged a lung biopsy from a patient with incipient TB, the complementary step was to image the 3D microsphere system developed by our team.[1,77,97,98] The first group of emerging methodologies I used to achieve that were label-free chemical characterisation and imaging techniques; Raman spectroscopy, Coherent Anti-Stokes Raman Scattering (CARS), Second Harmonic Generation (SHG), and Two-Photon Excitation Fluorescence (TPEF) microscopy. CARS imaging targets a single Raman frequency and is commonly used for lipid imaging. With SHG I imaged collagen fibres in the microsphere matrix and TPEF was used to detect autofluorescence from the alginate in the microspheres. I used custom-built setups for CARS, SHG, and TPEF all developed in my co-supervisor's group.[170-172]

Raman spectroscopy was used to identify the 'fingerprint' Raman spectra of our microspheres as well as the ingredients used to generate them. Each peak in a Raman spectrum can be associated with a specific molecular vibration of a chemical bond, therefore, useful information about the chemical composition of a sample can be extracted from it. I then went on to use CARS to monitor PBMC aggregation in microspheres and SHG to characterise collagen fibre localisation in the extracellular matrix, which I then compared to standard imaging by confocal microscopy.

4.1. Characterisation of the 3D matrix by Raman spectroscopy

I first used Raman spectroscopy, a label-free chemical characterisation technique, to characterise the 3D microsphere matrix, starting with its individual components. I then proceeded to characterise the different states of alginate (powder, gel and microsphere) and tried to detect the presence of collagen in the 3D matrix. All Raman spectra are plotted as 'counts' in arbitrary units (y-axis) against wavenumber in cm^{-1} (x-axis). The process of optimising the acquisition and spectral analysis parameters is described in *Chapter 2.*.

4.1.1. Background Raman spectrum

Since all samples are placed on a quartz cover slip in order to be characterised with Raman spectroscopy and are immersed in HBSS (with or without phenol red), I first needed to determine what the contribution of these two components was on the Raman spectrum, if any. The two spectra show the same pattern, without any distinct peaks that would affect our samples' spectral signature. The spectrum of HBSS has lower intensities overall and that is due to the fact that it is partially "blocking" the signal that originates from quartz, without contributing with a characteristic signal of its own (*Figure 38*). The features appearing below 600 cm^{-1} seem to be artefacts most likely due to autofluorescence of certain glass parts of the microscope (e.g. objective or other lenses). For that reason, all subsequent spectra were acquired with a minimum wavenumber of 590 cm^{-1}.

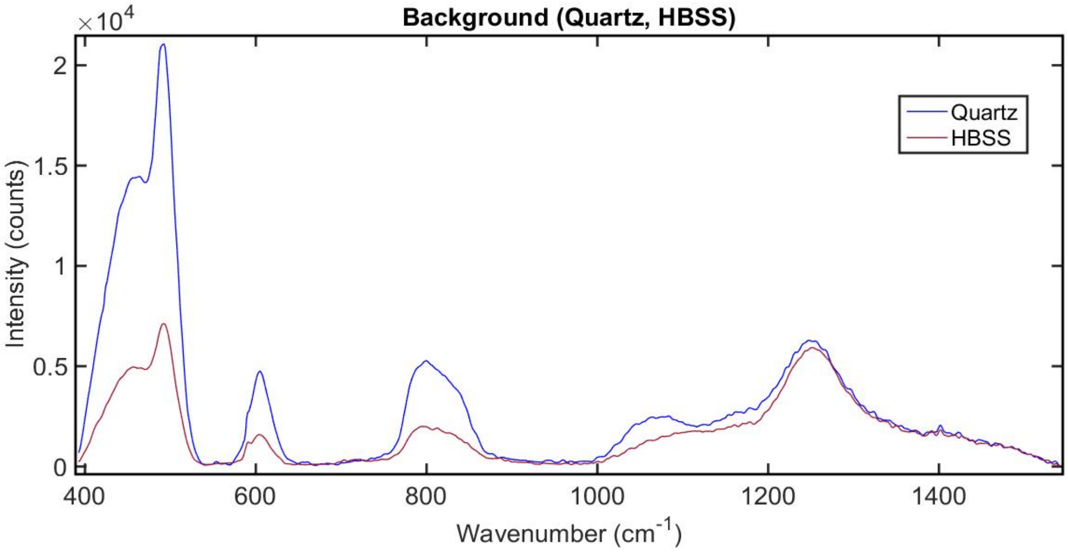

Figure 38. Static Raman spectra of the quartz cover slip (blue) and HBSS with phenol red (red).

Acquisition parameters: x50/0.50 NA Long Working Distance (LWD) objective, 100 mW·sec (as per **Equation 5**). This objective was used in this measurement as the x50/0.75 NA SWD objective was not available. All subsequent measurements were made using the 0.75 NA objective which was shown to acquire higher signal intensities. HBSS shows no contribution in the Raman signal detected except for partially masking the Raman spectrum of quartz, on which it is loaded for Raman spectroscopy.

4.1.2. Characterisation of alginate

After establishing the contribution of the background in our Raman spectra, I investigated whether characterisation of the raw materials used to make the microspheres is possible with Raman spectroscopy. I first compared two different alginate powders from different companies (Sigma-Aldrich and Novamatrix) that have a very different composition and purity to see whether I can successfully distinguish between them (*Figure 39*) and then, I compared the powder and microsphere forms for each of the two different alginates (*Figure 40*, *Figure 41*). One of the alginates used was an ultrapure alginate supplied by Novamatrix (PRONOVA UP MVG) and had a viscosity of 267 mPas and a guluronic acid (G) content of 67%. It also had less than 24 EU/gr of endotoxins. The second alginate tested came from Sigma-Aldrich and had a viscosity of 5-40 mPas and a guluronic acid (G) content of 39%. It also contained unknown concentrations of endotoxins and other impurities, being a relatively low-purity product for general use.

As mentioned in the *Introduction*, alginate comprises of two different homopolymeric (MM, GG) and one heteropolymeric (MG) subunits. Peaks 2, 4 and 6 (810 cm^{-1}, 888 cm^{-1}, 955 cm^{-1} respectively) are indicative of the presence of guluronic (G) and mannuronic (M) acid residues and are present in all alginate Raman spectra. Peak assignment for the most prominent peaks of Novamatrix alginate powder is shown in *Table 1* and for the Novamatrix alginate microspheres in *Table 2.*

Different alginate powders

The differences in the Raman spectra of the two types of alginate powder confirm that characterisation of different types of alginate is possible by Raman spectroscopy (*Figure 39*). Some of the impurities in the Sigma-Aldrich alginate-mixture powder, which is known to be of lower purity, emit fluorescence that masks important areas in the fingerprint region of the Raman spectrum and this is why it cannot be used as the 3D cell culture matrix in this study. The ultrapure Novamatrix alginate powder, on the other hand, is almost entirely free of contaminants, which allowed its Raman spectrum to be acquired with minimal interference from fluorescence. It is clear that both spectra correspond to alginate, as they share most of their features. However, there are some significant differences between them due to both the different chemical composition of the two alginates as well as the impurities present in the Sigma-Aldrich alginate.

The ratio of the three peaks (2, 4, 6) that correspond to the M and G residues in the MM, MG, and GG blocks/subunits of alginate (810 cm^{-1}, 890 cm^{-1}, 955 cm^{-1} respectively) differs between the two spectra. In the Novamatrix alginate spectrum, the peaks are progressively lower, whereas in the Sigma-Aldrich alginate spectrum, peak 6 (955 cm^{-1}) is the most prominent of the three. In the wavenumber area between 1000 cm^{-1} and

1150 cm^{-1}, there are very distinct peaks in the Novamatrix alginate spectrum. In the Sigma-Aldrich spectrum the same peaks appear “concealed” by higher levels of background, probably due to fluorescence phenomena from the contaminants present. The equivalent of peak 8 (1240 cm^{-1}) of Novamatrix alginate is also relatively concealed in the Raman spectrum of the Sigma-Aldrich alginate. Peak 9 (1414 cm^{-1}) appears stronger in the Sigma-Aldrich alginate spectrum and the unassigned peak at 1556 cm^{-1} is hardly visible in the same spectrum. Finally, the C-H stretching vibration peak 10 (2940 cm^{-1}) appears slightly shifted to the right (towards higher wavenumbers) in the Novamatrix alginate spectrum.

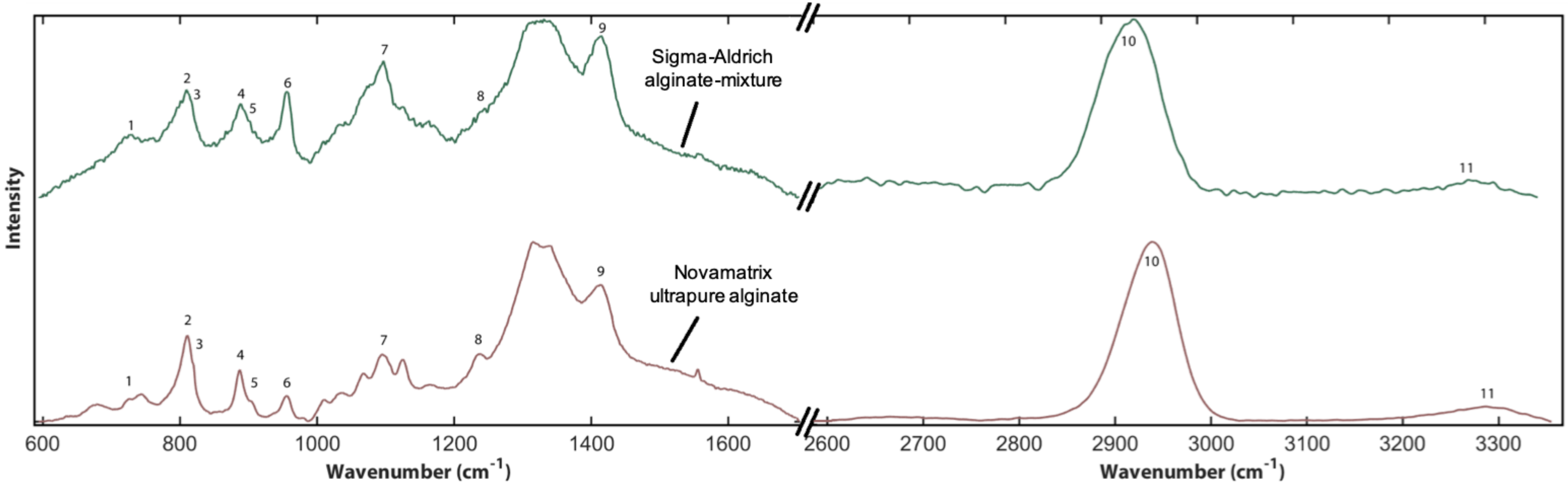

Figure 39. Characterisation of alginate powders from two different suppliers using Raman spectroscopy.

Raman spectra of Sigma-Aldrich alginate-mixture (top spectrum) and Novamatrix ultrapure alginate (bottom spectrum) powders. Total exposure for the Novamatrix alginate: 10,500 mW·sec and for the Sigma-Aldrich alginate: 3,500 mW·sec (as per **Equation 5**). Sigma-Aldrich alginate contains unknown impurities that potentially fluoresce and mask important alginate-specific peaks in the Raman spectrum. Peak assignment for the Novamatrix 'ultrapure' alginate powder can be found in **Table 1**.

Peak assignment for Novamatrix alginate powder			
Wavenumber (cm^{-1})	**Peak morphology**	**Vibrational mode**	**Chemical bond**
726 (1)	small	ring-breathing deformation	M and G residues
810.3 (2)	large	skeletal	C-C
819.7 (3)		-	M residue
887.5 (4)	medium/large	stretching	C-O
903.7 (5)		-	Poly-G fraction
956 (6)	medium	bending	C-C-H, C-C-O
1025	small/medium	-	G residue
1094.5 (7)	large	breathing	glycosidic ring (M residue)
1239 (8)	shoulder/small bump	-	Quartz or alginate
1414 (9)	large, broad shoulder	symmetric stretching	carboxylate
2939 (10)	very large, broad	stretching	C-H
3286 (11)	small/medium, broad	stretching	C-H

Table 1. Peak assignment for the most prominent peaks in the Raman spectrum of ultrapure Novamatrix alginate powder in two wavenumber regions; one ranging from 592 cm^{-1} to 1704 cm^{-1} (centre at 1180 cm^{-1}), and one ranging from 2606 cm^{-1} to 3356 cm^{-1} (centre at 3000 cm^{-1}).

Ultrapure alginate (Novamatrix) imaged as powder and within microspheres

Having characterised the spectrum of Novamatrix 'ultrapure' alginate in powder form, it was next important to study this in microspheres, which was my proposed cell culture platform. I verified by Raman spectroscopy that the signature spectrum of alginate microspheres is the same as the alginate powder spectrum except for a few subtle differences (*Figure 40*). The most prominent difference is the O-H non-hydrogen bonding bending mode, which gives peak 7 (~1635 cm^{-1}) and appears only in the microsphere spectrum. This peak comes from the presence of water, absent from the alginate powder but present in the microspheres.

Another difference between the two spectra is that in the powder spectrum, other peaks tend to have a higher intensity [e.g. 1000-1300 cm^{-1}, 1413 cm^{-1} (peak 6)], most likely because the powder is almost 100% pure alginate, whereas in the microspheres the concentration of alginate is 1.5%. Peak 8 (~2950 cm^{-1}), assigned to C-H stretching vibrational modes due to alginate, appears weakened in the spectrum of the microspheres, again, possibly because of the much lower alginate concentration in the microspheres. In the same spectrum, there is a broad O-H stretching peak at ~3200 cm^{-1} (peaks 9-13), due to the presence of water in the microspheres, which masks the ~3285 cm^{-1} C-H stretching peak.

Peak assignment for Novamatrix alginate microspheres

Wavenumber (cm^{-1})	Peak morphology	Vibrational mode	Chemical bond
811.5 (1)	medium	skeletal	C-C
888.6 (2)	medium	stretching	C-O
958.9 (3)	medium	bending	C-C-H, C-C-O
1096 (4)	very small	breathing	glycosidic ring
1239 (5)	shoulder/small bump		Quartz or alginate
1413 (6)	large, broad shoulder	symmetric stretching	carboxylate
1634 (7)	broad	asymmetric stretching or **non-hydrogen bonding bending**	carboxylate or **O-H**
2943 (8)	large, broad	stretching	C-H
3133 (9)	shoulder	stretching	O-H
3173 (10)	shoulder	stretching	O-H
3200 (11)	very large, broad	stretching	O-H
3213 (12)	very large, broad	stretching	O-H
3238 (13)	shoulder	asymmetric hydrogen bonding bending	O-H

Table 2. Peak assignment for the most prominent peaks in the Raman spectrum of ultrapure Novamatrix alginate microspheres, produced by bioelectrospraying, in two wavenumber regions; one ranging from 592 cm^{-1} to 1704 cm^{-1} (centre at 1180 cm^{-1}), and one ranging from 2606 cm^{-1} to 3356 cm^{-1} (centre at 3000 cm^{-1}).

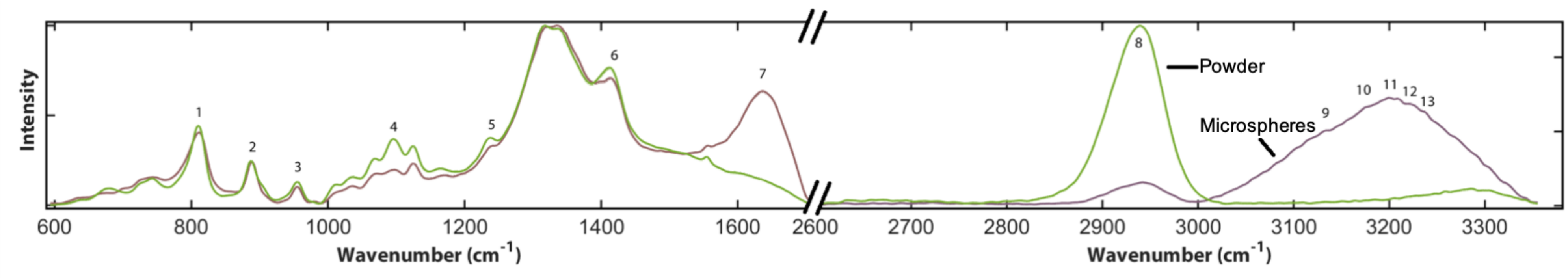

Figure 40. Characterisation of Novamatrix ultrapure alginate using Raman spectroscopy.

Raman spectra of Novamatrix alginate as powder (**green**) and as microspheres (**purple**). Total exposure for both spectra: 10,500 mW·sec. Spectra are normalised with the maximum peak in IRootLab. The two forms of ultrapure Novamatrix alginate can be distinguished by Raman spectroscopy. Peak assignment for the Novamatrix alginate powder in **Table 1** and for the Novamatrix alginate microspheres in **Table 2**.

Alginate-mixture (Sigma-Aldrich) powder and microspheres

Next, I compared the different forms of alginate-mixture (powder, microspheres) from Sigma-Aldrich and investigated their differences with Raman spectroscopy (*Figure 41*). In the microsphere Raman spectrum, there is the large O-H non-hydrogen bonding bending vibrational mode, which gives a peak at ~1635 cm^{-1} due to the presence of water in the microspheres. While some peaks are also present in the powder Raman spectrum, some others were masked by fluorescence (e.g. region 400-700 cm^{-1}). In this case, the dilution of alginate in the microspheres rendered these previously "masked" peaks detectable. Even so, the majority of Raman peaks were not as distinct as in the Novamatrix alginate microsphere spectrum, and therefore the Sigma-Aldrich alginate was not used in our subsequent experiments as a 3D cell culture matrix ingredient.

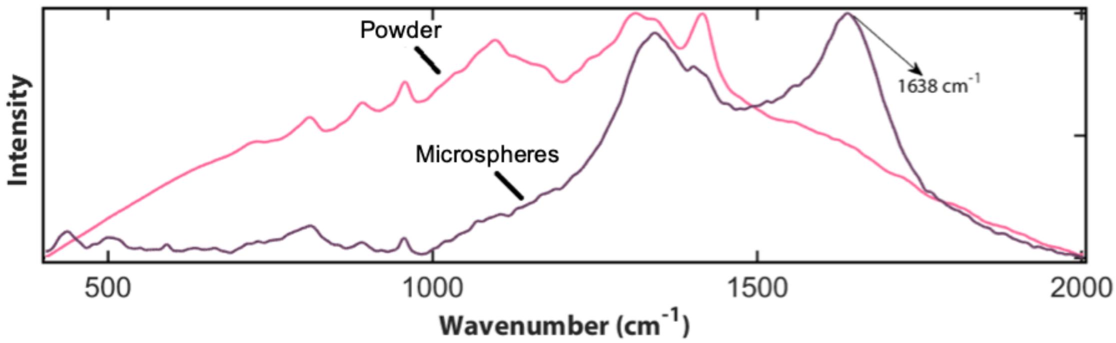

Figure 41. Characterisation of Sigma-Aldrich alginate-mixture using Raman spectroscopy. Raman spectra of Sigma-Aldrich alginate-mixture as a powder (**pink**) and as microspheres (**purple**). Total exposure for both spectra: 1,000 mW·sec. The laser exposure used for these measurements was kept very low due to strong fluorescence interfering with the spectrum which masked Raman peaks important for identification. Spectra are normalised with the maximum peak in IRootLab. Due to its dilution in the microspheres, Sigma-Aldrich alginate reveals some of the peaks in the Raman spectrum that were masked by fluorescence in the powder spectrum. Inconsistent fluorescence interference was observed in the Sigma-Aldrich spectra between different experiments, possibly related to the unknown (in kind and concentration) impurities contained in it. Nevertheless, Novamatrix alginate microspheres show much more distinct peaks, and so this alginate was used as the basis for our 3D cell culture matrix.

4.1.3. Characterisation of alginate-collagen mix

I had successfully characterised alginate both as a raw material and as a component of the microsphere matrix. However, the 3D cell matrix used within the microspheres also contains human type I collagen as its existence in the extracellular matrix is important in regulating cell biology and the host-pathogen interaction.[97] Therefore, with the next set of experiments I aimed to characterise the alginate-collagen mix using Raman spectroscopy to determine if it could be used as a readout of matrix turnover. First, I measured the collagen solution as a raw material and then as part of the alginate-collagen gel and alginate-collagen microsphere matrix. Finally, microspheres of different collagen concentrations were created and subsequently characterised with Raman spectroscopy.

Human collagen I solution

The human collagen I solution we use to make our 3D cell cultures has a concentration of 3 mg/ml, which initially was difficult to detect with conventional Raman spectroscopy. Therefore, in order to detect its Raman signal, I incubated 1 ml of type I collagen solution (3 mg/ml) in a 37 °C incubator for 1 hour until it condensed and turned to a semi-solid state. Another difficulty I faced when performing Raman spectroscopy on the collagen solution (even as a semi-solid) was that, due to the high laser power and exposure time used, it evaporated very quickly without leaving a visible residue, as the collagen concentration was very low. This was overcome by drying collagen solution droplets layered one on top of the other until a visible residue formed on the quartz cover slip. Peak assignment for the most prominent peaks is shown in *Table 3*.

Using Raman spectroscopy, I detected the major protein peaks of amide III and amide I as well as more collagen-specific peaks (*Figure 42*). Collagen spectra have been well characterised previously and typical peaks were identified using these references.[80,173-176] The quartz spectrum is plotted together with the collagen spectrum to show which peaks are due to or influenced by the quartz sample substrate. Having identified the Raman spectrum of our collagen I solution, I later searched for and tried to identify its peaks in our spectra with more confidence (*Microspheres with 3 different concentrations of collagen I*).

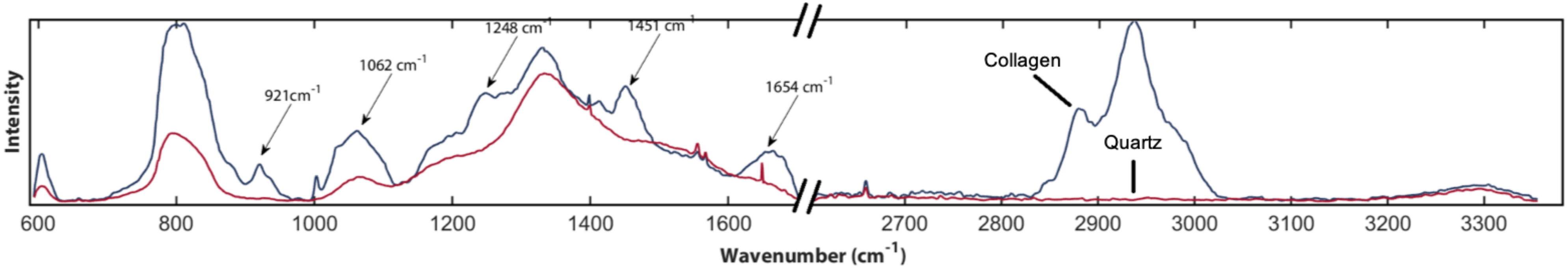

Figure 42. Characterisation of human type I collagen solution using Raman spectroscopy

Raman spectra of dried, type I human collagen solution (~3 mg/ml) (**blue**) plotted with the quartz spectrum (**red**) to show which peaks are purely due to collagen. Total laser exposure: 15,000 mW·sec. The amide I (1654 cm^{-1}) and amide III (1248 and 1332 cm^{-1}) peaks are clearly visible. Full peak assignment for the collagen solution can be found in **Table 3**.

Peak assignment for human collagen I solution (3mg/ml)

Wavenumber (cm^{-1})	**Peak morphology**	**Vibrational mode**	**Chemical bond**
810	medium	stretching	C-C
921	medium	stretching	C-N (proline)
1003	medium	stretching	C-C (phenylalanine)
1062	small, sharp	stretching	C-N (proline)
1248	shoulder	-	amide III
1332	large, broad	-	amide III
1451	small	deformation	CH_2, CH_3
1654	large, broad	-	amide I
		non-hydrogen bonding bending	**O-H (water)**
2937	medium	stretching	C-H

Table 3. Peak assignment for the most prominent peaks in the Raman spectrum of type I human collagen solution (~3 mg/ml) from Advanced Biomatrix in the fingerprint and the C-H stretching regions. The water peaks were identified using data from the following references.[173,174]

Alginate-collagen mix as a gel and as microspheres

Alginate-collagen mix as a gel and as microspheres was successfully distinguished with Raman spectroscopy (*Figure 43*). In the Raman spectrum of the gel (orange), there is an increase in the 1634 cm^{-1} peak, assigned to a water vibrational mode (O-H bending), since water is removed as the microspheres form during bioelectrospraying. Another significant difference between the two spectra is the appearance of three unassigned peaks in the Raman spectrum of the gel at wavenumbers 1017 cm^{-1}, 1044 cm^{-1} and 1067 cm^{-1}.

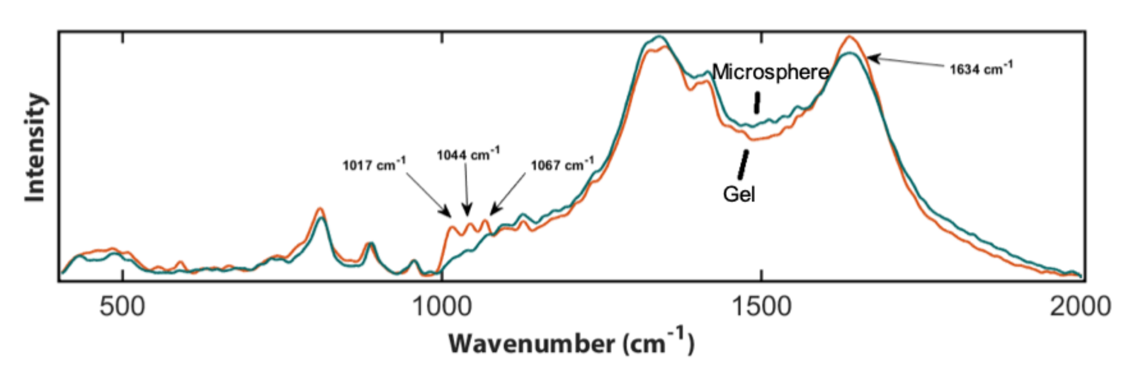

Figure 43. Characterisation of alginate-collagen mix using Raman spectroscopy

Raman spectra of alginate-collagen (1%) gel (**orange**) and alginate-collagen (1%) microspheres (**green**). Total exposure: 10,000 mW·sec. Three unassigned peaks appear in the gel spectrum (at wavenumbers 1017 cm^{-1}, 1044 cm^{-1}, 1067 cm^{-1}).

Microspheres with 3 different concentrations of collagen I

To determine if I could see a dose-response in the spectra, I produced microspheres with different concentrations of collagen (0%, 0.5%, 1%, 1.5%), and then imaged them with Raman spectroscopy. Analysis of these Raman spectra showed that there were no collagen-specific peaks detected in the microspheres and that occurred most likely due to its very low concentration in the microsphere matrix (*Figure 44*) which was lower than the detection limit of the machine.

In the ‘1.5% collagen’ microspheres (**purple**) Raman spectrum, there is a clear shoulder at 1241 cm^{-1} [peak (4)], which could be assigned to the amide III band (characteristic for proteins), and an increase in the 1416 cm^{-1} peak (5), which has been assigned to the symmetric stretching vibration of carboxylate. Another difference in the spectra is that in the same spectrum (**purple**) the unassigned 1568 cm^{-1} peak (6) is much lower in height (almost absent) compared to the rest of the spectra.

As collagen concentration rises in the microspheres, so does peak (7) (1634 cm^{-1}), assigned to the O-H bending mode of water. Also, the very broad peak (9) at around 3200 cm^{-1} appears to be very different in intensity between the four spectra. This is not an indication of the initial concentration of water in the microspheres, but merely the concentration of water in them at that specific time point. The only type of microspheres that initially contained a higher concentration of water was the ‘1.5% collagen’ microspheres. However, when microspheres are exposed to laser light, water from their interior evaporates causing them to shrink and shrivel. Since sometimes more than one spectra of the same microsphere were acquired, the difference in hydration that was detected indicates indirectly the amount of stress they were subjected to due to direct exposure to the laser.

Therefore, I concluded that Raman spectroscopy was useful for characterising collagen when in solid form, but within our microsphere system the concentration was not sufficient for either absolute or semi-quantitation. Consequently, I investigated different non-linear optical imaging methods to determine if they could be applied to the microsphere 3D cell cultures and provide useful biological information.

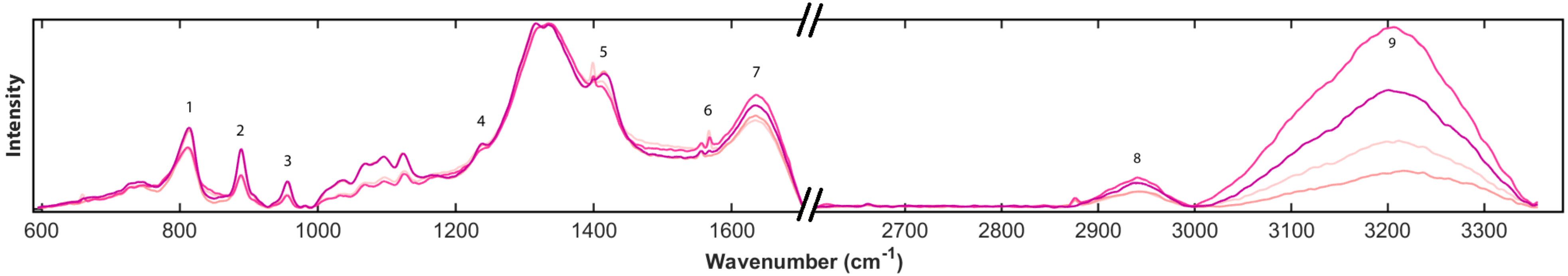

Figure 44. Characterisation of alginate-collagen mix using Raman spectroscopy.

Raman spectra of microspheres with different concentrations of collagen I; **no (0%)**, **low (0.5%)**, **medium (1%)**, **high (1.5%)**. Total exposure: [for the no (0%), low (0.5%) and medium (1%) collagen concentration] 12,500 mW·sec; [for the high (1.5%) collagen concentration spectrum] 10,500 mW·sec. Spectra were normalised with the maximum peak in IRootLab.

4.2. Label-free imaging of 3D cell cultures with CARS and SHG

After chemically characterising the microsphere matrix with Raman spectroscopy, I investigated the potential of label-free imaging techniques (CARS, SHG, TPEF) in the context of the microsphere 3D cell culture model. I first tested SHG microscopy, which detects non-centrosymmetric structures, in imaging collagen degradation in the 3D matrix after infection with *Mtb*. Collagen fibres are particularly SHG-active due to their non-centrosymmetric quaternary structure. Additionally, TPEF microscopy which can detect cell autofluorescence is incorporated in the same imaging platform as SHG and has, therefore, allowed me to simultaneously monitor cell (autofluorescence-TPEF) and collagen fibril (SHG) localisation. Subsequently, I used Coherent Anti-Stokes Raman Scattering (CARS) microscopy to monitor PBMC aggregation during *Mtb* infection by targeting the cell membrane lipid bilayer. CARS imaging is based on detecting enhanced Raman signals due to coherent excitation of molecular vibrations and on this occasion was used to image lipids, for which it is particularly well suited.

4.2.1. Characterising the 3D cell culture matrix with SHG/TPEF

Detection of collagen fibrils

SHG and TPEF imaging were successful in visualising the alginate and alginate-collagen microspheres using a 800 nm pulsed laser. Initially, collagen fibres in the alginate-collagen microspheres were not detected with SHG, as the collagen was either in monomeric form or in very short trimers. However, after overnight fixation of the microspheres in 4% PFA, chemically-induced cross-linking occurred, and collagen fibres became visible (*Figure 45*).

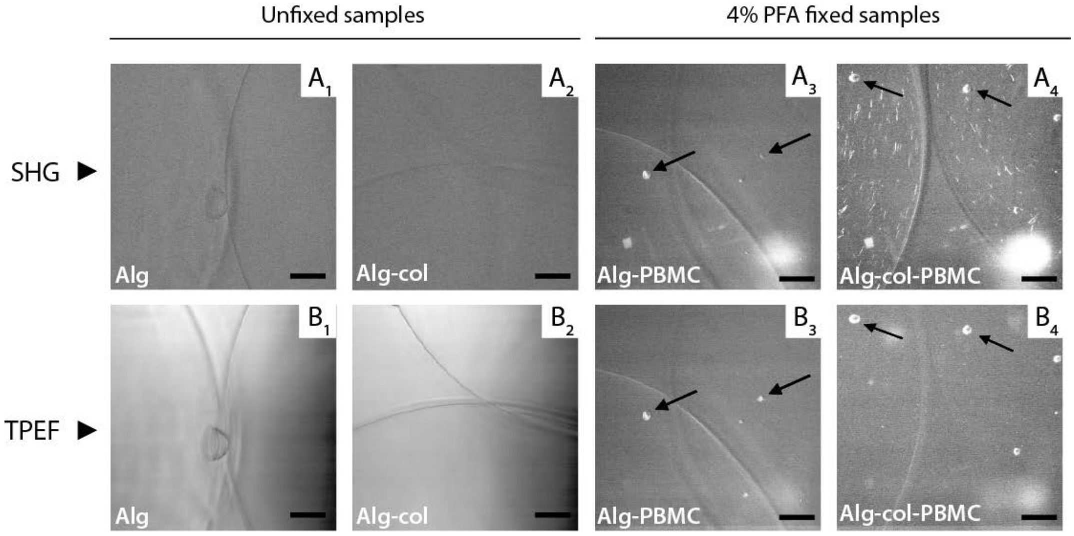

Figure 45. SHG (A_1-A_4) and TPEF (B_1-B_4) images of microspheres with and without PBMCs. **Black** arrows are pointing to PBMCs. Collagen fibres (short white lines) appear in the SHG image of the PFA-fixed microspheres (A_4) but not in that of the unfixed samples (A_2). Scale bar = 25 µm.

Effect of temperature and PFA on the formation of collagen fibrils

The observation that collagen fibrils appeared only in the PFA-fixed samples raised the question of whether cells in our bioelectrospray-generated 3D cell cultures encounter collagen fibres (as they would in a real tissue) or collagen monomers, which were initially incorporated into the spheres. It is known that formalin fixation causes chemical cross-linking of collagen in tissue in a dose-dependent manner.[177] It is also known that collagen spontaneously cross-links and forms fibrils when incubated at 37°C.[178]

Using the same samples on which that observation was made, I studied the formation of collagen fibres after incubating them at 37°C for different times (*Figure 46*). Our standard procedure when making microspheres that contained human cells was to fix them for safety before imaging. We did not need to fix the microspheres that did not contain any cells and so the role of PFA fixation was initially ignored. This is the reason that in this experiment certain controls seem to be missing (e.g. 'fixed alginate', 'fixed alginate-collagen', 'unfixed alginate-PBMC' and 'unfixed alginate-collagen-PBMC'). PFA fixation was identified through the literature as a factor that affects collagen fibre formation only after this experiment was concluded.

Collagen fibres were detected only in the PFA-fixed samples that contained cells and not in the unfixed microspheres without cells. No further change was observed until the last time point (24 h), but this was not systematically quantified as digital analysis of a larger number of images would be required to validate this observation. This experiment does not evaluate the role of PBMC presence in the microspheres in the formation of collagen fibres as essential controls are missing.

Preliminary experiments performed at a later stage revealed that large collagen fibres form in the unfixed microspheres at some point within the first three days of incubation at 37°C but that was not investigated further to determine the exact time-point when large collagen fibres start to appear in the microsphere matrix.

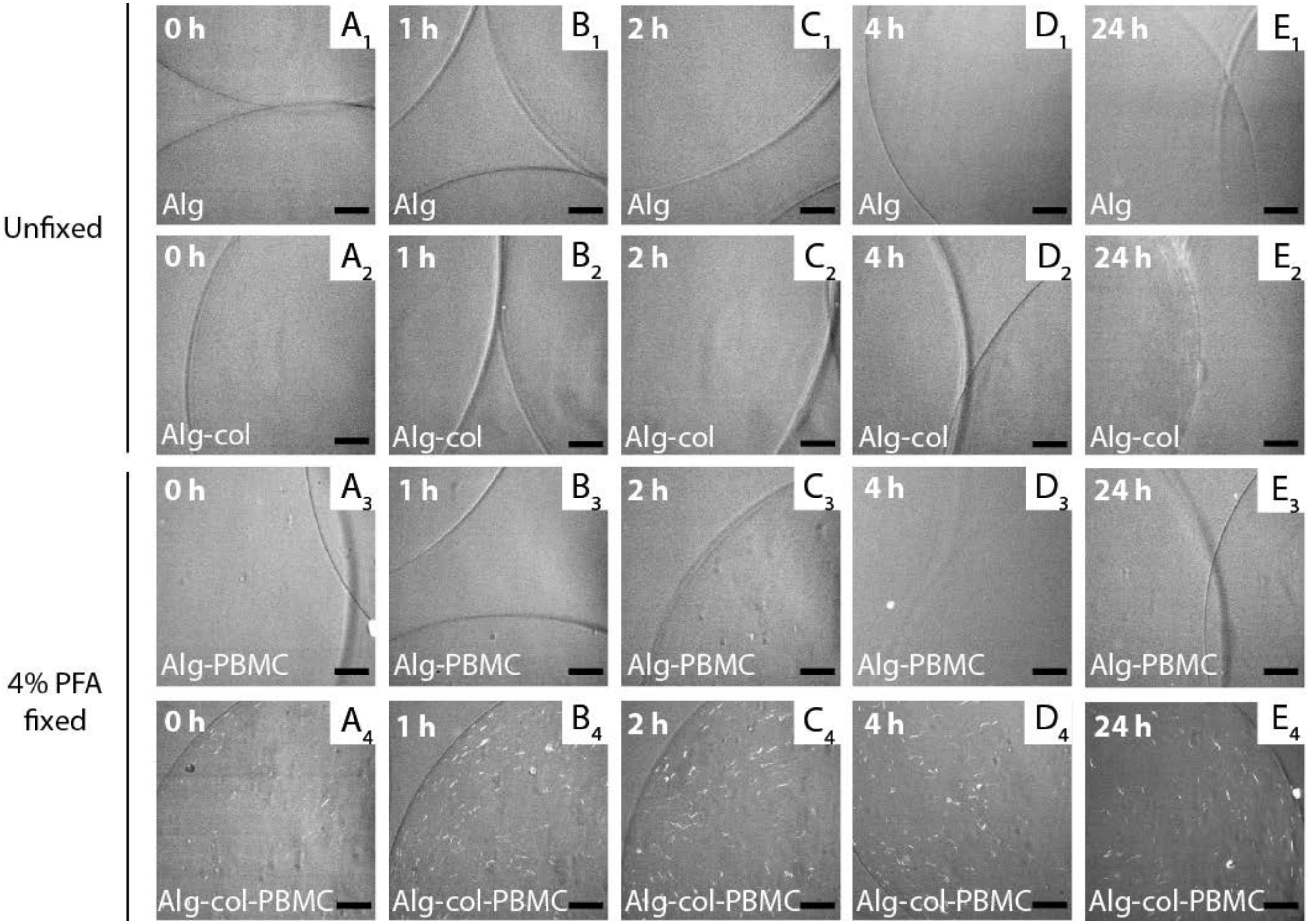

Figure 46. Time-course experiment for collagen cross-linking after different times of incubation at 37°C.

Samples were imaged before incubation (**A_1-A_4**), and then after 1 hour (**B_1-B_4**), 2 hours (**C_1-C_4**), 4 hours (**D_1-D_4**), and 24 hours (**E_1-E_4**) of incubation at 37°C. In the unfixed microspheres collagen fibrils are not detected even after 24 hours of incubation. In PFA-fixed samples collagen fibrils are detected, but no change in their number was observed in the first 24h of incubation. Scale bar = 25 μm.

Selection of a collagen type for the 3D cell culture matrix

SHG was therefore able to detect unlabelled collagen as long as it was PFA-fixed, consistent with using a solution of unlabelled human type I collagen for our microsphere matrix. However, I needed to corroborate any findings from SHG with more established techniques such as fluorescence or confocal microscopy. In order to do that, I would combine fluorescence with SHG readings of collagen in the 3D matrix, and so needed to use fluorescently labelled collagen. For that purpose, microspheres containing different types of collagen (in solution, lyophilised, DQ- and FITC-labelled collagen) were prepared, fixed with 4% PFA and then imaged with SHG. These microspheres did not contain PBMCs as matrix composition had to be kept as simple as possible while trying to confirm whether the SHG signal detected originates from collagen or not.

Microspheres with lyophilised collagen were made because this permitted a three-fold increase of collagen concentration in the 3D matrix (3 mg/ml instead of 1 mg/ml). However, in order to dissolve the lyophilized powder, HCl (pH = 2) was used as a solvent, which made the pH of the matrix drop to a very acidic value, not viable for the cells to grow in. This meant that such microspheres could not be used in subsequent experiments for cell culture. DQ-collagen is commonly used to track collagenase activity and its fluorescence is quenched until it is cleaved by a collagenase. All types of collagen were detected with SHG, except for (fluorescein isothiocyanate) FITC-collagen (*Figure 47e_1-e_2*). This probably indicates that the FITC conjugate does not allow for chemical, PFA-induced cross-linking of collagen and the formation of SHG-detectable fibres. The samples were also imaged with TPEF as collagen has been reported to autofluoresce at 390 nm,[95] but this was not detected in any of the samples (data not shown).

I was keen to verify that the SHG signal detected originates from collagen fibres, and so PFA-fixed microspheres were incubated with collagenase at 37°C overnight and imaged again with SHG. If the SHG signal detected originated from collagen fibres, the expected result would be that after collagenase treatment large collagen fibres would be turned to smaller undetectable fragments which would result in substantially fewer (if any) large collagen fibres detected in the microsphere matrix. However, this was not the case, as the signal remained unchanged before and after treatment of PFA-fixed microspheres with collagenase (*Figure 47*). Since collagenase was added externally to the 3D matrices, one potential explanation for that would be that it might have not been able to penetrate them. Another explanation could be that chemical fixation was preventing collagenase from degrading collagen by cross-linking the collagenase cleavage sites.

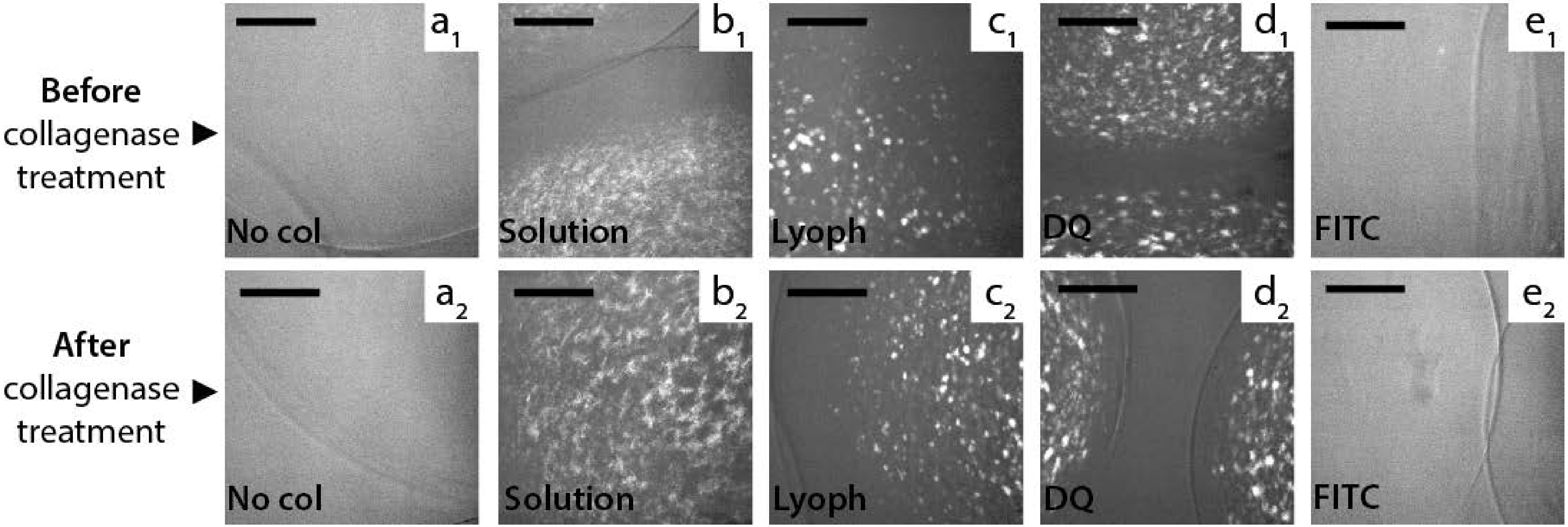

Figure 47. Collagenase treatment of PFA-fixed microspheres did not cause collagen degradation.

SHG images of microsphere matrices containing different types of human type I collagen, empty of any cellular component. Spheres before (**a_1-e_1**) and after (**a_2-e_2**) treatment with collagenase. Alginate 3D matrices with: (**a**) no collagen, (**b**) collagen solution, (**c**) lyophilised collagen, (**d**) DQ-collagen, and (**e**) FITC-collagen. FITC-conjugated collagen was not detected with SHG before or after treatment, which could indicate that the FITC conjugate does not allow for the collagen to be chemically cross-linked by PFA, unlike the rest of the collagen types. Scale bar = 50 µm.

Verification that the SHG signal derived from collagen in the microsphere matrix

Given that collagenase did not reduce the SHG signal of PFA-fixed samples, I performed a collagenase assay to verify that the SHG signal in my images originated from collagen by incubating microspheres with collagenase before fixation. The collagenase used was extracted from *Clostridium histolyticum* and was a mixture of molecules with molecular weights ranging from 68 to 125 kDa.

This time, three different concentrations of collagenase were added in the alginate-collagen gel before bioelectrospraying, then the mixture was passed through the bioelectrosprayer and formed microspheres. These microspheres were in turn incubated at 37°C for three days to enable collagen digestion by collagenase in the matrix. After three days, they were fixed with 4% PFA and imaged with SHG along with all necessary controls. The collagenase-containing samples showed no SHG signal at all three concentrations of the enzyme, which confirmed that fibrillar structures detected in alginate-collagen microspheres are indeed collagen fibres (*Figure 48*). No dose-response effect was observed between the three different concentrations of collagenase, which indicates that either a 3-day incubation was long enough for even the lowest concentration of collagenase to fully digest large collagen fibres or the collagenase concentrations used were too high for the amount of collagen present in the microspheres. Collagen fibres were detected with SHG (*Figure 48c_1-c_2*) which brings us to the conclusion that collagen does indeed 'thermally' cross-link in our microspheres at some point during the first 3 days of incubation at 37°C and PBMCs encounter them as they would in real human tissue.

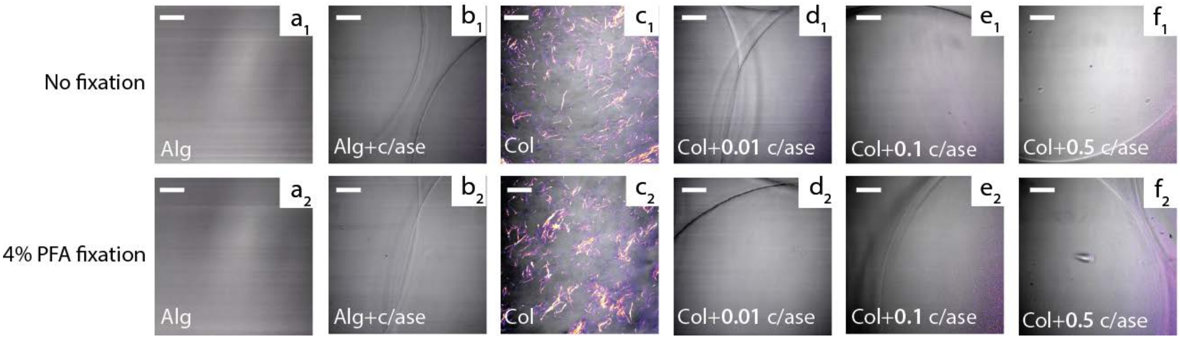

Figure 48. Verification of collagen presence in the alginate-collagen 3D matrices using collagenase.

Unfixed (**a_1-f_1**) and 4% PFA-fixed (**a_2-f_2**) microspheres. Types of matrices: (**a**) alginate, (**b**) alginate with 0.5 ml collagenase, (**c**) alginate-collagen, (**d**) alginate-collagen with 0.01 ml collagenase, (**e**) alginate-collagen with 0.1 ml collagenase, and (**f**) alginate-collagen with 0.5 ml collagenase. The alginate-collagen control sample (**c_1**, **c_2**) contained collagen fibres, whereas in all samples with collagenase, collagen was degraded and no SHG signal was detected. PFA-fixation after a 3-day incubation at 37°C did not affect collagen fibre formation in the same control sample. In the samples that did not contain collagen, SHG signal was also not detected, as expected. Scale bar = 25 μm.

Collagenase penetrates the microsphere matrix

On explanation of the non-collagenase effect seen in *Figure 47*, was whether collagenase penetrates the 3D matrix of the microspheres during incubation at 37°C. To answer that question, I incubated (at 37°C for three days) alginate-collagen microspheres with collagenase which was added externally to the microspheres after bioelectrospraying. After this time, samples were fixed with 4% PFA overnight and imaged with SHG.

The 3-day-long treatment with collagenase resulted in complete absence of SHG-detectable fibrillar collagen from the alginate-collagen microspheres (*Figure 49*). This indicates that *Clostridium histolyticum*-derived collagenase can penetrate the unfixed microspheres and either cleave human type I collagen in the 3D cell culture matrix to the point that it is undetectable by SHG or prevent collagen fibre formation in the first place. It also shows that molecules of a molecular weight above 65 kDa can penetrate our alginate microspheres.

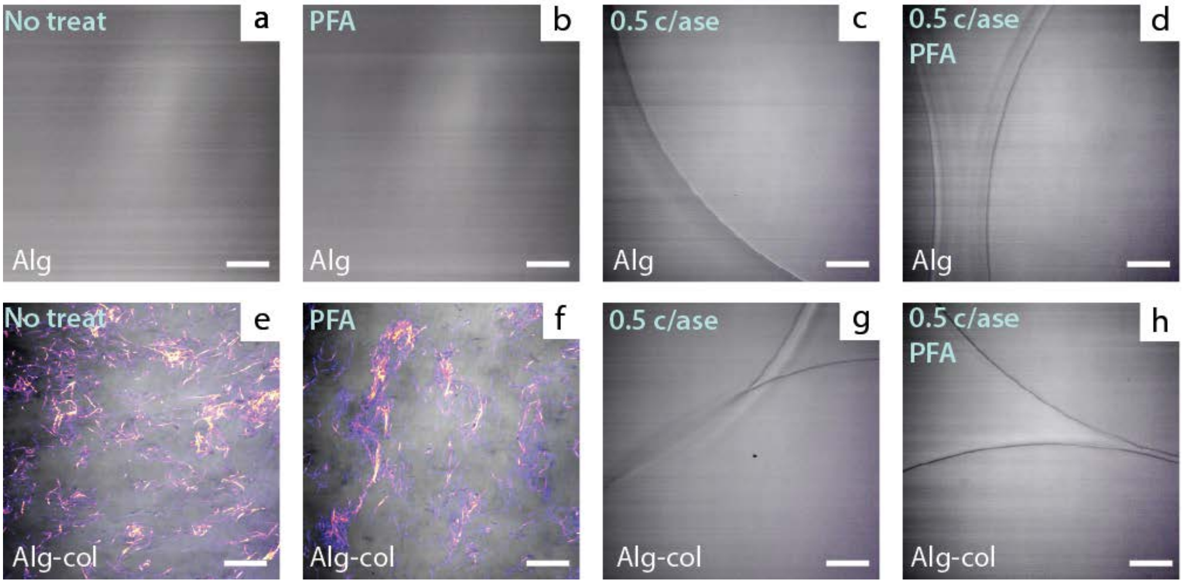

Figure 49. Collagenase penetrates the microsphere matrix.

Overlay of SHG (collagen) and TPEF (autofluorescence) images of alginate (**a**-**d**) and alginate-collagen (**e**-**h**) microspheres after a 3-day treatment with collagenase at 37°C and subsequent 4% PFA-fixation (for panels **b**, **d**, **f**, and **h**). Spheres with no treatment (**a**, **e**), PFA-fixed (**b**, **f**), with externally-added 0.5 ml collagenase (**c**, **g**), and PFA-fixed with externally-added 0.5 ml collagenase (**d**, **h**) were imaged at the same time. Fixation after the 3-day-long treatment did not seem to affect collagen cross-linking. The external addition of collagenase to the microspheres, on the other hand, resulted in complete disappearance of SHG-detectable collagen fibres in the microspheres. Therefore, collagenase can penetrate the sphere and cleave human type I collagen in the 3D matrix. Scale bar = 25 µm.

Imaging fluorescent PBMCs under SHG/TPEF laser

After successfully imaging collagen fibres in the 3D matrix, I then added an extra layer of complexity to the imaged sample by adding PBMCs to the microspheres. The purpose of this experiment was to utilise both SHG and TPEF channels to simultaneously obtain two readouts on the same field of view (FoV); one showing PBMCs (TPEF channel) and one showing collagen fibres (SHG). In order to achieve that, PBMCs were fluorescently stained so that they would be imaged in the TPEF channel while at the same time imaging collagen fibres with SHG in the same microsphere matrix.

Microspheres with PBMCs were stained with propidium iodide which stains the cells and fluoresces at 617 nm and then fixed with 4% PFA overnight before transferring to the room housing the fluorescent microscope. Fluorescent signal from PI-stained PBMCs was leaking into the SHG channel which resulted in collagen fibres not being detected in the microspheres, as the fluorescence was much more intense compared to the inherently weak SHG signal of collagen. Also, as soon as the laser shone on the fluorescently-labelled PBMCs, they started to burn (*Figure 50*) even when very low laser power was used. Burning cells appeared as black in the TPEF channel and saturated, bright white in the SHG channel.

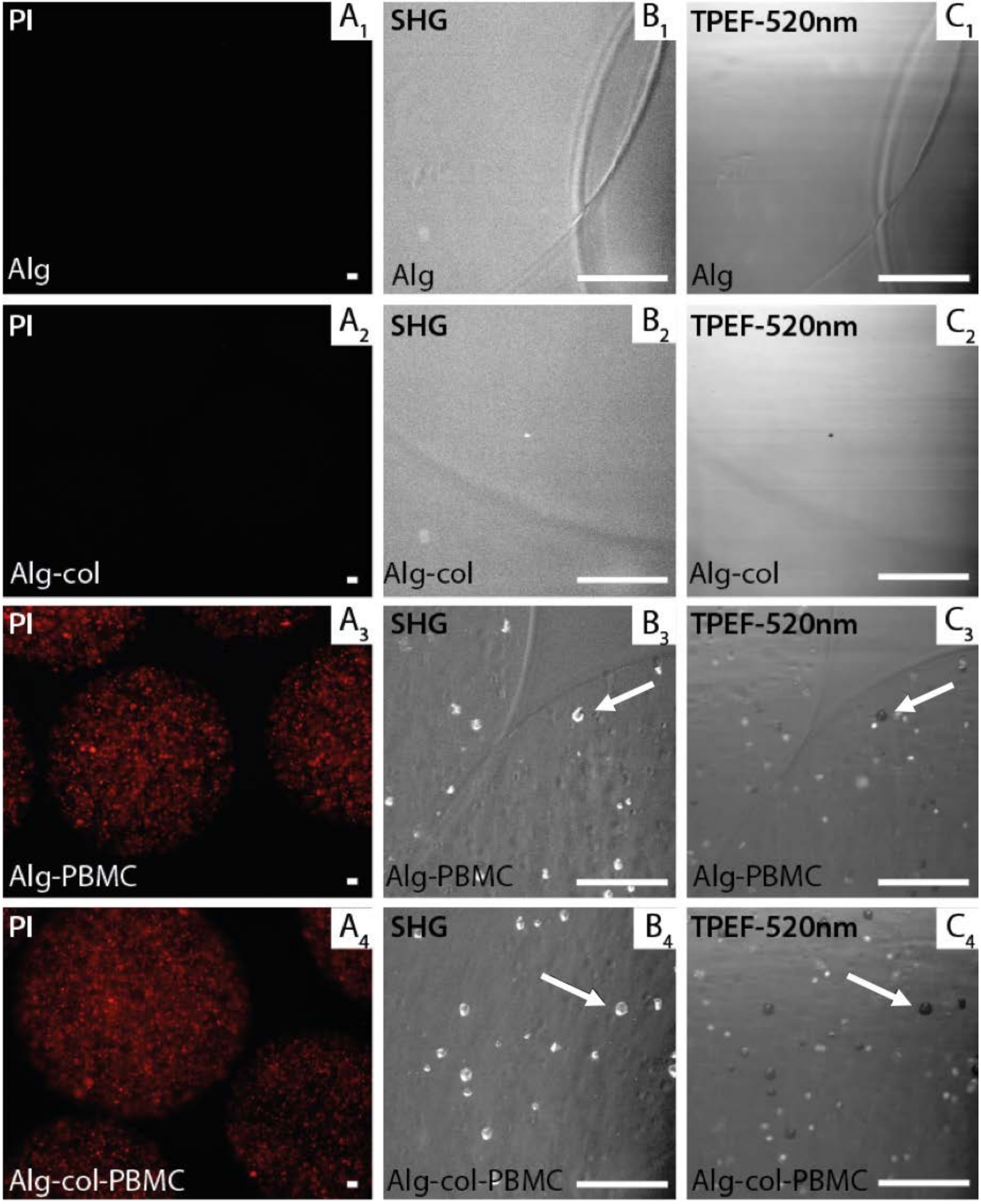

Figure 50. Fluorescent staining of PBMCs causes them to burn when illuminated by the pulsed laser.

(**A**$_1$-**C**$_1$) Alginate and (**A**$_2$-**C**$_2$) alginate-collagen microspheres without PBMCs, (**A**$_3$-**C**$_3$) alginate and (**A**$_4$-**C**$_4$) alginate-collagen microspheres with PBMCs. (**A**$_1$-**A**$_4$) Images from a standard fluorescence microscope, (**B**$_1$-**B**$_4$) SHG images, and (**C**$_1$-**C**$_4$) TPEF images of PI-stained PBMCs in microspheres. White arrows point to burning, fluorescently-labelled PBMCs, that appear white in the SHG channel and black in the TPEF channel. Scale bar = 50 µm.

4.2.2. Imaging PBMCs in microspheres with CARS

Having confirmed that SHG could image cross-linked collagen within microspheres, I was interested in investigating a better way to image the cellular content, especially as TPEF led to the fluorescently-labelled cells burning. CARS microscopy is a powerful technique for label-free imaging of biomolecules and has been applied by both our research group and others to image cellular lipids in cell cultures, tissues and organisms.[149,152,179] In our custom-built setup, CARS is coupled with a SHG modality which allows for simultaneous imaging of PBMCs and collagen in the same FoV in microspheres. CARS images of the alginate and alginate-collagen microspheres show it is possible to visualise the 3D matrix clearly in all three frequencies examined; a common frequency for lipids (2850 cm^{-1}), one for proteins (2960 cm^{-1}) and one for sugars (3030 cm^{-1}). These frequencies do not exclusively appear in lipids, proteins, or sugars, respectively. The 2850 cm^{-1} is assigned to the C-H stretching bond, which is a very common chemical bond (and therefore molecular vibration) found in lipids. The 2960 cm^{-1} peak corresponds to the asymmetric stretching vibration of CH_3, which is a vibration commonly found in proteins.[180] Finally, the 3030 cm^{-1} peak is assigned to the sp^3 CH_3 stretching vibration, which is frequently encountered in sugars.[181]

Selection of the best frequency for combined CARS/SHG imaging

As mentioned before, CARS imaging at the standard wavenumber for lipids (2850 cm^{-1}) and proteins (2960 cm^{-1}) showed that it is possible to clearly visualise PBMCs in the 3D matrix. Acquiring a SHG image of the same FoV can provide information about the distribution of collagen fibres in relation to PBMCs (as shown previously in *Figure 20*). The frequency selected for offering the best contrast for both cells and collagen was 2845-2850 cm^{-1}.

The SHG channel in *Figure 51* seems like it is detecting both collagen fibres and cell outlines, which could indicate cell autofluorescence leaking into the wrong channel. As described later in the thesis (*Collagen fibres*) I found that it detects both the free collagen fibres in the matrix, as well as the ones attached to the cell membrane of some PBMCs, which makes it look like it is detecting some cells as well. The reason this happens is still unknown, but it occurs in PBMCs of both infected and uninfected samples.

Microspheres with PBMCs infected with live Mycobacterium tuberculosis *(lab strain: H37Rv)*

Having performed the initial optimisation steps, CARS/SHG imaging of microspheres was performed at days 1, 7 and 14 after infection with the commonly-used *Mtb* laboratory strain H37Rv (*Figure 53*). Cell aggregation was observed at day 7 and day 14 in the infected samples (*Figure 52*). Some cell aggregation was also observed in the uninfected, collagen-containing, control samples. From day 7 onwards, elongated macrophages started to appear in the periphery of the collagen-containing microsphere (*Figure 53*), consistent with previous observations by our group using different imaging modalities.

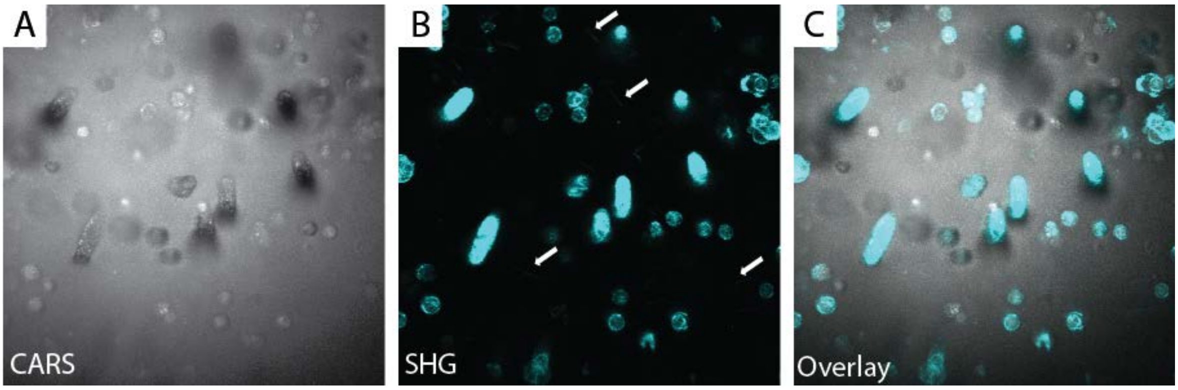

Figure 51. CARS and SHG imaging of microspheres containing PBMCs.
(**A**) CARS image (greyscale) taken at 2850 cm^{-1} showing day 7, *Mtb*-infected PBMCs in an alginate-collagen matrix after 4% PFA fixation. (**B**) SHG image showing collagen fibres (white arrows pointing to very thin lines pseudo-coloured as **cyan**) and PBMC outlines (**cyan**). Some PBMC outlines light up in the SHG channel as there is accumulation of collagen fibres around some PBMCs. (**C**) Overlay of CARS and SHG images show collagen (**cyan**) accumulating around certain PBMCs.

Due to low SNR, quantitative information about cell aggregates in 3D could not be obtained automatically by available Fiji plugins. Therefore, cell aggregate size and number was manually counted in ‘Day 1’ and ‘Day 7’ samples where 3-5 microspheres from each sample were imaged at a depth of 200 µm. This information could not be obtained for ‘Day 14’ samples as only one microsphere per sample was imaged at that time-point. The minimum aggregate size for counting was selected at 4 cells.

It seems that at day 7 (*Figure 52*), the presence of collagen in the matrix had a positive effect on the number of large aggregates, however *Mtb* infection did not seem to increase this aggregation further. The fact that collagen was shown to have a more dominant effect than *Mtb* infection on PBMC aggregation in the microspheres was surprising, as it has been previously shown by Tezera *et al*[97] using light microscopy that there is increased aggregation in infected microspheres. Since neither of these effects were statistically significant in my study, I can only conclude that neither the presence of collagen nor *Mtb* infection significantly affected the total number of aggregates, when 3-5 microspheres were imaged from each sample. In order to acquire statistically significant information, I would first need to eliminate any donor-to-donor variation by repeating this experiment for at least 3 different PBMC donors (currently only a single donor's cells were imaged) and by having a higher throughput of imaged microspheres from each sample.

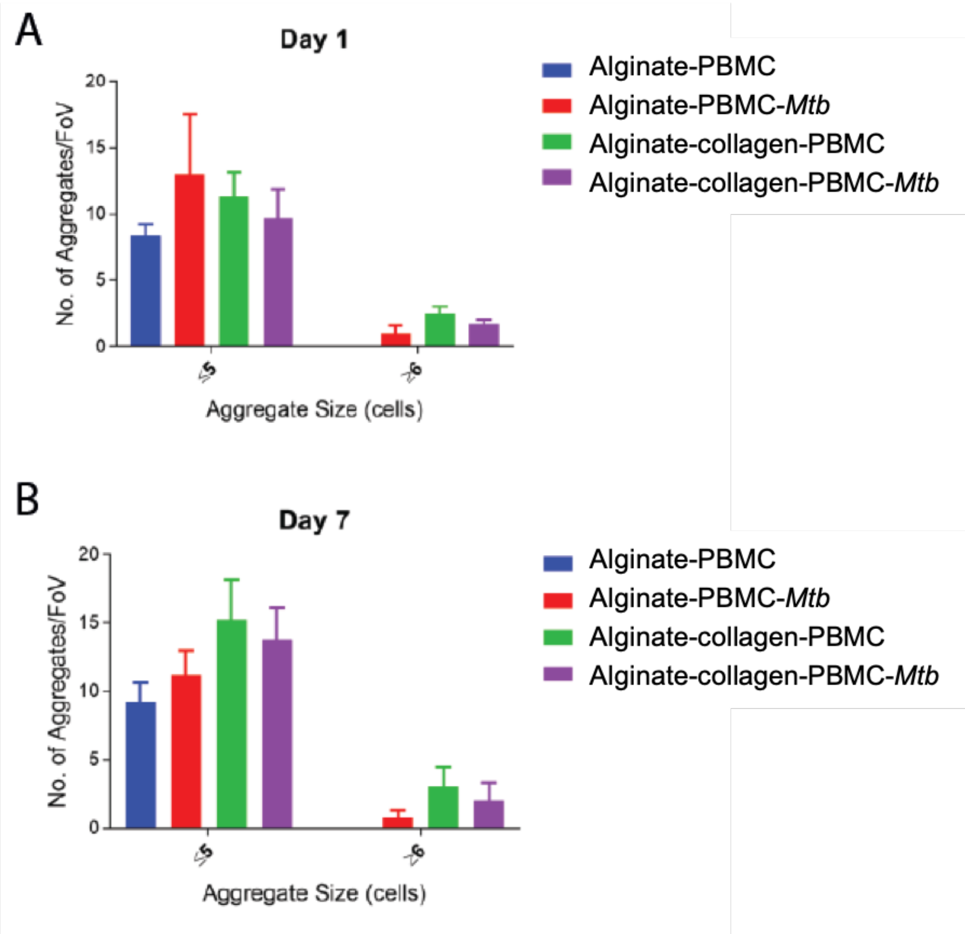

Figure 52. Presence of collagen and *Mtb*-infection did not significantly affect PBMC aggregation in the microsphere (size and number of aggregates measured in CARS images) At days 1 (**A**) and 7 (**B**) of infection with *Mtb,* PBMC aggregates were counted in the central FoV of at least three spheres of each kind (with or without collagen and with or without *Mtb*). Small aggregates were defined as equal to or less than 5-cells-big (plotted **left**) and large aggregates (plotted **right**) were defined as equal to or more than 6-cells-big. Neither collagen nor *Mtb*-infection in the 3D matrix significantly increased PBMC aggregation in the microspheres (at day 1 or 7) when quantitated by CARS.

Collagen was found to accumulate around some PBMCs in the collagen-containing microspheres, as well as to form independent fibres in the matrix. Each panel in *Figure 53* represents a z-stack of SHG images projected as a 2D representation using 'Z-project' (maximum intensity) in Fiji. For links to the videos showing a 360° rotation around the Y-axis of the 3D projections of z-stacks shown in *Figure 53*, please see *List of Accompanying Materials.*

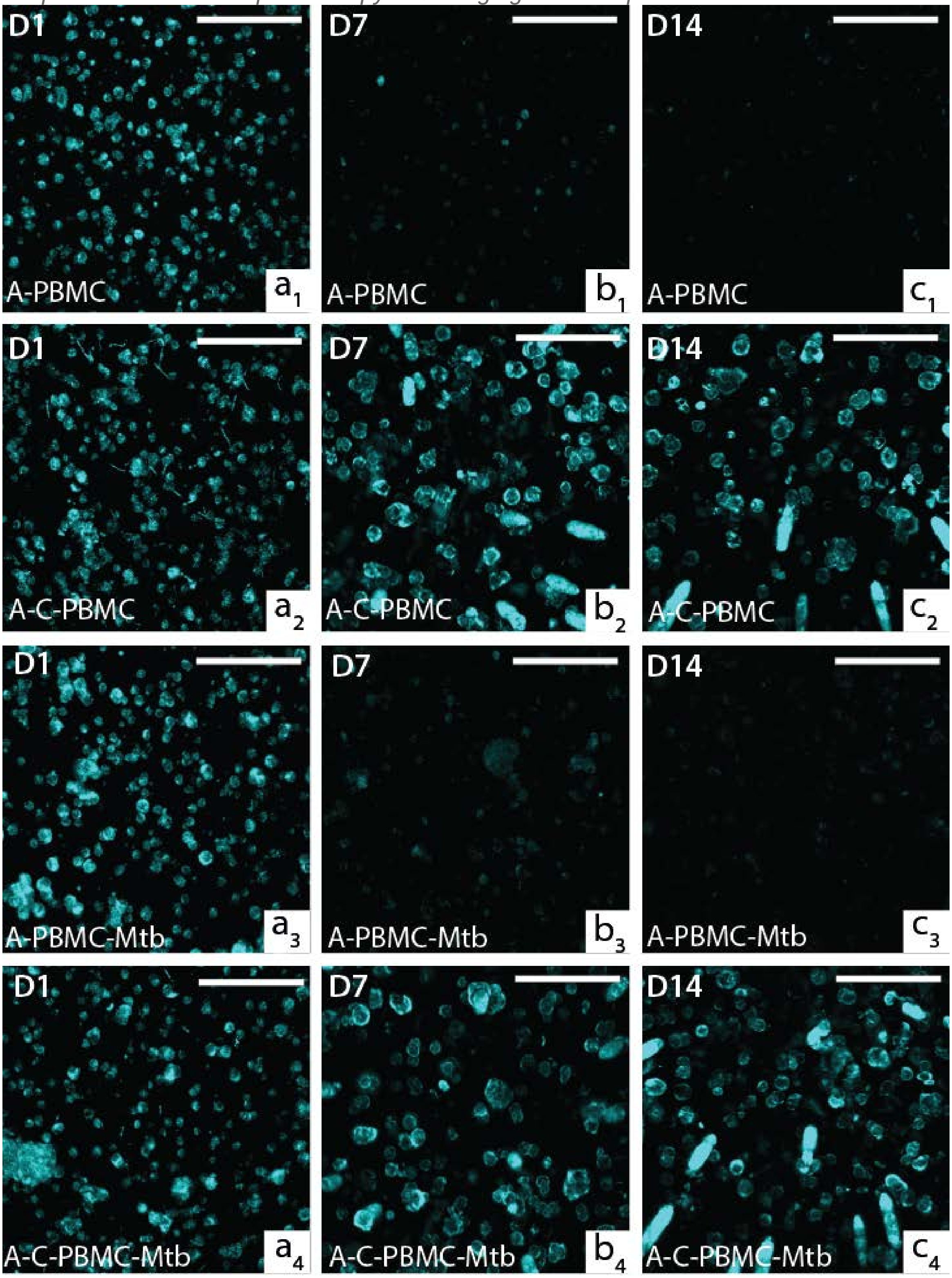

Figure 53. SHG z-stacks of microspheres at days 1, 7 and 14 of infection.

(**a_1-a_4**) Day 1, (**b_1-b_4**) day 7, (**c_1-c_4**) and day 14 of infection. (**a_1-c_1**) Alginate matrix, no infection, (**a_2-c_2**) alginate-collagen matrix, no infection, (**a_3-c_3**) alginate matrix, *Mtb*-infection, (**a_4-c_4**) and alginate-collagen matrix, *Mtb*-infection. Cell (**cyan** LUT) aggregation was observed at day 7 and 14 when looking through the z-stack slice-by-slice, as well as the emergence of elongated macrophages in the periphery of the microsphere in collagen-containing samples. Cells appearing larger in day 7 and 14 samples is due to the accumulation of more collagen fibres around them as the days pass. Each of these images is a maximum intensity z-projection in Fiji. Pseudo-colour (**cyan** LUT) was added digitally in Fiji. Scale bar = 50 µm.

4.2.3. Discussion

I used Raman spectroscopy to characterise the raw materials of our 3D cell culture matrix, which were alginate and human type I collagen. First, I successfully distinguished between two different types of alginate (pure and mixture) and then between the powder form and the microsphere form of each one. I also characterised the Raman spectrum of human type I collagen and distinguished between the gel and microsphere forms of alginate-collagen mix. Collagen could not be detected in the microspheres, most likely due to its very low concentration. Bonnier *et al.,* who used a collagen gel as a 3D matrix for their cells, reported that the collagen gel did not contribute to the Raman spectrum of the 3D cell culture, which is in line with our findings. In order to make their collagen gel, a 5 mg/ml collagen solution was used, even higher than the 3 mg/ml collagen solution we used for our alginate-based 3D cell culture matrix. This indicated that the collagen concentration that is sufficient to sustain cell viability is too low for a conventional Raman spectrometer to pick up.[80]

Alginate and type I human collagen have also been studied by other groups with Raman spectroscopy, either as raw materials or as parts of a 3D cell culture. The area of the Raman spectrum of alginate that is below 1300 cm^{-1} contains mostly vibrations of the polymer backbone, and the area starting from 1300 cm^{-1} and above contains the stretching vibrations of the carboxylate functional groups.[92] For the Raman peak assignment of sodium alginate from other groups, see *Appendix I*.[92,93] My findings were overall consistent with the ones from other groups, as I identified the same main alginate peaks at either the same or slightly different wavenumbers.

In Raman spectroscopy studies of type I collagen by other groups,[175,176] all of the peaks I identified were reported, as well as some additional ones. I could only detect a Raman signature from collagen when I measured dried collagen solution. The reason I detected fewer peaks is most likely due to the very low concentration of our collagen solution, which causes it to give a weak signal. Another reason for this could be that collagen in the solution was in the form of small tropocollagen molecules and not fibrils, which give a much stronger Raman signal and quite possibly more peaks in the spectrum. The collagen Raman spectrum was also affected by the Raman signal of the quartz cover slip that was used as a substrate for conducting the measurements. In a study by Dong *et al*, the Raman spectra of type I collagen at different temperatures were collected, with the temperature ranging from -150 °C to 200 °C.[175] In a different study by Votteler *et al*, the type I collagen Raman spectrum was identified and some of its characteristic peaks were reported at different wavenumbers. In the latter study, collagen was lyophilized,[176] contrary to the study by Dong *et al*, where it was in a solution.[175] In a study by Frushour and Koenig, two amide III peaks were reported at 1248 and 1272 cm^{-1}. Their hypothesis was that the existence of two distinct amide III peaks in the Raman spectrum of collagen is due to the biphasic nature of the tropocollagen molecule, referring to the proline-rich (non polar) and the proline-poor (polar) regions of the collagen chain.[182] Therefore, my findings on dried collagen were consistent with those reported in the literature, but the methodology does not seem well suited for quantitation of collagen turnover in the microspheres.

Since collagen could not be detected by Raman spectroscopy in its current concentration in the 3D matrix, I decided to pursue other methods of investigating collagen degradation by exploring other types of label-free techniques, which give stronger signals for collagen, (SHG) and allow for simultaneous imaging of cells in the 3D cell culture, namely CARS and TPEF.

SHG is commonly used alone or in conjunction with TPEF to study the extracellular matrix, because of its ability to create high-resolution 3D images of tissues.[116,124] In fact, Japanese researchers utilised quantitative SHG combined with TPEF *ex vivo* in a mouse model for osteoarthritis, and successfully measured the degeneration of components of articular cartilage. Their final aim is to establish this technology as a diagnostic test for this disease.[137]

CARS has been used to study the behaviour and kinetics of lipids, since they are particularly CARS-active. Le *et al.* showed that lipids accumulate in M109 lung cancer cells from BALB/c mice, due to excess free fatty acids. They also found a positive correlation between intracellular lipid content and cancer metastasis.[129] Furthermore, CARS is being used for the *in vivo* monitoring of the status of myelin sheath nerves in demyelinating diseases, like multiple sclerosis.[125,130-133] Since myelin is about 70% lipidic in nature,[131] it is a prime target for CARS. In fact, Huff *et al.* utilized CARS for the *in vivo* imaging of the myelin sheath in the sciatic nerve,[130] while Wang *et al.* combined CARS and TPEF to image axon myelin in pigs and characterise the molecular orientation of myelin lipids.[125]

SHG is best at detecting cross-linked collagen, and collagen cross-links when fixed by formalin[177] or when incubated at 25-37°C.[178] I confirmed using SHG that human type I collagen in the microspheres forms fibres if it is either chemically cross-linked by PFA fixation, or thermally cross-linked during the first three days of incubation at 37°C. Different types of both fluorescent and unlabelled collagen were imaged in the 3D matrix to determine whether fluorescent collagen can be used in the making of microspheres, in order to obtain both fluorescence and SHG readings on the same FoV. The fibrillar form of collagen was best depicted in the microspheres containing unlabelled collagen solution and this is the one that was then used for all subsequent experiments. FITC-conjugated collagen did not show any fibres on SHG imaging even after PFA-fixation, most likely due to the FITC conjugate blocking fibre formation. After characterising collagen-containing microsphere matrices with SHG, I showed the effect of collagen on macrophage shape and motility using CARS.

Combined CARS and SHG imaging has been proposed as a platform for monitoring stem cell differentiation by imaging the cell morphology (CARS) and simultaneously the production of collagen with a very low detection limit (SHG).[82] Imaging of our microspheres with CARS and SHG showed that visualisation of both PBMCs and collagen fibres is possible. After imaging at different CARS frequencies, the best contrast for both cells and collagen fibres was found to be at 2845 cm^{-1} and 2850 cm^{-1}, two general wavenumbers for CARS imaging of lipids. Imaging at this frequency allowed for detailed visualisation of the cell outline due to the lipids present in the cell membrane. These readouts were then used to characterise cell aggregation in microspheres containing *Mtb*-infected PBMCs. Cell aggregation was observed after one and two weeks of culture at 37°C in the infected samples, but some aggregation was also observed in the collagen-containing, uninfected control. The emergence of elongated macrophages around the periphery of the collagen-containing microspheres was also shown with CARS/SHG, consistent with previous observations from our group. At least 3 microspheres of each sample were imaged for this experiment but the effect of infection with *Mtb* or presence of collagen in the 3D matrix on cell aggregation remained unclear as our study suffered from a small sample size and the absence of experimental triplicates. Analysis of a greater number of samples would be required to give sufficient statistical power to determine whether aggregation measured by this method shows a significant increase.

Therefore, I investigated three methods to chemically characterise and image microspheres using Raman spectroscopy and non-linear optics; CARS and SHG. Overall, Raman spectroscopy of microspheres was disappointing as although I could acquire a spectrum from collagen in solid form, the collagen concentration in the microspheres was insufficient to be detected by a commercial Raman spectrometer. Both CARS and SHG generated clear images of collagen and cellular lipid, but the next major challenge will be to develop methods to quantitate aggregation, lipid content and matrix turnover in an automated, unbiased manner. These issues relate to numerous emerging imaging platforms,[183] where digital analysis of images permits quantitation. For example, while our group has previously demonstrated increased cell aggregation using light microscopy to count aggregates in a large number of spheres[97] I did not show a statistically significant difference due to the low throughput of this approach and the consequent low number of spheres that I could analyse. My next step was to proceed to more traditional and well established imaging techniques, such as transmission and scanning electron microscopy, to investigate microsphere structure and cellular behaviour.

Chapter 5

-

Imaging the microsphere model

Chapter 5. Imaging the microsphere model

Using label-free imaging techniques to chemically characterise and image the microsphere model undisturbed by staining and general sample preparation steps identified a number of unforeseen challenges and presented a number of limitations. Therefore, I then proceeded to image the microsphere model and its internal structures with more established or better developed techniques, such as scanning and transmission electron microscopy, confocal microscopy and micro-CT. My overall goal remained to compare emerging and established imaging techniques to determine what kind of information they were able to generate.

5.1. Collagen fibres

The first feature of interest for the purposes of this thesis, and in the general research interests of our group, was collagen. As mentioned in the *Materials & Methods* chapter, human type I collagen solution is used as a component of the 3D matrix of the microspheres. Upon incubation at 37°C, the short collagen molecules cross-link and form larger collagen fibres that run through the entire 3D matrix providing mechanical stability for the cells and a fibrillar network for them to use for migrating around the microsphere. Scanning Electron Microscopy is an excellent technique for visualising the surface of 3D objects and generating a comprehensive image of the surface and texture of a specimen. Sample preparation is minimal compared to that of other electron microscopy techniques (e.g. TEM, SBF-SEM) and therefore our microspheres could be imaged on the day they were fixed. For that purpose, I collected microspheres infected with H37Rv, processed them for SEM and then cut several of them in half using a scalpel blade. SEM images of an intact microsphere as well as one that was cut in half can be seen in *Figure 54*.

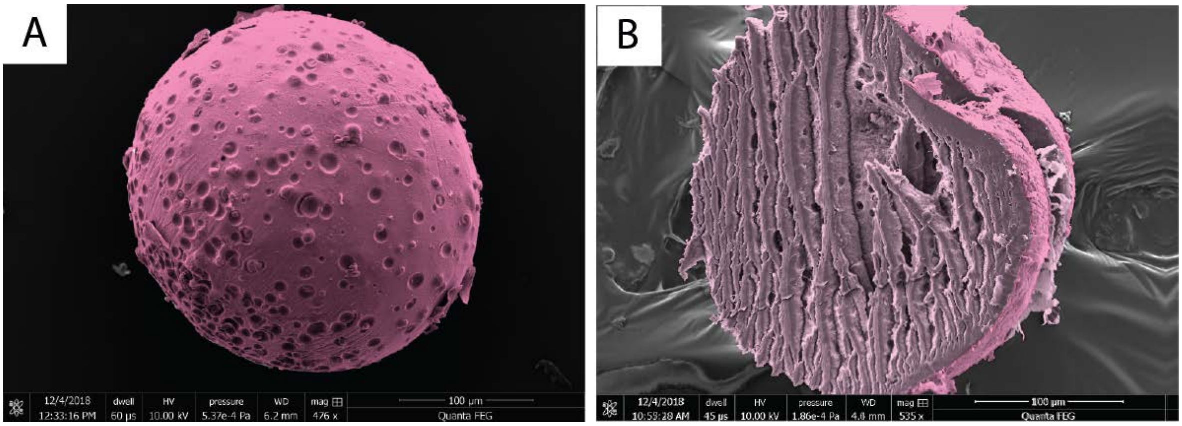

Figure 54. SEM view of a microsphere after critical-point drying.

External (**A**) and internal (**B**) view, after the microsphere was cut in half using the blade of a scalpel. Small holes in the matrix indicate locations where cells are thought to have been. During the cutting process most PBMCs are believed to have fallen off but some can still be seen in tunnel-like formations in the matrix.

One of my aims was to use SEM imaging to investigate the localisation of collagen fibres in the microsphere matrix as well as whether there was binding between collagen and the alginate network. In order to achieve that level of detail and image individual fibres, I increased the magnification of the SEM, but was constrained by the resulting resolution and therefore could not reach a conclusion on how collagen fibres are aligned in the matrix. However, I was able to sufficiently resolve parts of collagen fibres that were extending towards the outer surface of the microsphere (*Figure 55*).

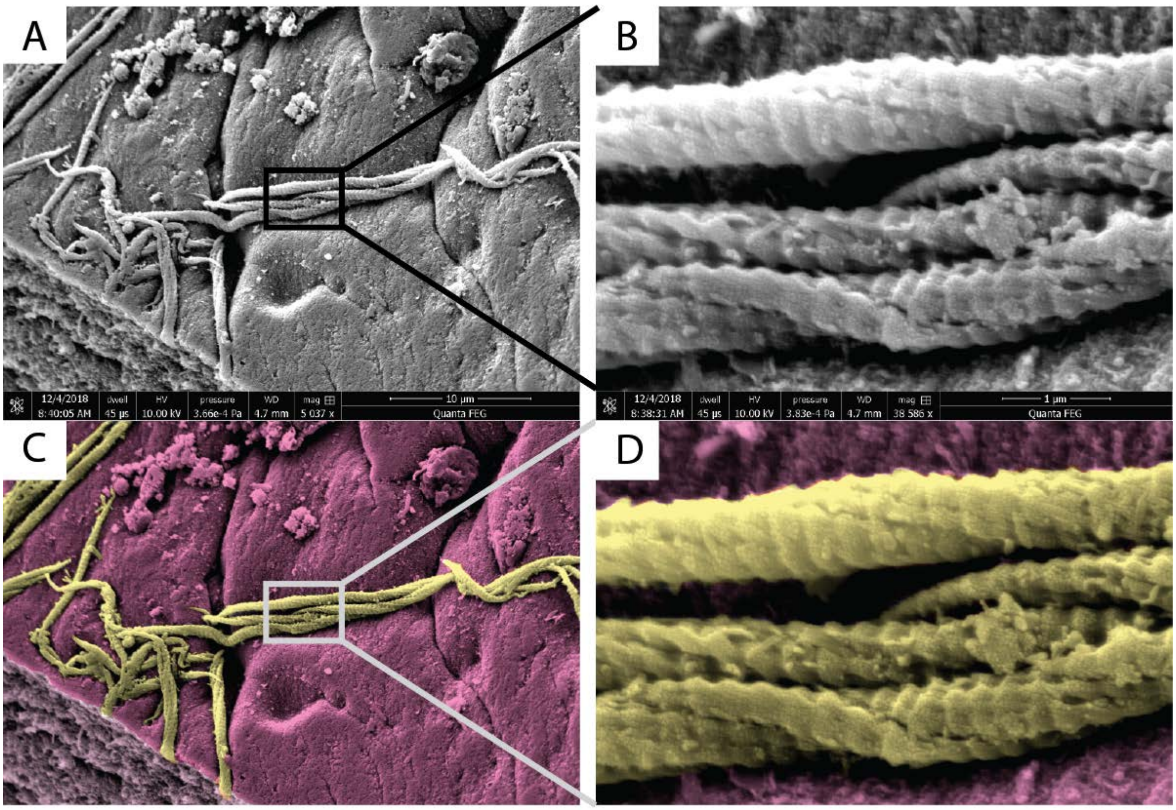

Figure 55. Collagen fibres on the outer surface of a microsphere imaged by SEM. Collagen fibres (yellow) were imaged at (**A**, **C**) a low (approximately 5,000x) and (**B**, **D**) a high (approximately 38,500x) magnification. The typical cord-like structure of fibrillar collagen is observed. Both (A, B) original greyscale and (C, D) pseudo-coloured (to enhance contrast between collagen fibre and the surrounding alginate) versions of these images are shown here.

It is known that collagen degradation takes place around infected PBMCs[184] and to demonstrate whether that happens within our microsphere model, we imaged day 7 infected cells in microspheres using confocal microscopy. We stained the cells with PI which stains nucleic acids and used DQ-collagen which fluoresces green when cleaved. The result was yellow light which resulted from the overlap of green (collagen degradation) and red (cells) around an aggregate of *Mtb*-infected PBMCs (*Figure 56*) In order to determine whether this collagen degradation increases with time, we would need to perform live microscopy which we did not do as it was deemed to be outside the scope of this project. Live microscopy of microspheres also presents a number of challenges related to maintaining focus depth stable and preventing microspheres from moving and rotating.

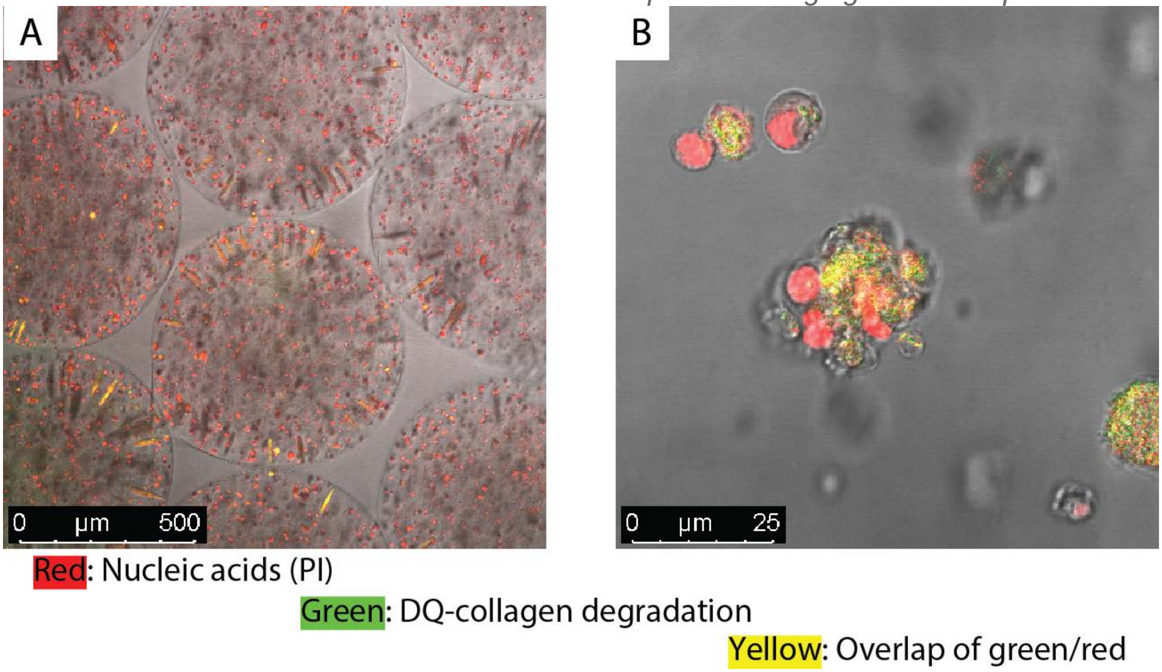

Figure 56. Confocal imaging of microspheres containing *Mtb*-infected PBMCs. (**A**) Confocal image at 10x magnification of PI-stained, day 7, *Mtb*-infected PBMCs in microspheres with DQ-collagen in the matrix. (**B**) Confocal image at 20x magnification where red staining shows PBMC nuclei and yellow indicates the overlap of green (i.e. collagen degradation) and red (i.e. PBMCs).

Next, having shown collagen fibres on the microsphere surface by SEM and collagen degradation by confocal microscopy, I moved on to TEM imaging, which allows for much higher resolution. TEM is ideal for imaging of finer cellular structures as well as the relationship of cells with collagen fibres. When microspheres were imaged with TEM, a collagen capsule-like formation (*Figure 57*) was observed around certain PBMCs either apoptotic, necrotic or healthy-looking in both *Mtb*-infected and uninfected samples. Most PBMCs with such a collagen capsule around them appeared dead or to be undergoing cell death. According to the Nomenclature Committee on Cell Death (2009) a cell can be considered ‘dead’ when one of certain molecular and/or morphological events takes place. The one relevant to the imaging performed in this thesis is that ‘*the cell, including its nucleus, has undergone complete fragmentation into discrete bodies (which are frequently referred to as ‘apoptotic bodies’)*’ in order for it to be considered ‘dead’.[185]

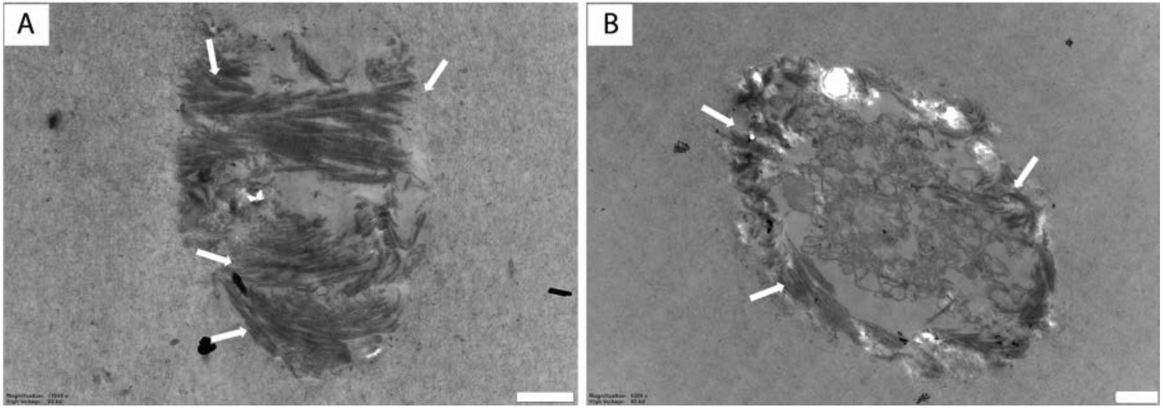

Figure 57. TEM images of individual PBMCs with collagen fibres tightly wrapped around them. Both cells appear to be dead as there is no visible subcellular structure. White arrows are pointing to collagen fibres tightly wrapped around the cell. This phenomenon was observed in PBMCs from both *Mtb*-infected as well as uninfected samples and its cause or consequences are unknown. Scale bar (white) = 1 µm.

SEM imaging revealed a capsule-like formation around some PBMCs of unknown origin (*Figure 58*). The resolution of the SEM was not sufficient for us to reach a conclusion as to whether this capsule is made of collagen fibres as suggested by TEM imaging of the microspheres, but correlation between the two imaging modalities would suggest that this was the case.

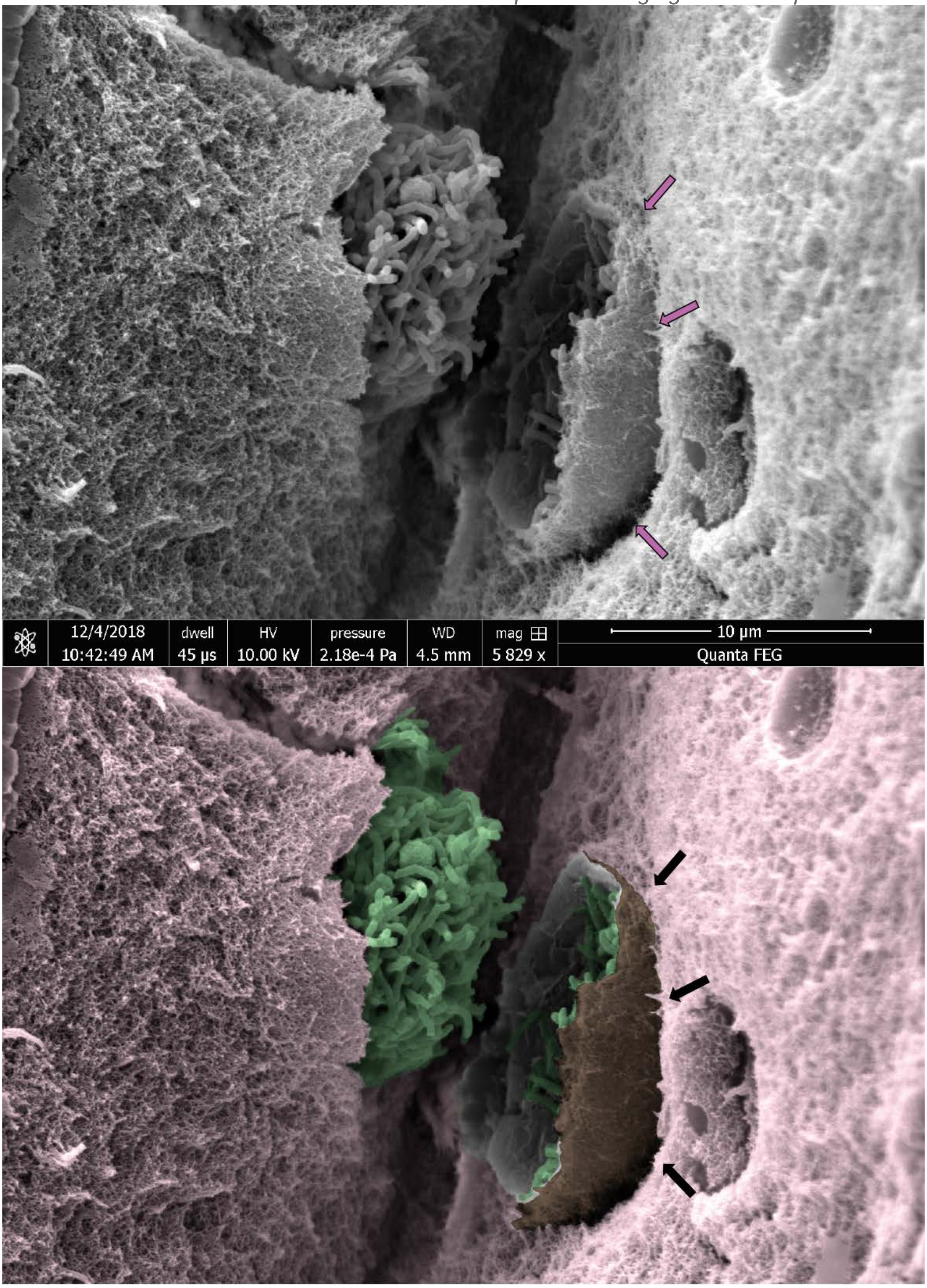

Figure 58. SEM picture of a day 7 *Mtb*-infected PBMC riddled with bacteria (**green**) and a capsule- or shell-like formation (arrows) around it (**brown**).

5.2. *Mtb* infection of PBMCs in microspheres

Using TEM I imaged PBMCs in microspheres that were either uninfected, or infected with one of the two *Mtb* strains available to me; the commonly-used laboratory strain, H37Rv (*Figure 59*), which we hypothesise might now be attenuated after being grown *in vitro* for decades; and a clinical isolate, 0414B, which is derived directly from a patient with active TB and is likely to be more virulent. However, this was technically challenging as the resin always appeared to be torn around *Mtb* bacilli.

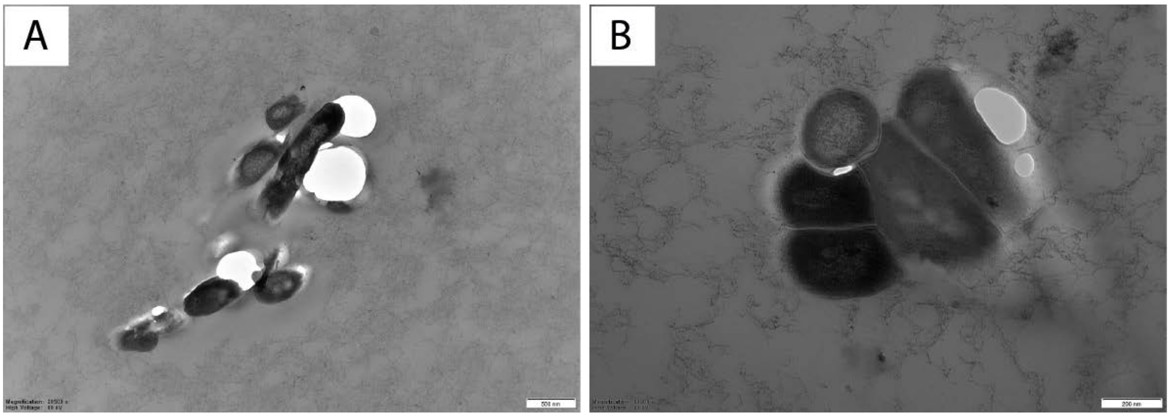

Figure 59. TEM pictures of UV-killed *Mtb* bacilli of the strain H37Rv embedded in alginate as found in the microspheres without the presence of PBMCs.

Tears in the resin were always observed around *Mtb* bacteria indicating that the bacteria cell wall might be repelling the resin around it. Bacteria had to be UV-killed as they still retain all their structure but cannot cause infection and so we could prepare the samples in a BSLII laboratory without the need for the specialist BSLIII laboratory needed when working with live *Mtb*. Bacteria were UV-killed by Dr. Magdalena Bielecka.

When imaging PBMCs in microspheres with TEM, I found that the same tears in the resin were observed around phagocytosed *Mtb* bacteria as well (*Figure 60*) both of the lab strain H37Rv as well as the clinical strain, 0414B. Less often I would find tears like these around lipid bodies in the cell cytoplasm which might suggest there is a property in lipids that repels the resin which would apply to both lipid bodies as well as the outer surface (e.g. mycolic acid layer) of *Mtb* bacilli.

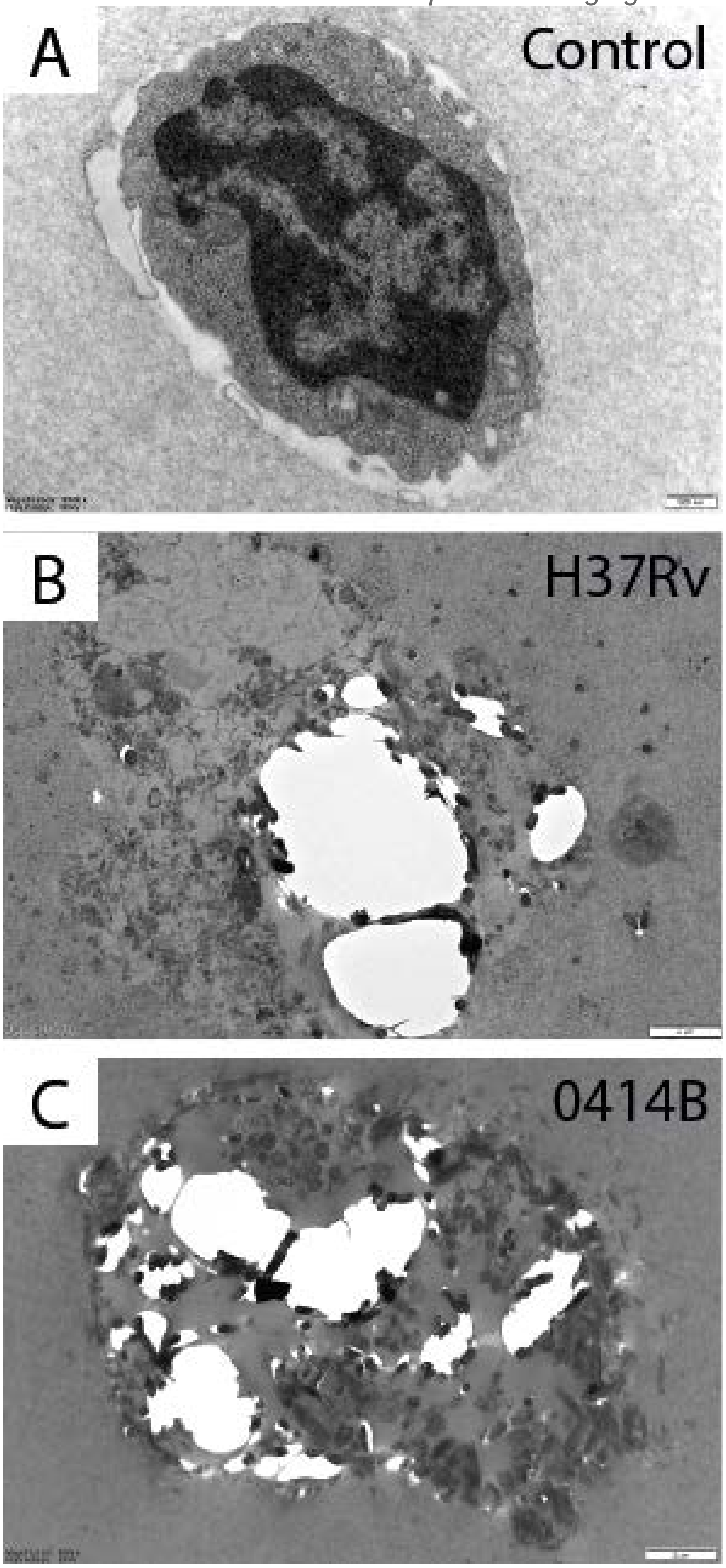

Figure 60. TEM imaging of a healthy cell versus two *Mtb*-infected ones (H37Rv and 0414B). (**A**) Uninfected control cell, (**B**) H37Rv-infected cell, and (**C**) 0414B-infected cell, all within microspheres. A typical TEM picture of an infected cell features these characteristic tears (saturated white areas) within the cell, around bacteria. Both infected cells appear dead as there is no visible subcellular structure anymore. Only a few cells in each microsphere section from an infected sample would appear so damaged and riddled with bacteria. Most of them appeared healthy or necrotic/apoptotic but without any bacteria in their cytoplasm in the plane represented in the section.

There is published data that suggests that sometimes phagocytosed *Mtb* bacilli escape the phagosome and reside in the cytoplasm.[18,19,186-189] I tried to investigate this hypothesis by TEM imaging of phagocytosed bacteria with the aim of counting the number of membranes around them (e.g. cell membrane, mycolic acid cell wall) and seeing if there was an extra membrane which would be host-derived (phagosomal) (*Figure 61*). However, the aforementioned problem with the resin rendered the resin blocks softer than normal and therefore did not allow for the sections to be cut thinly enough (i.e. thickness of 10 μm) for the microscope to be able to resolve such detail (e.g. number of membranes).

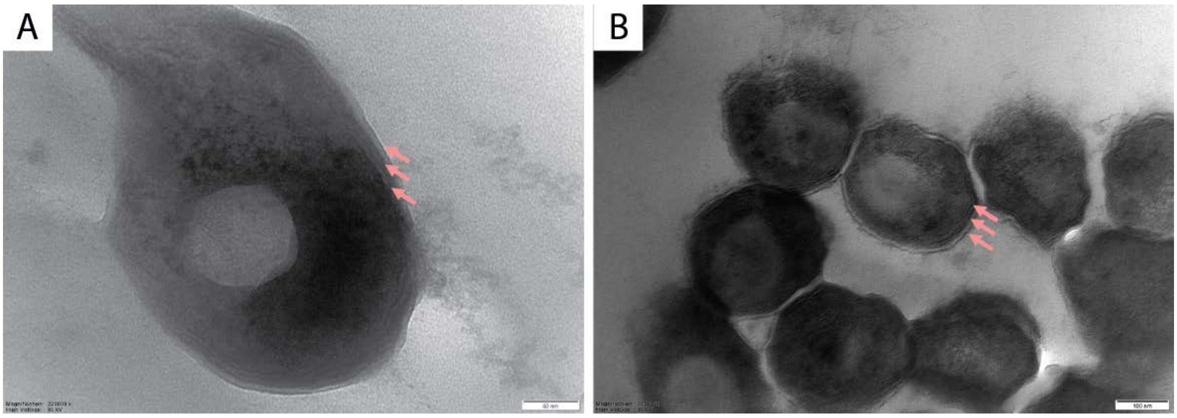

Figure 61. TEM pictures of phagocytosed *Mtb* bacilli in PBMCs in microspheres. (**A**) TEM close-up of a single *Mtb* bacillus at 220,000x magnification. (**B**) Lower power TEM picture (105,000x magnification) showing *Mtb* bacilli with what appears to be a single (possibly host-derived) membrane around multiple of them (**pink** arrows). Due to the thickness of the section, it is difficult to determine whether the (seemingly) third membrane around the bacilli is actually intact and host-derived.

5.3. Cellular aggregation in TB

5.3.1. TEM imaging of a single PBMC aggregate

It is known that *Mtb*-infected cells cause cellular aggregation around them to form granulomas.[190] One such aggregate can be seen in *Figure 62*, where at least five cells have aggregated together and are undergoing cell death. Cellular aggregates are not a common occurrence in *Mtb*-infected microspheres and were especially hard to find when randomly taking an ultra-thin section off a resin block. There are likely to be merely 2 or 3 aggregates in a single microsphere (diameter of ~1mm), therefore the chances of sectioning through the middle of one are low. I aspired to image phagocytosed bacteria within such aggregates but after imaging hundreds of cells, I only came across one aggregate which indicates how hard it is to randomly come across one in an ultrathin section. In that one aggregate I did not detect any bacteria, but I merely imaged a single plane of ~0.12 μm thickness through the aggregate. Consequently, a correlative imaging approach seems to be needed in order to image the entirety of a cellular aggregate in such great detail.

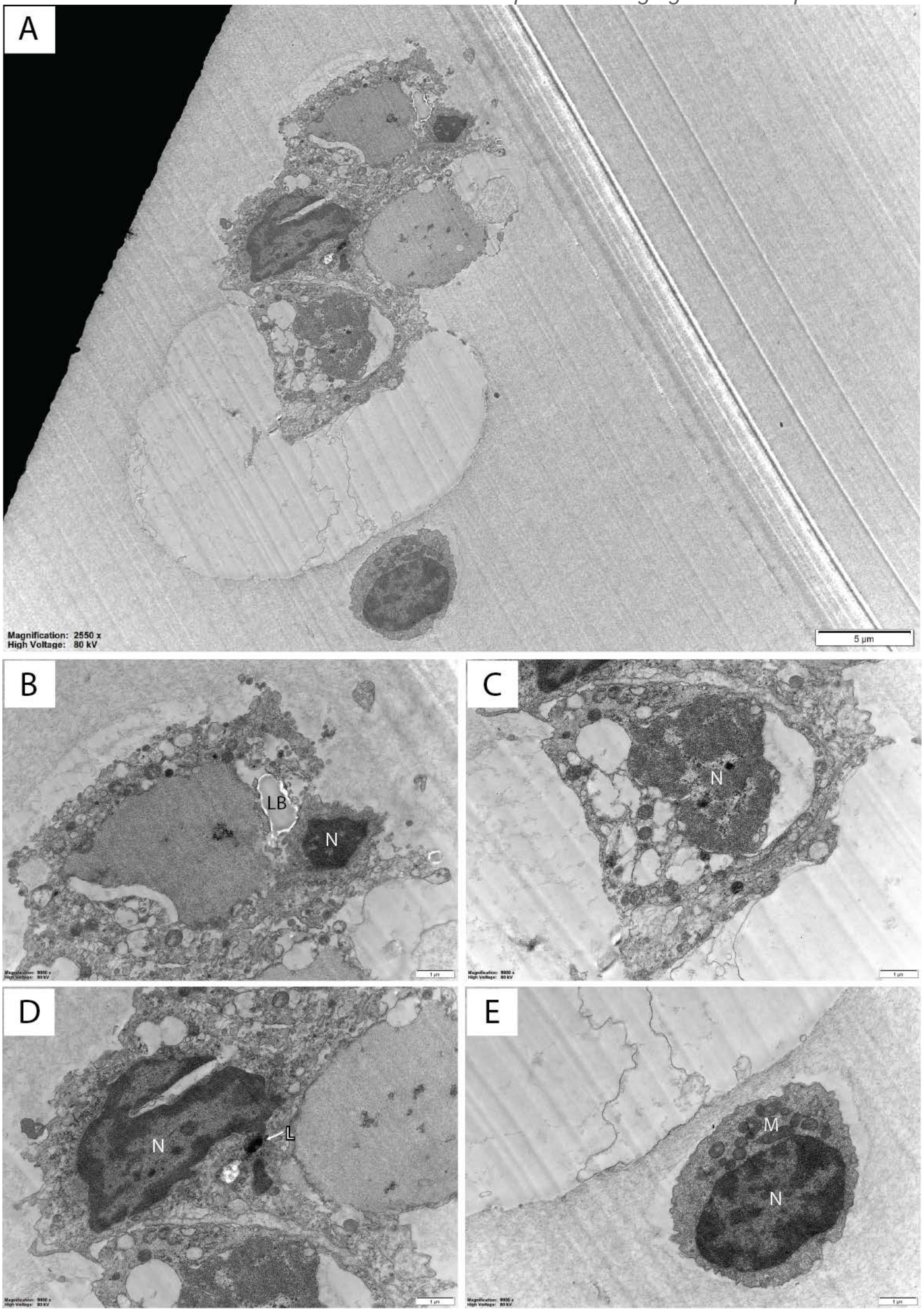

Figure 62. TEM images of an aggregate and the individual PBMCs of which it consists.

A PBMC aggregate (**A**) and close-ups of its constituent cells (**B**-**E**) in a microsphere incorporating infected PBMCs at day 7 after infection with the clinical *Mtb* strain 0414B. (**N**: Nucleus, **M**: Mitochondria, **L**: Lysosome, **LB**: Lipid body)

5.3.2. Micro-CT for localisation of cellular aggregates in *Mtb*-infected microspheres

In order to non-invasively locate cellular aggregates in the microsphere model of *Mtb*-infected PBMCs, I used micro-CT to scan a resin block of H37Rv-infected microspheres at day 14 after infection, originally prepared and stained for TEM imaging. By imaging the complete volume of multiple microspheres contained in a resin block I circumvented the problem of taking sections for TEM in random planes which might or might not contain a cellular aggregate. Cells were stained with osmium tetroxide and uranyl acetate which create contrast and make them appear white under the micro-CT scanner (*Figure 63*). PBMCs were visible in the micro-CT scan but due to the relatively large voxael size, individual bacteria were not detected. This is the first micro-CT scan of human cells infected with *Mtb* to the best of our knowledge. Phagocytosis of *Mtb* bacilli by host-derived PBMCs was confirmed by ultrathin sectioning and TEM imaging of these sections.

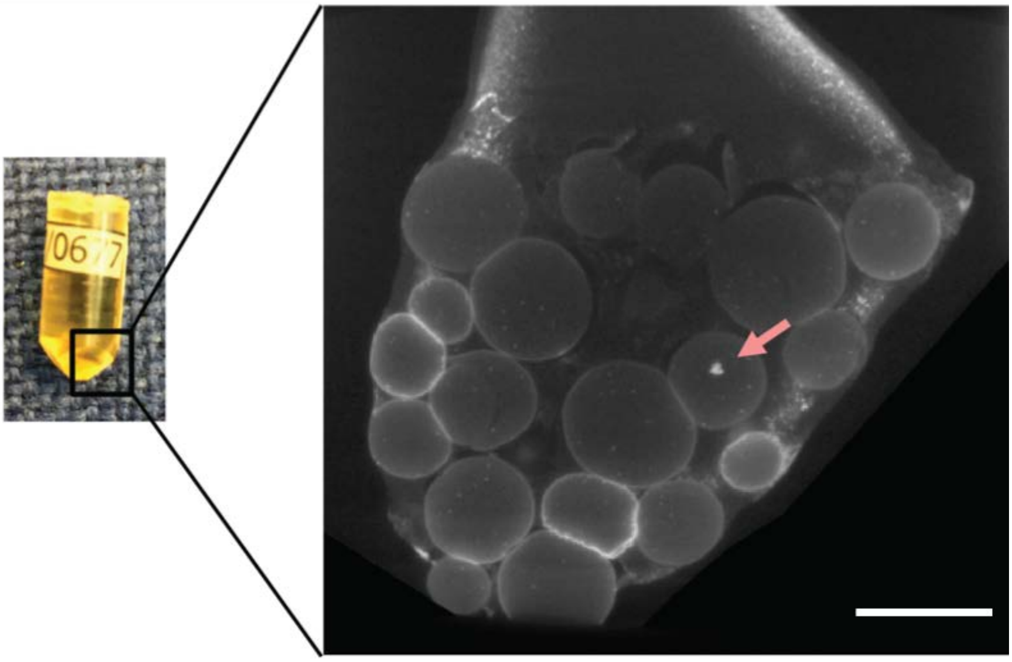

Figure 63. A resin block containing microspheres with *Mtb*-infected PBMCs was prepared for TEM imaging and scanned non-invasively with micro-CT.
(**Left**) A TAAB resin block containing microspheres with H37Rv-infected PBMCs harvested at day 14 after infection and (**right**) a single section from the 3D micro-CT stack where a cellular aggregate is detected (as bright white) as indicated by the pink arrow. Scale bar = 1 mm.

The result of this scan was then analysed and visualised using the software Amira where manual segmentation revealed at least three microspheres containing cellular aggregates. Representative still images from the video going through the full volume stack (*List of Accompanying Materials*) can be seen in *Figure 64* and a 3D visualisation of the whole stack with three aggregate-containing microspheres highlighted can be seen in *Figure 65*.

Using micro-CT, we showed that PBMCs are equally distributed throughout the microsphere matrix. However, we found that large PBMC aggregates did occur but not at the frequency that we had predicted. This might be due to the stiffness of the 3D matrix of the microspheres being too high for the cells to easily migrate in and this is a hypothesis that will be investigated in the future by other researchers in our group.

Alternatively, it may be that the donor studied had relatively reduced cellular migration, as significant donor-to-donor variability has been observed, and this can only be addressed by studying numerous donors. The time taken to image spheres by micro-CT and then perform image analysis on the stack generated is a limitation of addressing this question.

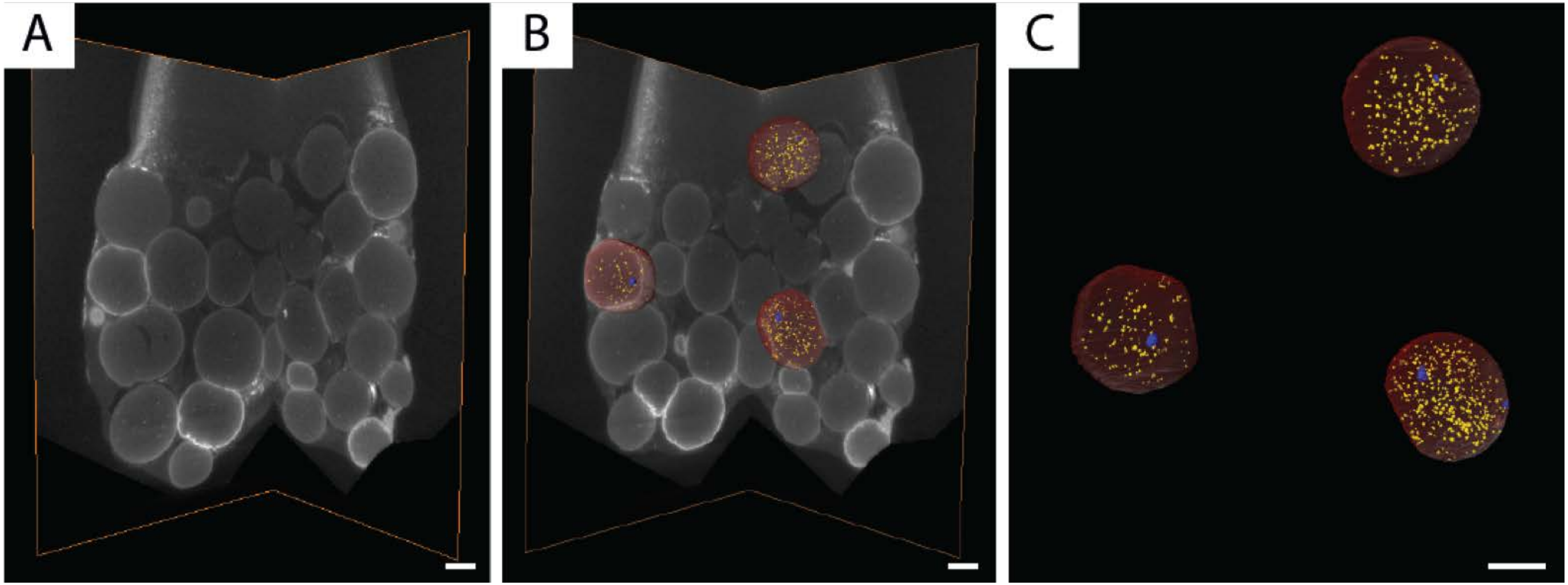

Figure 64. Micro-CT scanning of a resin block revealed aggregate-bearing microspheres at day 14 after infection with the laboratory strain H37Rv. Manual segmentation was performed in Amira to visualise aggregates (**blue**), as well as individual cells (**yellow**) and microspheres (**red**). Scale bar = 500 µm.

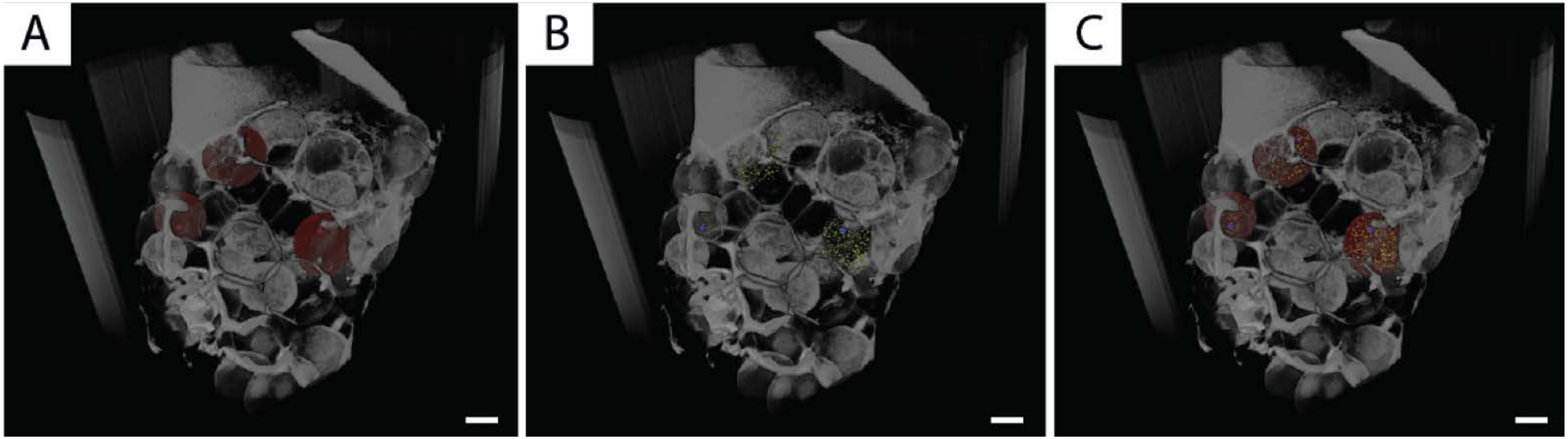

Figure 65. A 3D visualisation of the full volume stack in Amira software.

(**A**) Microspheres highlighted as **red** in the micro-CT stack, (**B**) single PBMCs (**yellow**) and PBMC aggregates (**blue**), (**C**) overlay of cells and microspheres. The lines on the left are imaging artefacts from the scanning.

5.4. Lipid bodies in host cells and ILIs in *Mtb* bacteria

Lipids are very important molecules in the biology of *Mtb*. Host lipid bodies are used as lipid stores in the cytoplasm of the cell and it is believed that *Mtb* bacilli use these host lipid stores either as building blocks to synthesise their own lipids, such as mycolic acids, or as a direct food source.[191] Some PBMCs in the microspheres were found to contain LBs (*Figure 66*).

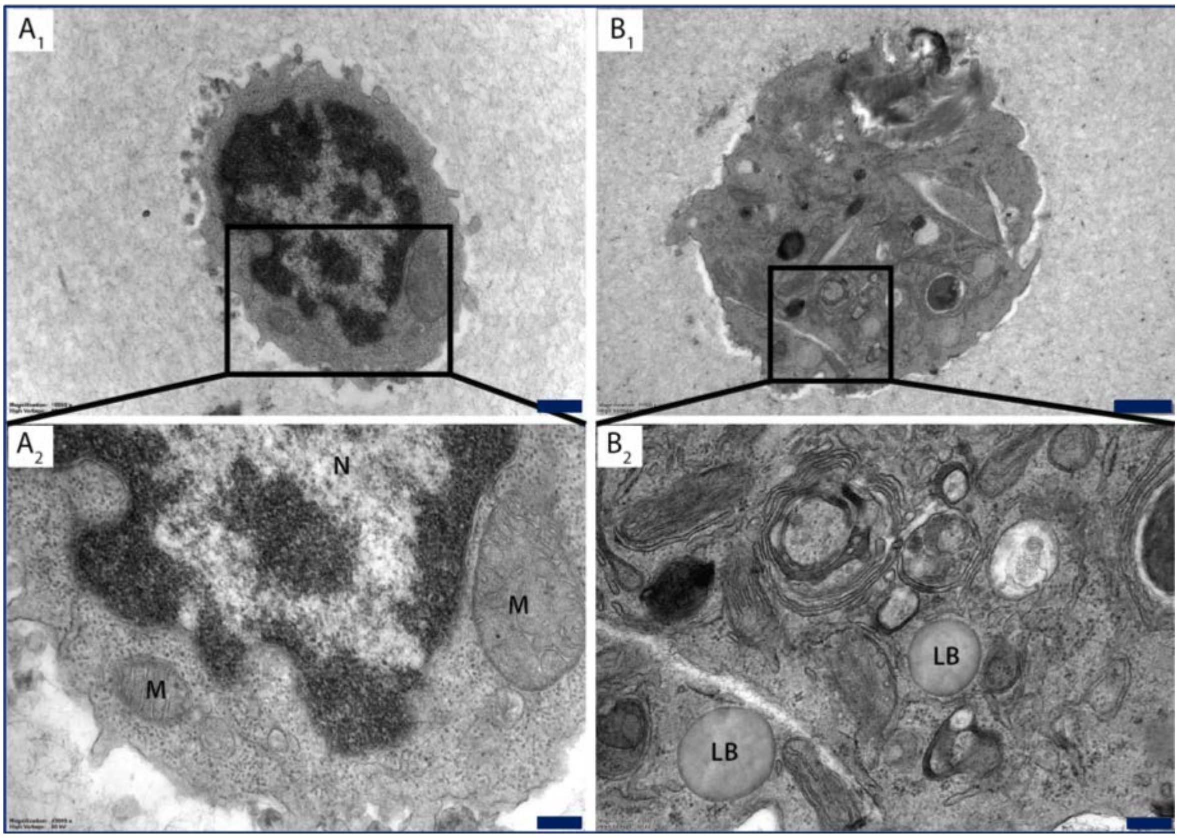

Figure 66. *Mtb*-infected PBMCs imaged with TEM have lipid bodies in their cytoplasm. (**A_{1-2}**) TEM picture of a cell from an uninfected sample with no lipid bodies in its cytoplasm. **N**: Nucleus, **M**: Mitochondrion (**B_{1-2}**) TEM picture of a cell from an *Mtb*-infected sample containing multiple lipid bodies (**LB**). Both cells are from the day 14 timepoint. Scale bars correspond to the following values: A_1 – 500 nm, B_1 – 1 μm, A_2, B_2 – 200 nm.

To generate quantitative data and further investigate this observation, at least 3 grids of each different sample were scanned with TEM. I found that there was a higher percentage of *Mtb*-infected cells that contained lipid bodies compared to the equivalent percentage of uninfected cells containing LBs and this was the case for both H37Rv and 0414B *Mtb* strains (*Figure 67A*). Additionally, the percentage of total cell area covered by LBs was significantly larger in H37Rv-infected cells than in their 0414B-infected counterparts (*Figure 67B*).

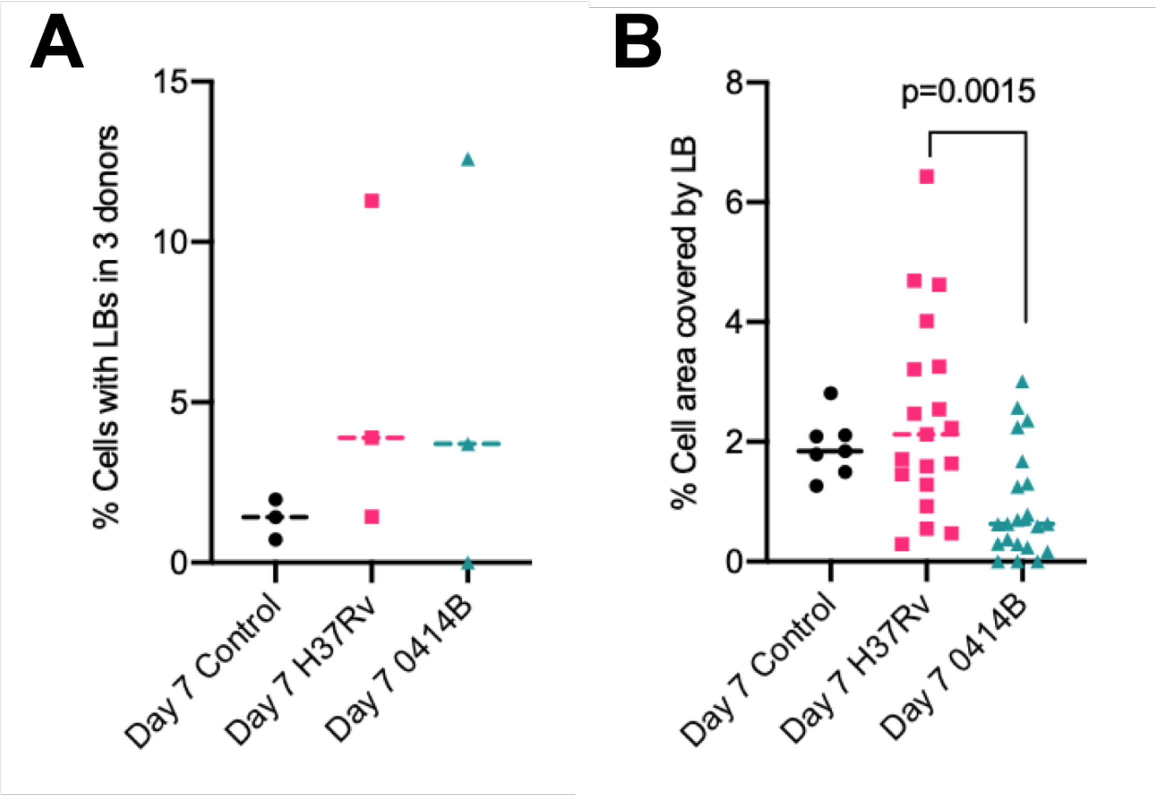

Figure 67. Dot plots related to the presence of lipid bodies in *Mtb*-infected samples. (**A**) Percentage of cells that contain lipid bodies out of the total number of cells imaged. I observed a higher percentage of *Mtb*-infected cells that presented LBs compared to the uninfected control. This was the case for both H37Rv and 0414B *Mtb* strains. The three different data points for each type of sample correspond to the three different donors examined. (**B**) Percentage of the total cell area covered by LBs in cells where LBs were encountered. Each data point corresponds to a single cell. LBs occupied larger areas of the cell in *Mtb*-infected samples with H37Rv having significantly (p=0.0015) larger areas covered by LBs compared to 0414B. Ordinary one-way ANOVA with Tukey's multiple comparisons test was performed to generate both these graphs with data from 3 different donors.

Another observation made with TEM imaging of infected cells was the presence of intracytoplasmic lipid inclusions in *Mtb* bacilli of both strains (*Figure 68*). The presence of ILIs in the cytoplasm has been associated with non-replicating persistence of mycobacteria in the latent stages of TB disease.[37] In our samples, no difference was observed in the number of ILIs between the two different strains imaged at day 7 of infection.

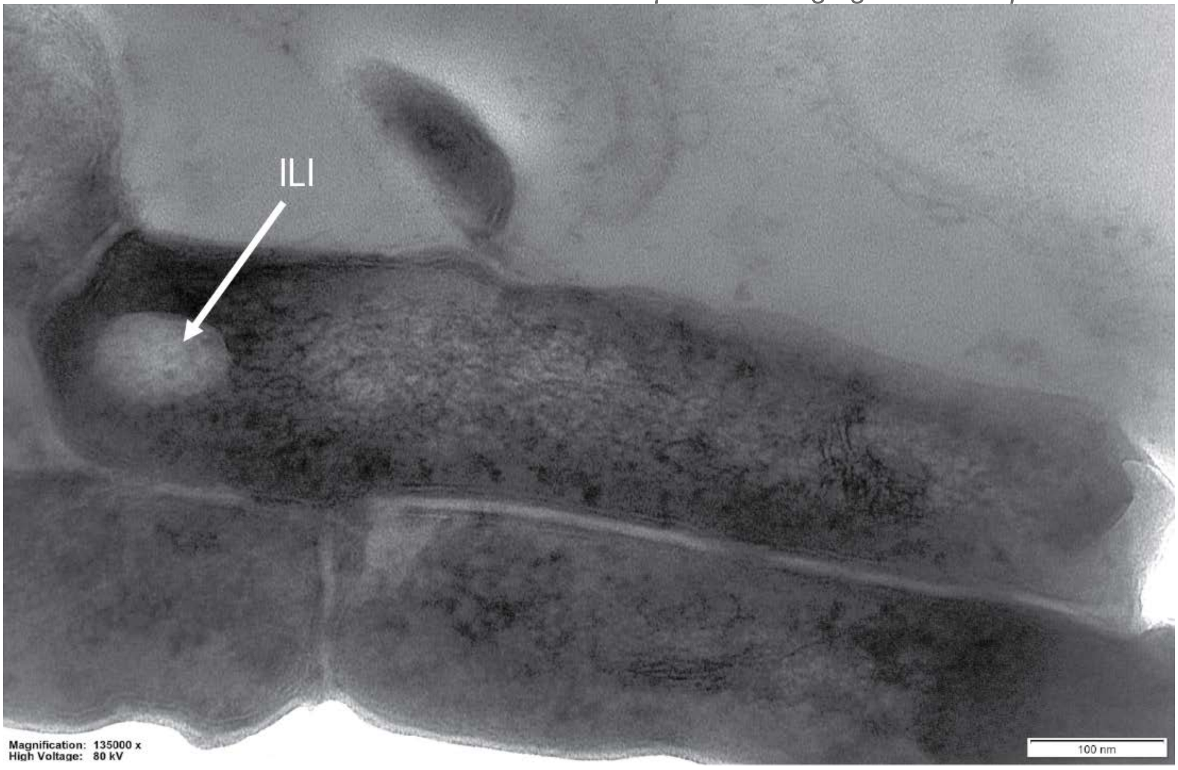

Figure 68. ***Mtb*** **bacilli at a high magnification under a TEM microscope.**

A large ILI is visible (white arrow) in the cytoplasm of one of the phagocytosed bacilli in a PBMC in a microsphere.

5.5. Discussion

In this chapter, I used a range of established techniques to image *Mtb* infection in relation to collagen presence and cell aggregation, and combined these with the method of micro-CT which is emerging in the field of biology. Collagen is the major structural protein of the extracellular matrix. Imaging of collagen fibre thickness and orientation is often investigated with SHG imaging as the molecule's non-centrosymmetric structure and high degree of crystallinity make it an excellent candidate for SHG imaging.[192] In this project, we imaged collagen with a number of different imaging techniques (including SHG microscopy) and in this chapter I showed the results of SEM and TEM imaging of type I collagen fibres within the context of a 3D cell culture matrix. SEM imaging showed that collagen fibres form thick bundles that extend through the entire diameter of the microsphere. However, in the preparatory steps for SEM imaging, microspheres are subjected to a series of ethanol-immersion steps which dehydrates them and then critical-point drying which causes them to shrink significantly. Therefore, it may be the case that due to dehydration and drying, the internal 3D matrix structure changes and what we are observing is actually an artefact of sample preparation and processing.

Another observation made using TEM was that around certain PBMCs in the microspheres, there is a capsule-like formation made out of collagen fibres. This occurred in both infected and uninfected samples. Collagen I interacts with cells by binding to their surface through a number of different cell membrane receptors; it binds to integrins that are responsible for cell adhesion,[48] the discoidin domain receptors (DDR)1 and DDR2 that exhibit tyrosine kinase activity,[49] glycoprotein VI (GPVI) that is expressed in platelets and promotes their aggregation[50] and the leukocyte-associated immunoglobulin-like receptor 1 (LAIR-1) (or CD305) which inhibits immune cell activation *in vitro*.[51] As in our microspheres we only culture PBMCs and no platelets, receptor GPVI is irrelevant to our model at the moment. Adhesion to collagen through these molecules can then affect intracellular signalling pathways, leading to altered cell survival.[1] The main mechanism(s) via which collagen binding to cell surface in the microspheres occurs remains unknown, but it was an unexpected observation that some cells seem to bind to a disproportionate amount of collagen within the microspheres. These results demonstrate how directly imaging microspheres provides different information from readouts that measure the total collagen content of multiple microspheres, and thereby validates the approach of integrating different readouts. It would be interesting to investigate whether this is mediated predominantly by one type of receptor or if it occurs via multiple receptors acting in synergy.

While trying to image TB infection of PBMCs in microspheres at a high resolution with electron microscopy, I encountered a number of technical difficulties. First of all, we start with a MOI of 0.1 which means that – in theory, based on previous experiments of the group to determine how efficient the infection process was - there is one bacillus for every ten macrophages in the microsphere. The chance of randomly sectioning (with ultramicrotomy) through the microsphere for TEM imaging and capturing an infected cell with a bacillus was, therefore, very low. Furthermore, as *Mtb* is only 2-4 μm long, even sectioning an infected macrophage does not guarantee visualising the *Mtb*, as the ultrathin section is only 0.12-0.15 μm thick. The same was true for SEM imaging and also the fact that during critical-point drying the sample significantly shrank and shrivelled, which made this problem more prominent. The other major issue I was faced with was poor resin penetration in the sample while preparing them for TEM imaging. I used Spurr and TAAB resins as they are the standard resins used in the Biomedical Imaging Unit where this work was carried out and they were always in stock. However, both of them seemed to produce resin blocks that were softer than expected and therefore most of the time could not be cut thinly enough for the microscope to be able to resolve fine structures at an extremely high level of detail (e.g. bacterial- or host-membrane continuation). Other researchers have used softer resins such as Epoxy resin. Also, in all sections, the resin seemed to be torn around bacteria[193] or in some cases around areas of intense collagen presence. We suspect that the mycolic acid wall around *Mtb* bacilli inhibits sufficient penetration of the resin, due to its extremely hydrophobic nature, creating tears on the resin around them.

One of the aims of this study was to investigate whether *Mtb* remains exclusively in the phagosome after phagocytosis or whether it can escape to the cytoplasm of the phagocyte as suggested by other groups[19] and compare this behaviour between our two strains

(H37Rv and 0414B). Due to the resin's poor penetration, I was unable to determine the number of membranes around *Mtb* bacilli to conclude whether it actually remains in the phagosome at all times. Due to the softness of the blocks and the inevitable thickness of the sections (0.12-0.15 μm instead of 0.10 μm) host membranes were poorly defined in certain areas of the section that were thicker than others, so we were unable to reach a conclusion at this point. More experiments to optimise the sample preparation method are needed in order to improve TEM imaging of *Mtb* in microspheres in the future. I would systematically vary the fixative and resin to generate harder blocks that would overcome the issue of being too soft, and also find a resin that penetrated better and was not as repelled by the *Mtb* cell wall.

I then proceeded to our second aim of this chapter which was to investigate the potential of micro-CT as an assay to detect and quantify cellular aggregation in the microspheres due to infection. We scanned a resin block prepared for TEM imaging that was at day 14 after *Mtb*-infection and managed to detect cellular aggregates as well as single PBMCs and determine their exact location in the microsphere, as micro-CT provides a real 3D image of the sample with an isotropic voxel. Therefore, we concluded that micro-CT can be used to guide TEM sectioning in order to image certain features of interest at a very high magnification and thus enter the realm of correlative imaging. Unfortunately, there was no time or funding for this work to be undertaken during the experimental part of my PhD but it is something I would aspire to pursue in the future. Micro-CT did not require any additional sample processing but the image analysis and manual segmentation that comes with it is a very laborious and slow process, which could definitely benefit from some level of automation in the workflow. Manually segmenting this specific stack took several months as it required availability of the computer workstations that have the specialist Amira/Avizo software installed in them.

An observation made by imaging hundreds of *Mtb*-infected and uninfected PBMCs with TEM was a clear trend of more cells from the *Mtb*-infected samples having lipid bodies than cells from uninfected controls. This was the case for both the ones infected with the laboratory strain H37Rv, as well as those infected with the clinical strain, 0414B. Additionally, I observed that more cells from the infected samples had lipid bodies out of the total cells imaged, compared to their uninfected counterparts. *Mtb* is known to hijack and use host lipids either as a direct energy source or as building blocks to synthesise its own lipids (e.g. mycolic acids).[194] *Mtb*-derived mycolic acids can induce accumulation of foamy macrophages in granulomas.[32] Therefore, this observation was quite interesting, showing that the microsphere system could potentially be used to study the role of lipids in TB over a longer time-course than standard cell culture experiments. The full biological significance remains to be investigated, and the type of experiments that I would anticipate would involve inhibiting specific parts of the lipid synthesis pathway, and similarly adding exogenous lipids and determining the effect on *Mtb* growth, lipid body formation and inflammatory response in the host-cells.

Summary

&

Future Work

Summary

The original idea behind my project was to investigate the potential of different emerging and traditional microscopy techniques in imaging *Mycobacterium tuberculosis* infection both in human PBMCs cultured in microspheres as well as in a human lung biopsy from a patient with active TB. Each technique required some degree of optimisation of sample processing and imaging protocols before the actual acquisition took place. However, overall, I successfully generated imaging data using a wide range of techniques, each of which had benefits and limitations, and this built my skill set across a range of platforms and analytical software.

Imaging clinical samples is important to understand human disease. The human lung biopsy of active TB disease was scanned with micro-CT to reveal features of interest that can be identified through non-invasive X-ray imaging. Human biopsies of active TB are a rare occurrence as TB patients do not routinely undergo biopsy as part of their standard clinical diagnosis and care, as TB is typically diagnosed by bronchial washing. This scan is the first micro-CT scan of an unstained tuberculous human lung biopsy to the best of our knowledge. Using micro-CT, we identified regions of caseous necrosis and matched slices in the stack with corresponding H&E-stained sections of the same block (analysis not shown as it was incomplete at the time). The next step is to adopt a correlative imaging approach to combine features revealed from staining sections with the 3D micro-CT image of the sample and this will be done as part of my ‘Research Fellow’ position in the Biomedical Imaging Unit. Since we have a large number of unstained sections from the same block, I will proceed to stain them with immunofluorescence and immunohistochemistry for different cell types in order to then enrich the micro-CT 3D stack with more cellular information. At this point, the micro-CT provides information about the complexity of a human lung lesion, with much greater variation than the standard cartoon depiction of granulomas, but at the same time the resolution and detail falls well short of that obtained by standard H&E staining. This primarily results from the relatively similar Hounsfield units across tissue, so that obtaining contrast between different parts of the tissue is challenging. Gaining greater information from micro-CT of tissue blocks is the main next technical challenge for the methodology.

However, a biopsy is merely a ‘snapshot’ of the disease, frozen in the moment when it was extracted. In order to investigate the dynamic immunological processes of the disease and especially in its early stages, we used an *in vitro* 3D cell culture (‘microsphere’) model produced in our group with freshly isolated PBMCs from whole blood. 3D cell cultures offer distinct advantages over traditional 2D cell cultures such as a more natural cell shape, cell-cell and cell-ECM interactions and mechanical stimuli in 3D. For the purposes of this thesis I studied our microsphere model of *Mtb* infection with a range of different emerging and traditional imaging techniques.

The first group of imaging techniques I used to image the microspheres without the need of extensive preparatory steps was collectively called ‘label-free imaging’. Label-free imaging is non-invasive, requires no sample preparation and can give almost confocal-like results. After chemically characterising the matrix and its raw components with Raman spectroscopy, I then imaged collagen fibres with SHG and PBMCs with CARS and TPEF. As collagen in the microsphere matrix was in a very low concentration, it could not be detected with Raman spectroscopy so the techniques could not be used to monitor matrix turnover in the microspheres. It did however teach me valuable lessons that helped me achieve better CARS (Raman-based) imaging in the next stages. CARS microscopy could identify cell membranes in the microspheres and SHG microscopy successfully imaged collagen fibres in the microsphere matrix. The home-built CARS/SHG and SHG/TPEF setups came with a number of limitations relating to throughput, day-to-day variations in machine performance and (at the time) lack of capability to acquire z-stacks. Overall, label-free imaging seemed promising in principle, but the technology needed more time to reach the stage where it could effectively be used on a complex sample such as 3D microspheres incorporating cells. I did not achieve the reproducibility and quantitative readouts necessary to use label-free imaging as a standard readout for experiments where the conditions were varied, however, I see some potential in them for the future.

Therefore, I moved onto more traditional techniques such as transmission and scanning electron microscopy, and also emerging in the biomedical field but more established techniques like micro-CT. TEM provides greatly detailed imaging of *Mtb* infection of PBMCs in microspheres but has the problem of ultrathin sectioning being at completely random depths in the resin block. The other limitation is poor resin penetration, which most likely occurs due to the lipid-rich wall outside the mycobacterial cell membrane. The approach definitely gave novel information that has raised questions about the microsphere matrix, such as the interesting observation of collagen fibres attached to the surface of some, but not all, PBMCs. This warrants further investigation, to determine what proportion of cells have ‘capsules’, how this affects cell survival and at what point they form within microspheres. TEM revealed the presence of more lipid bodies in infected cells compared to their uninfected counterparts. Micro-CT showed cell aggregation in microspheres and I have identified its great potential in being used to guide ultramicrotomy sectioning of resin blocks for targeted TEM imaging of cell aggregates.

The overall conclusion of my PhD is that the different imaging techniques complement each other in a way that highlights the value and importance of correlative imaging approaches. Modelling the complexity of human TB disease has proven to be a very daunting task, with our microsphere model merely being a simplistic replication of the actual *Mtb* infection, albeit probably the most advanced in vitro model of TB to date.[195] My project shows how important it is to accompany molecular, biochemical and microbiological assays with some sort of imaging of the actual process/feature in the sample (preferably different kinds of imaging that could be correlated). Studying the microspheres with all these different microscopy techniques has made us challenge preconceived ideas we had about the structure of the matrix as well as the behaviour of the cells in it. For example, I did not at any point detect collagen fibres cross-linking with the alginate network which is something that previous data acquired in the group had suggested. Cells were thought to form quite a few aggregates in every microsphere but 3D imaging of the spheres with micro-CT showed that aggregates are in fact quite a rare occurrence in microspheres. These observations along with all the rest mentioned previously in this thesis, will contribute to us fine-tuning the conditions of microsphere generation and re-thinking our 3D cell culture model and how to optimise it and make it recapitulate the real conditions of human TB infection even better.

The next potential steps forward for the system would include trying to increase the cellular complexity of the model, such as by adding fibroblasts to the culture, or varying other parameters such as the extracellular matrix by adding fibrin, fibronectin, elastin, whole lung extract or other components. Additionally, the environment microspheres are cultured in can be systematically varied, such as placing them in hypoxic conditions. In terms of imaging, the primary challenges that I perceive is to improve it by further optimising sample preparation protocols as well as image acquisition and analysis workflows so that quantitative data can be generated as a readout for biological interventions.

Future work

Human biopsy tissue

First, I would like to stain more sections from our lung biopsy with immunostaining and perform correlative imaging on the data acquired. The newly stained sections along with the H&E stained sections we already prepared will then be registered onto the micro-CT dataset to extract the maximal amount of information from a single CT scan of a lung biopsy. We also intend to scan and do the same for a larger number of clinical samples of TB. Another relevant aim of my post-doctoral position is to make the image analysis workflow more automated and user-friendly.

Collagen localisation and turnover

Providing that the potential for z-stack acquisition was added onto the SHG setup, I could use this technique to image collagen fibres and investigate their localisation and orientation in the microsphere matrix. Therefore, SHG in 3D could also be used to demonstrate collagen turnover during *Mtb*-infection in a quantitative or semi-quantitative way.[196] It would also be useful to perform quantitative analysis on collagen in microspheres using more established collagen quantitation kits to corroborate SHG findings.

Cellular aggregation

Reducing micro-CT scan times and accelerating post-acquisition image processing and analysis by automating either the whole process or part of it would enable us to use it as a non-invasive readout for cellular aggregation in the microspheres during *Mtb*-infection. CARS microscopy could also be used as a non-invasive readout for cell aggregation, requiring no sample preparation, although it would be limited by an imaging depth of 200 µm.

Mtb localisation and 3D EM imaging

To investigate whether *Mtb* escapes from the phagosome to the cytosol of the host phagocyte, I would use micro-CT to guide me to a cellular aggregate, which is bound to have at least one infected cell in the middle of it, and then perform serial block-face scanning electron microscopy (SBF-SEM) (using the Gatan 3View imaging setup available in the BIU). The Gatan 3View takes serial sections off the face of the resin block and scans the block-face in between the sectioning to create a z-stack of very high-resolution SEM images. This way, after some manual segmentation we could re-create the 3D image of every single phagocytosed bacillus and determine whether any of them are in the cytosol as opposed to the phagosome. This type of experiment would certainly require for the sample processing protocols to be optimised first so that we maximise resin penetration and resin block hardness is sufficient to produce good quality sections. Furthermore, developing the methodology so that the micro-CT can guide the area to be sectioned on another instrument presents a logistic challenge, with the need for fixed reference points and accurate measurements.

References

1. Al Shammari B, Shiomi T, Tezera L, et al. The Extracellular Matrix Regulates Granuloma Necrosis in Tuberculosis. *Journal of Infectious Diseases* 2015;212(3):463-73.

2. O'Garra A, Redford PS, McNab FW, et al. The immune response in tuberculosis. *Annual Review of Immunology* 2013;31:475-527.

3. Organization GWH. Global Tuberculosis Report. 2016.

4. Organization GWH. Global Tuberculosis Report, 2019.

5. Organization GWH. Global Tuberculosis Report, 2018.

6. Organization GWH. Global Tuberculosis Report, 2017.

7. Cheon SA, Cho HH, Kim J, et al. Recent tuberculosis diagnosis toward the end TB strategy. *Journal of Microbiological Methods* 2016;123:51-61.

8. Leibert E, Danckers M, Rom WN. New drugs to treat multidrug-resistant tuberculosis: the case for bedaquiline. *Therapeutics and Clinical Risk Management* 2014;10:597-602.

9. Yan L, Xiao H, Zhang Q. Systematic review: Comparison of Xpert MTB/RIF, LAMP and SAT methods for the diagnosis of pulmonary tuberculosis. *Tuberculosis* 2016;96:75-86.

10. Gandhi NR, Nunn P, Dheda K, et al. Multidrug-resistant and extensively drug-resistant tuberculosis: a threat to global control of tuberculosis. *The Lancet* 2010;375(9728):1830-43.

11. Chung-Delgado K, Guillen-Bravo S, Revilla-Montag A, et al. Mortality among MDR-TB Cases: Comparison with Drug-Susceptible Tuberculosis and Associated Factors. *PLoS One* 2015;10(3):e0119332.

12. Jassal M, Bishai WR. Extensively drug-resistant tuberculosis. *The Lancet Infectious Diseases* 2009;9(1):19-30.

13. Buijtels PC, Willemse-Erix HF, Petit PL, et al. Rapid identification of mycobacteria by Raman spectroscopy. *Journal of Clinical Microbiology* 2008;46(3):961-5.

14. Darby J, Black J, Buising K. Interferon-gamma release assays and the diagnosis of tuberculosis: have they found their place? *Internal Medicine Journal* 2014;44(7):624-32.

15. Gil O, Diaz I, Vilaplana C, et al. Granuloma encapsulation is a key factor for containing tuberculosis infection in minipigs. *PLoS One* 2010;5(4):e10030.

16. Elkington PT, Friedland JS. Permutations of time and place in tuberculosis. *The Lancet Infectious Diseases* 2015;15(11):1357-60.

17. Nunes-Alves C, Booty MG, Carpenter SM, et al. In search of a new paradigm for protective immunity to TB. *Nature reviews. Microbiology* 2014;12(4):289-99.

18. Jamwal SV, Mehrotra P, Singh A, et al. Mycobacterial escape from macrophage phagosomes to the cytoplasm represents an alternate adaptation mechanism. *Scientific Reports* 2016;6:23089.

19. van der Wel N, Hava D, Houben D, et al. *M. tuberculosis* and *M. leprae* translocate from the phagolysosome to the cytosol in myeloid cells. *Cell* 2007;129(7):1287-98.

20. Parasa VR, Rahman MJ, Ngyuen Hoang AT, et al. Modeling *Mycobacterium tuberculosis* early granuloma formation in experimental human lung tissue. *Disease Models & Mechanisms* 2014;7(2):281-88.

21. Behar SM, Martin CJ, Booty MG, et al. Apoptosis is an innate defense function of macrophages against *Mycobacterium tuberculosis*. *Mucosal Immunology* 2011;4(3):279-87.

22. Nagata S, Golstein P. The Fas death factor. *Science* 1995;267(5203):1449-56.

23. Oddo M, Renno T, Attinger A, et al. Fas ligand-induced apoptosis of infected human macrophages reduces the viability of intracellular *Mycobacterium tuberculosis*. *The Journal of Immunology* 1998;160(11):5448-54.

24. Sylvius LBF. *Opera Medica*. Venice, Italy: Ex Typographia Hertziana; 1679.

25. Ramakrishnan L. Revisiting the role of the granuloma in tuberculosis. *Nature Reviews Immunology* 2012;12(5):352-66.

26. Sandor M, Weinstock JV, Wynn TA. Response to Doenhoff: Granulomas: these gizmos are cool! *Trends in Immunology* 2003;24(4):169-70.

27. Davis JM, Ramakrishnan L. The role of the granuloma in expansion and dissemination of early tuberculous infection. *Cell* 2009;136(1):37-49.

28. Orme IM, Cooper AM. Cytokine/chemokine cascades in immunity to tuberculosis. *Immunology Today* 1999;20(7):307-12.

29. Saunders BM, Cooper AM. Restraining mycobacteria: role of granulomas in mycobacterial infections. *Immunology & Cell Biology* 2000;78(4):334-41.

30. Tsai MC, Chakravarty S, Zhu G, et al. Characterization of the tuberculous granuloma in murine and human lungs: cellular composition and relative tissue oxygen tension. *Cellular Microbiology* 2006;8(2):218-32.

31. Fortune SM, Solache A, Jaeger A, et al. *Mycobacterium tuberculosis* Inhibits Macrophage Responses to IFN-γ through Myeloid Differentiation Factor 88-Dependent and -Independent Mechanisms. *The Journal of Immunology* 2004;172(10):6272-80.

32. Peyron P, Vaubourgeix J, Poquet Y, et al. Foamy macrophages from tuberculous patients' granulomas constitute a nutrient-rich reservoir for *M. tuberculosis* persistence. *PLOS Pathogens* 2008;4(11):e1000204.

33. Cronan MR, Beerman RW, Rosenberg AF, et al. Macrophage Epithelial Reprogramming Underlies Mycobacterial Granuloma Formation and Promotes Infection. *Immunity* 2016;45(4):861-76.

34. Lay G, Poquet Y, Salek-Peyron P, et al. Langhans giant cells from *M. tuberculosis*-induced human granulomas cannot mediate mycobacterial uptake. *The Journal of Pathology* 2007;211(1):76-85.

35. Guerrini V, Prideaux B, Blanc L, et al. Storage lipid studies in tuberculosis reveal that foam cell biogenesis is disease-specific. *PLOS Pathogens* 2018;14(8):e1007223.

36. Caire-Brändli I, Papadopoulos A, Malaga W, et al. Reversible lipid accumulation and associated division arrest of Mycobacterium avium in lipoprotein-induced foamy macrophages may resemble key events during latency and reactivation of tuberculosis. *Infection and Immunity* 2014;82(2):476-90.

37. Garton NJ, Christensen H, Minnikin DE, et al. Intracellular lipophilic inclusions of mycobacteria in vitro and in sputum. *Microbiology* 2002;148(Pt 10):2951-8.

38. Garton NJ, Waddell SJ, Sherratt AL, et al. Cytological and transcript analyses reveal fat and lazy persister-like bacilli in tuberculous sputum. *PLoS medicine* 2008;5(4):e75-e75.

39. Ouimet M, Koster S, Sakowski E, et al. Mycobacterium tuberculosis induces the miR-33 locus to reprogram autophagy and host lipid metabolism. *Nature immunology* 2016;17:677.

40. Cardona P-J. A Spotlight on Liquefaction: Evidence from Clinical Settings and Experimental Models in Tuberculosis. *Clinical and Developmental Immunology* 2011;2011:868246.

41. Ordonez AA, Tasneen R, Pokkali S, et al. Mouse model of pulmonary cavitary tuberculosis and expression of matrix metalloproteinase-9. *Disease Models & Mechanisms* 2016;9(7):779-88.

42. Subbian S, Tsenova L, Yang G, et al. Chronic pulmonary cavitary tuberculosis in rabbits: a failed host immune response. *Open biology* 2011;1(4):110016.

43. Dannenberg AM, Jr. Liquefaction and cavity formation in pulmonary TB: a simple method in rabbit skin to test inhibitors. *Tuberculosis (Edinb)* 2009;89(4):243-7.

44. Ehlers S, Schaible UE. The Granuloma in Tuberculosis: Dynamics of a Host–Pathogen Collusion. *Frontiers in Immunology* 2012;3:411.

45. Harvey Lodish AB, S. Lawrence Zipursky, Paul Matsudaira, David Baltimore and James Darnell. *Molecular Cell Biology*. 4th ed. New York, NY: W. H. Freeman & Co.; 2000.

46. Davidson JM. Biochemistry and turnover of lung interstitium. *European Respiratory Journal* 1990;3(9):1048-63.

47. Cicchi R, Vogler N, Kapsokalyvas D, et al. From molecular structure to tissue architecture: collagen organization probed by SHG microscopy. *Journal of Biophotonics* 2013;6(2):129-42.

48. Heino J. The collagen family members as cell adhesion proteins. *Bioessays* 2007;29(10):1001-10.

49. Mohan RR, Mohan RR, Wilson SE. Discoidin Domain Receptor (DDR) 1 and 2: collagen-activated tyrosine kinase receptors in the cornea. *Experimental Eye Research* 2001;72(1):87-92.

50. Nurden AT. Clinical significance of altered collagen-receptor functioning in platelets with emphasis on glycoprotein VI. *Blood Reviews* 2019;38:100592.

51. Smith CW, Thomas SG, Raslan Z, et al. Mice lacking the inhibitory collagen receptor LAIR-1 exhibit a mild thrombocytosis and hyperactive platelets. *Arteriosclerosis, Thrombosis, and Vascular Biology* 2017;37(5):823-35.

52. Frantz C, Stewart KM, Weaver VM. The extracellular matrix at a glance. *Journal of Cell Science* 2010;123(Pt 24):4195-200.

53. Palomo T, Vilaça T, Lazaretti-Castro M. Osteogenesis imperfecta: diagnosis and treatment. *Current Opinion in Endocrinology, Diabetes and Obesity* 2017;24(6):381-88.

54. Parapia LA, Jackson C. Ehlers-Danlos syndrome – a historical review. *British Journal of Haematology* 2008;141(1):32-35.

55. Bitterman AD, Sponseller PD. Marfan Syndrome: A Clinical Update. *JAAOS - Journal of the American Academy of Orthopaedic Surgeons* 2017;25(9):603-09.

56. Jarvelainen H, Sainio A, Koulu M, et al. Extracellular matrix molecules: potential targets in pharmacotherapy. *Pharmacological Reviews* 2009;61(2):198-223.

57. White ES. Lung extracellular matrix and fibroblast function. *Annals of the American Thoracic Society* 2015;12 Suppl 1:S30-3.

58. Brinckerhoff CE, Matrisian LM. Matrix metalloproteinases: a tail of a frog that became a prince. *Nature Reviews Molecular Cell Biology* 2002;3(3):207-14.

59. Visse R, Nagase H. Matrix metalloproteinases and tissue inhibitors of metalloproteinases: structure, function, and biochemistry. *Circulation Research* 2003;92(8):827-39.

60. Ramos-Martinez AG, Enciso-Moreno JA, Espinosa-Ayala I, et al. Expression kinetics of metalloproteinases and their tissue inhibitors in experimental murine pulmonary tuberculosis. *Experimental Lung Research* 2015;41(1):1-11.

61. Elkington PT, Ugarte-Gil CA, Friedland JS. Matrix metalloproteinases in tuberculosis. *European Respiratory Journal* 2011;38(2):456-64.

62. Elkington P, Shiomi T, Breen R, et al. MMP-1 drives immunopathology in human tuberculosis and transgenic mice. *The Journal of Clinical Investigation* 2011;121(5):1827-33.

63. Ugarte-Gil CA, Elkington P, Gilman RH, et al. Induced Sputum MMP-1, -3 & -8 Concentrations during Treatment of Tuberculosis. *PLoS One* 2013;8(4):e61333.

64. Friedland JS, Shaw TC, Price NM, et al. Differential regulation of MMP-1/9 and TIMP-1 secretion in human monocytic cells in response to *Mycobacterium tuberculosis*. *Matrix Biology* 2002;21(1):103-10.

65. Chang JC, Wysocki A, Tchou-Wong KM, et al. Effect of *Mycobacterium tuberculosis* and its components on macrophages and the release of matrix metalloproteinases. *Thorax* 1996;51(3):306-11.

66. Chen WL, Sheu JR, Chen RJ, et al. *Mycobacterium tuberculosis* Upregulates TNF-alpha Expression via TLR2/ERK Signaling and Induces MMP-1 and MMP-9 Production in Human Pleural Mesothelial Cells. *PLoS One* 2015;10(9):e0137979.

67. Elkington PT, D'Armiento JM, Friedland JS. Tuberculosis Immunopathology: The Neglected Role of Extracellular Matrix Destruction. *Science translational medicine* 2011;3(71):71ps6-71ps6.

68. Subbian S, Tsenova L, O'Brien P, et al. Spontaneous Latency in a Rabbit Model of Pulmonary Tuberculosis. *The American Journal of Pathology* 2012;181(5):1711-24.

69. Dharmadhikari AS, Nardell EA. What Animal Models Teach Humans about Tuberculosis. *American Journal of Respiratory Cell and Molecular Biology* 2008;39(5):503-08.

70. Puissegur MP, Botanch C, Duteyrat JL, et al. An *in vitro* dual model of mycobacterial granulomas to investigate the molecular interactions between mycobacteria and human host cells. *Cellular Microbiology* 2004;6(5):423-33.

71. Meeker ND, Trede NS. Immunology and zebrafish: spawning new models of human disease. *Developmental & Comparative Immunology* 2008;32(7):745-57.

72. Manabe YC, Dannenberg AM, Tyagi SK, et al. Different strains of *Mycobacterium tuberculosis* cause various spectrums of disease in the rabbit model of tuberculosis. *Infection and Immunity* 2003;71(10):6004-11.

73. Buddle BM, Skinner MA, Neil Wedlock D, et al. Cattle as a model for development of vaccines against human tuberculosis. *Tuberculosis* 2005;85(1–2):19-24.

74. Rui-An Wang Z-YKYLTYJ-HQ, Li W. Why is *Mycobacterium Tuberculosis* Hard to Grow? The Principle of Biorelativity Explains. *Journal of Clinical & Experimental Pathology* 2014;4(3):-.

75. Ghodbane R, Raoult D, Drancourt M. Dramatic reduction of culture time of *Mycobacterium tuberculosis*. *Scientific Reports* 2014;4:4236.

76. Ravi M, Paramesh V, Kaviya SR, et al. 3D cell culture systems: advantages and applications. *Journal of Cellular Physiology* 2015;230(1):16-26.

77. Workman VL, Tezera LB, Elkington PT, et al. Controlled Generation of Microspheres Incorporating Extracellular Matrix Fibrils for Three-Dimensional Cell Culture. *Advanced Functional Materials* 2014;24(18):2648-57.

78. Choi JS, Mahadik BP, Harley BA. Engineering the hematopoietic stem cell niche: Frontiers in biomaterial science. *Biotechnology Journal* 2015;10(10):1529-45.

79. Baker BM, Chen CS. Deconstructing the third dimension – how 3D culture microenvironments alter cellular cues. *Journal of Cell Science* 2012;125(13):3015-24.

80. Bonnier F, Meade AD, Merzha S, et al. Three dimensional collagen gels as a cell culture matrix for the study of live cells by Raman spectroscopy. *Analyst* 2010;135(7):1697-703.

81. Schwartz MA, Chen CS. Deconstructing Dimensionality. *Science* 2013;339(6118):402-04.

82. Mortati L, Divieto C, Sassi MP. CARS and SHG microscopy to follow collagen production in living human corneal fibroblasts and mesenchymal stem cells in fibrin hydrogel 3D cultures. *Journal of Raman Spectroscopy* 2012;43(5):675-80.

83. Justice BA, Badr NA, Felder RA. 3D cell culture opens new dimensions in cell-based assays. *Drug Discovery Today* 2009;14(1-2):102-7.

84. Weigelt B, Ghajar CM, Bissell MJ. The need for complex 3D culture models to unravel novel pathways and identify accurate biomarkers in breast cancer. *Advanced Drug Delivery Reviews* 2014;69-70:42-51.

85. Matsusaki M, Case CP, Akashi M. Three-dimensional cell culture technique and pathophysiology. *Advanced Drug Delivery Reviews* 2014;74:95-103.

86. Campbell JJ, Husmann A, Hume RD, et al. Development of three-dimensional collagen scaffolds with controlled architecture for cell migration studies using breast cancer cell lines. *Biomaterials* 2017;114:34-43.

87. Thoma CR, Zimmermann M, Agarkova I, et al. 3D cell culture systems modeling tumor growth determinants in cancer target discovery. *Advanced Drug Delivery Reviews* 2014;69-70:29-41.

88. Godugu C, Patel AR, Desai U, et al. AlgiMatrix based 3D cell culture system as an *in vitro* tumor model for anticancer studies. *PLoS One* 2013;8(1):e53708.

89. Astashkina A, Grainger DW. Critical analysis of 3-D organoid *in vitro* cell culture models for high-throughput drug candidate toxicity assessments. *Advanced Drug Delivery Reviews* 2014;69-70:1-18.

90. do Nascimento Pedrosa T, De Vuyst E, Mound A, et al. Methyl-beta-cyclodextrin treatment combined to incubation with interleukin-4 reproduces major features of atopic dermatitis in a 3D-culture model. *Archives of Dermatological Research* 2017;309(1):63-69.

91. Choi SH, Kim YH, Hebisch M, et al. A three-dimensional human neural cell culture model of Alzheimer's disease. *Nature* 2014;515(7526):274-8.

92. Schmid T, Messmer A, Yeo BS, et al. Towards chemical analysis of nanostructures in biofilms II: tip-enhanced Raman spectroscopy of alginates. *Analytical and Bioanalytical Chemistry* 2008;391(5):1907-16.

93. Matsuhiro B, Martínez-Gómez F, Mansilla A. Vibrational spectroscopy characterization of sodium alginate and its heteropolymeric and homopolymeric block fractions *Alginic Acid: Chemical Structure, Uses and Health Benefits*; 2015 p89-103.

94. Xu G, Cheng L, Zhang Q, et al. *In situ* thiolated alginate hydrogel: Instant formation and its application in hemostasis. *Journal of Biomaterials Applications* 2016.

95. Cox G, Kable E, Jones A, et al. 3-dimensional imaging of collagen using second harmonic generation. *Journal of Structural Biology* 2003;141(1):53-62.

96. Cox GC, Manconi F, Kable E. Second harmonic imaging of collagen in mammalian tissue. 2002;4620:148-56.

97. Tezera LB, Bielecka MK, Chancellor A, et al. Dissection of the host-pathogen interaction in human tuberculosis using a bioengineered 3-dimensional model. *eLife* 2017;6:e21283.

98. Bielecka MK, Tezera LB, Zmijan R, et al. A Bioengineered Three-Dimensional Cell Culture Platform Integrated with Microfluidics To Address Antimicrobial Resistance in Tuberculosis. *MBio* 2017;8(1):e02073-16.

99. Ahlf DR, Masyuko RN, Hummon AB, et al. Correlated mass spectrometry imaging and confocal Raman microscopy for studies of three-dimensional cell culture sections. *Analyst* 2014;139(18):4578-85.

100. Winterhalder MJ, Zumbusch A. Beyond the borders — Biomedical applications of non-linear Raman microscopy. *Advanced Drug Delivery Reviews* 2015;89:135-44.

101. Taatjes DJ, Mossman BT. *Cell Imaging Techniques: Methods and Protocols*: Humana Press; 2006.

102. Ellis DI, Cowcher DP, Ashton L, et al. Illuminating disease and enlightening biomedicine: Raman spectroscopy as a diagnostic tool. *Analyst* 2013;138(14):3871-84.

103. Das RS, Agrawal YK. Raman spectroscopy: Recent advancements, techniques and applications. *Vibrational Spectroscopy* 2011;57(2):163-76.

104. Campagnola PJ, Clark HA, Mohler WA, et al. Second-harmonic imaging microscopy of living cells. *Journal of Biomedical Optics* 2001;6(3):277-86.

105. Campagnola PJ, Dong CY. Second harmonic generation microscopy: principles and applications to disease diagnosis. *Laser & Photonics Reviews* 2011;5(1):13-26.

106. Welsher K, Sherlock SP, Dai H. Deep-tissue anatomical imaging of mice using carbon nanotube fluorophores in the second near-infrared window. *Proceedings of the National Academy of Sciences* 2011;108(22):8943-48.

107. Yue S, Cardenas-Mora JM, Chaboub LS, et al. Label-free analysis of breast tissue polarity by Raman imaging of lipid phase. *Biophysical Journal* 2012;102(5):1215-23.

108. Smith E, Dent G. Introduction, Basic Theory and Principles *Modern Raman Spectroscopy – A Practical Approach*: John Wiley & Sons, Ltd; 2005 p1-21.

109. Austin LA, Osseiran S, Evans CL. Raman technologies in cancer diagnostics. *Analyst* 2016;141(2):476-503.

110. Butler HJ, Ashton L, Bird B, et al. Using Raman spectroscopy to characterize biological materials. *Nature Protocols* 2016;11(4):664-87.

111. Begley RF, Harvey AB, Byer RL. Coherent anti‐Stokes Raman spectroscopy. *Applied Physics Letters* 1974;25(7):387-90.

112. Zhang X, Roeffaers MBJ, Basu S, et al. Label-free Live Cell Imaging of Nucleic Acids using Stimulated Raman Scattering (SRS) Microscopy. *Chemphyschem : a European journal of chemical physics and physical chemistry* 2012;13(4):1054-59.

113. Pestov D, Murawski RK, Ariunbold GO, et al. Optimizing the Laser-Pulse Configuration for Coherent Raman Spectroscopy. *Science* 2007;316(5822):265-68.

114. Konorov SO, Blades MW, Turner RF. Non-resonant background suppression by destructive interference in coherent anti-Stokes Raman scattering spectroscopy. *Optics Express* 2011;19(27):25925-34.

115. Krafft C, Dietzek B, Schmitt M, et al. Raman and coherent anti-Stokes Raman scattering microspectroscopy for biomedical applications. *Journal of Biomedical Optics* 2012;17(4):040801.

116. Zoumi A, Yeh A, Tromberg BJ. Imaging cells and extracellular matrix in vivo by using second-harmonic generation and two-photon excited fluorescence. *Proceedings of the National Academy of Sciences of the United States of America* 2002;99(17):11014-19.

117. Denk W, Strickler JH, Webb WW. Two-photon laser scanning fluorescence microscopy. *Science* 1990;248(4951):73-6.

118. Coda S, Siersema PD, Stamp GWH, et al. Biophotonic endoscopy: a review of clinical research techniques for optical imaging and sensing of early gastrointestinal cancer. *Endoscopy International Open* 2015;03(05):E380-E92.

119. Masters BR, So PT. Multi-photon excitation microscopy and confocal microscopy imaging of *in vivo* human skin: a comparison. *Microscopy and Microanalysis* 1999;5(4):282-89.

120. Pascut FC, Goh HT, Welch N, et al. Noninvasive detection and imaging of molecular markers in live cardiomyocytes derived from human embryonic stem cells. *Biophysical Journal* 2011;100(1):251-9.

121. Jess PR, Smith DD, Mazilu M, et al. Early detection of cervical neoplasia by Raman spectroscopy. *International Journal of Cancer* 2007;121(12):2723-8.

122. Rösch P, Schmitt M, Kiefer W, et al. The identification of microorganisms by micro-Raman spectroscopy. *Journal of Molecular Structure* 2003;661–662:363-69.

123. Moura CC, Tare RS, Oreffo ROC, et al. Raman spectroscopy and coherent anti-Stokes Raman scattering imaging: prospective tools for monitoring skeletal cells and skeletal regeneration. *Journal of the Royal Society Interface* 2016;13(118):20160182.

124. Zipfel WR, Williams RM, Christie R, et al. Live tissue intrinsic emission microscopy using multiphoton-excited native fluorescence and second harmonic generation. *Proceedings of the National Academy of Sciences of the United States of America* 2003;100(12):7075-80.

125. Wang H, Fu Y, Zickmund P, et al. Coherent Anti-Stokes Raman Scattering Imaging of Axonal Myelin in Live Spinal Tissues. *Biophysical Journal*;89(1):581-91.

126. Mitchell A, Ashton L, Yang XB, et al. Detection of early stage changes associated with adipogenesis using Raman spectroscopy under aseptic conditions. *Cytometry* 2015;87(11):1012-19.

127. Vaulkner A. Coherent Raman Scattering Microscopy. In: Matousek P, Morris, Michael (ed.) *Emerging Raman Applications and Techniques in Biomedical and Pharmaceutical Fields*; 2009 p111-52.

128. Liu T-T, Lin Y-H, Hung C-S, et al. A High Speed Detection Platform Based on Surface-Enhanced Raman Scattering for Monitoring Antibiotic-Induced Chemical Changes in Bacteria Cell Wall. *PLoS One* 2009;4(5):e5470.

129. Le TT, Huff TB, Cheng J-X. Coherent anti-Stokes Raman scattering imaging of lipids in cancer metastasis. *BMC Cancer* 2009;9(1):42.

130. Huff TB, Cheng JX. *In vivo* coherent anti-Stokes Raman scattering imaging of sciatic nerve tissue. *Journal of Microscopy* 2007;225(Pt 2):175-82.

131. Henry FP, Côté D, Randolph MA, et al. Real-time *in vivo* assessment of the nerve microenvironment with Coherent Anti–Stokes Raman Scattering microscopy. *Plastic and Reconstructive Surgery* 2009;123(2S):123S-30S.

132. Fu Y, Huff TB, Wang H-W, et al. *Ex vivo* and *in vivo* imaging of myelin fibers in mouse brain by coherent anti-Stokes Raman scattering microscopy. *Optics Express* 2008;16(24):19396-409.

133. Fu Y, Wang H, Huff TB, et al. Coherent anti-stokes Raman scattering imaging of myelin degradation reveals a calcium-dependent pathway in lyso-PtdCho-induced demyelination. *Journal of Neuroscience Research* 2007;85(13):2870-81.

134. Parekh SH, Lee YJ, Aamer KA, et al. Label-Free Cellular Imaging by Broadband Coherent Anti-Stokes Raman Scattering Microscopy. *Biophysical Journal* 2010;99(8):2695-704.

135. Bito K, Okuno M, Kano H, et al. Protein Secondary Structure Imaging with Ultrabroadband Multiplex Coherent Anti-Stokes Raman Scattering (CARS) Microspectroscopy. *The Journal of Physical Chemistry B* 2012;116(4):1452-57.

136. Camp JrCharles H, Lee YJ, Heddleston JM, et al. High-speed coherent Raman fingerprint imaging of biological tissues. *Nature Photonics* 2014;8(8):627-34.

137. Kiyomatsu H, Oshima Y, Saitou T, et al. Quantitative SHG imaging in osteoarthritis model mice, implying a diagnostic application. *Biomedical Optics Express* 2015;6(2):405-20.

138. Kale S, Biermann S, Edwards C, et al. Three-dimensional cellular development is essential for *ex vivo* formation of human bone. *Nature Biotechnology* 2000;18(9):954-8.

139. Chatterjee K, Lin-Gibson S, Wallace WE, et al. The effect of 3D hydrogel scaffold modulus on osteoblast differentiation and mineralization revealed by combinatorial screening. *Biomaterials* 2010;31(19):5051-62.

140. Charwat V, Schutze K, Holnthoner W, et al. Potential and limitations of microscopy and Raman spectroscopy for live-cell analysis of 3D cell cultures. *Journal of Biotechnology* 2015;205:70-81.

141. Kunstar A, Leferink AM, Okagbare PI, et al. Label-free Raman monitoring of extracellular matrix formation in three-dimensional polymeric scaffolds. *Journal of the Royal Society Interface* 2013;10(86):20130464.

142. Bonnier F, Knief P, Lim B, et al. Imaging live cells grown on a three dimensional collagen matrix using Raman microspectroscopy. *Analyst* 2010;135(12):3169-77.

143. Browne S, Monaghan MG, Brauchle E, et al. Modulation of inflammation and angiogenesis and changes in ECM GAG-activity via dual delivery of nucleic acids. *Biomaterials* 2015;69:133-47.

144. Brauchle E, Johannsen H, Nolan S, et al. Design and analysis of a squamous cell carcinoma in vitro model system. *Biomaterials* 2013;34(30):7401-7.

145. Ashton L, Lau K, Winder CL, et al. Raman spectroscopy: lighting up the future of microbial identification. *Future Microbiology* 2011;6(9):991-97.

146. Jarvis RM, Goodacre R. Discrimination of bacteria using surface-enhanced Raman spectroscopy. *Analytical Chemistry* 2004;76(1):40-7.

147. Kapetanaki S, Chouchane S, Girotto S, et al. Conformational differences in *Mycobacterium tuberculosis* catalase-peroxidase KatG and its S315T mutant revealed by resonance Raman spectroscopy. *Biochemistry* 2003;42(13):3835-45.

148. Chouchane S, Lippai I, Magliozzo RS. Catalase-peroxidase (*Mycobacterium tuberculosis* KatG) catalysis and isoniazid activation. *Biochemistry* 2000;39(32):9975-83.

149. Imran IP, Christian S, Stefanie R, et al. Coherent anti-Stokes Raman scattering for label-free biomedical imaging. *Journal of Optics* 2013;15(9):094006.

150. Steuwe C, Kaminski CF, Baumberg JJ, et al. Surface Enhanced Coherent Anti-Stokes Raman Scattering on Nanostructured Gold Surfaces. *Nano Letters* 2011;11(12):5339-43.

151. Huefner A, Kuan W-L, Barker RA, et al. Intracellular SERS Nanoprobes For Distinction Of Different Neuronal Cell Types. *Nano Letters* 2013;13(6):2463-70.

152. Steuwe C, Patel II, Ul-Hasan M, et al. CARS based label-free assay for assessment of drugs by monitoring lipid droplets in tumour cells. *Journal of Biophotonics* 2014;7(11-12):906-13.

153. Trevisan J, Angelov PP, Scott AD, et al. IRootLab: a free and open-source MATLAB toolbox for vibrational biospectroscopy data analysis. *Bioinformatics* 2013;29(8):1095-7.

154. Palaci M, Dietze R, Hadad DJ, et al. Cavitary disease and quantitative sputum bacillary load in cases of pulmonary tuberculosis. *Journal of clinical microbiology* 2007;45(12):4064-66.

155. Park DY, Kim JY, Choi KU, et al. Comparison of polymerase chain reaction with histopathologic features for diagnosis of tuberculosis in formalin-fixed, paraffin-embedded histologic specimens. *Arch Pathol Lab Med* 2003;127(3):326-30.

156. Ishida Y, Agata Y, Shibahara K, et al. Induced expression of PD-1, a novel member of the immunoglobulin gene superfamily, upon programmed cell death. *The EMBO journal* 1992;11(11):3887-95.

157. Wang X, Teng F, Kong L, et al. PD-L1 expression in human cancers and its association with clinical outcomes. *OncoTargets and therapy* 2016;9:5023-39.

158. Lugo-Villarino G, Hudrisier D, Benard A, et al. Emerging Trends in the Formation and Function of Tuberculosis Granulomas. *Frontiers in Immunology* 2013;3(405).

159. Squeglia F, Ruggiero A, Berisio R. Collagen degradation in tuberculosis pathogenesis: the biochemical consequences of hosting an undesired guest. *Biochemical Journal* 2018;475(19):3123-40.

160. Elkington PTG, Friedland JS. Matrix metalloproteinases in destructive pulmonary pathology. *Thorax* 2006;61(3):259.

161. Ruggiero S, Pilvankar M, Ford Versypt A. Mathematical Modeling of Tuberculosis Granuloma Activation. *Processes* 2017;5:79.

162. Ong CWM, Fox K, Ettorre A, et al. Hypoxia increases neutrophil-driven matrix destruction after exposure to *Mycobacterium tuberculosis*. *Scientific Reports* 2018;8(1):11475.

163. Ulrichs T, Kosmiadi GA, Trusov V, et al. Human tuberculous granulomas induce peripheral lymphoid follicle-like structures to orchestrate local host defence in the lung. *The Journal of Pathology* 2004;204(2):217-28.

164. Barber DL, Sakai S, Kudchadkar RR, et al. Tuberculosis following PD-1 blockade for cancer immunotherapy. *Science translational medicine* 2019;11(475).

165. Elkington PT, Bateman AC, Thomas GJ, et al. Implications of Tuberculosis Reactivation after Immune Checkpoint Inhibition. *American Journal of Respiratory and Critical Care Medicine* 2018;198(11):1451-53.

166. Helke KL, Mankowski JL, Manabe YC. Animal models of cavitation in pulmonary tuberculosis. *Tuberculosis* 2006;86(5):337-48.

167. Saeed W. Cavitating pulmonary tuberculosis: a global challenge. *Clinical medicine (London, England)* 2012;12(1):40-41.

168. Clayton K, Polak ME, Woelk CH, et al. Gene Expression Signatures in Tuberculosis Have Greater Overlap with Autoimmune Diseases Than with Infectious Diseases. *American Journal of Respiratory and Critical Care Medicine* 2017;196(5):655-56.

169. Tzelepis F, Blagih J, Khan N, et al. Mitochondrial cyclophilin D regulates T cell metabolic responses and disease tolerance to tuberculosis. *Sci Immunol* 2018;3(23).

170. Moura CC, Bourdakos KN, Tare RS, et al. Live-imaging of Bioengineered Cartilage Tissue using Multimodal Non-linear Molecular Imaging. *Scientific Reports* 2019;9(1):5561.

171. Devitt G, Howard K, Mudher A, et al. Raman Spectroscopy: An Emerging Tool in Neurodegenerative Disease Research and Diagnosis. *ACS Chemical Neuroscience* 2018;9(3):404-20.

172. Jones MG, Andriotis OG, Roberts JJ, et al. Nanoscale dysregulation of collagen structure-function disrupts mechano-homeostasis and mediates pulmonary fibrosis. *eLife* 2018;7.

173. Claverie R, Fontana MD, Duričković I, et al. Optical Sensor for Characterizing the Phase Transition in Salted Solutions. *Sensors* 2010;10(4):3815.

174. Walrafen GE, Pugh E. Raman Combinations and Stretching Overtones from Water, Heavy Water, and NaCl in Water at Shifts to ca. 7000 cm−1. *Journal of Solution Chemistry* 2004;33(1):81-97.

175. Dong R, Yan X, Pang X, et al. Temperature-dependent Raman spectra of collagen and DNA. *Spectrochimica Acta Part A: Molecular and Biomolecular Spectroscopy* 2004;60(3):557-61.

176. Votteler M, Carvajal Berrio DA, Pudlas M, et al. Raman spectroscopy for the non-contact and non-destructive monitoring of collagen damage within tissues. *Journal of Biophotonics* 2012;5(1):47-56.

177. Fishbein KW, Gluzband YA, Kaku M, et al. Effects of formalin fixation and collagen cross-linking on T2 and magnetization transfer in bovine nasal cartilage. *Magnetic Resonance in Medicine* 2007;57(6):1000-11.

178. van der Slot-Verhoeven AJ, van Dura EA, Attema J, et al. The type of collagen cross-link determines the reversibility of experimental skin fibrosis. *Biochimica et Biophysica Acta (BBA) - Molecular Basis of Disease* 2005;1740(1):60-67.

179. Smus JP, Moura CC, McMorrow E, et al. Tracking adipogenic differentiation of skeletal stem cells by label-free chemically selective imaging. *Chemical Science* 2015;6(12):7089-96.

180. FTIR and Raman Characteristic Peak Frequencies in Biological Studies *Vibrational Spectroscopy for Tissue Analysis*: CRC Press; 2012 p213-94.

181. Hannah RW, Mayo DW. Answers to the Exercises *Course Notes on the Interpretation of Infrared and Raman Spectra*: John Wiley & Sons, Inc.; 2004 p509-47.

182. Frushour BG, Koenig JL. Raman scattering of collagen, gelatin, and elastin. *Biopolymers* 1975;14(2):379-91.

183. Gurcan MN, Boucheron LE, Can A, et al. Histopathological Image Analysis: A Review. *IEEE Reviews in Biomedical Engineering* 2009;2:147-71.

184. Sathyamoorthy T, Tezera LB, Walker NF, et al. Membrane type 1 matrix metalloproteinase regulates monocyte migration and collagen destruction in tuberculosis. *The Journal of Immunology* 2015;195(3):882-91.

185. Kroemer G, Galluzzi L, Vandenabeele P, et al. Classification of cell death: recommendations of the Nomenclature Committee on Cell Death 2009. *Cell death and differentiation* 2009;16(1):3-11.

186. Gavrilin MA, Bouakl IJ, Knatz NL, et al. Internalization and phagosome escape required for *Francisella* to induce human monocyte IL-1β processing and release. *Proceedings of the National Academy of Sciences of the United States of America* 2006;103(1):141-46.

187. Welin A, Lerm M. Inside or outside the phagosome? The controversy of the intracellular localization of *Mycobacterium tuberculosis*. *Tuberculosis (Edinb)* 2012;92(2):113-20.

188. Simeone R, Sayes F, Song O, et al. Cytosolic access of *Mycobacterium tuberculosis*: critical impact of phagosomal acidification control and demonstration of occurrence in vivo. *PLOS Pathogens* 2015;11(2):e1004650.

189. Simeone R, Bobard A, Lippmann J, et al. Phagosomal rupture by *Mycobacterium tuberculosis* results in toxicity and host cell death. *PLOS Pathogens* 2012;8(2):e1002507.

190. Rubin EJ. The granuloma in tuberculosis--friend or foe? *The New England Journal of Medicine* 2009;360(23):2471-3.

191. Saka HA, Valdivia R. Emerging Roles for Lipid Droplets in Immunity and Host-Pathogen Interactions. *Annual Review of Cell and Developmental Biology* 2012;28(1):411-37.

192. Cox G, Kable E. Second-harmonic imaging of collagen. *Methods in Molecular Biology* 2006;319:15-35.

193. Fine KL, Metcalfe MG, White E, et al. Involvement of the autophagy pathway in trafficking of *Mycobacterium tuberculosis* bacilli through cultured human type II epithelial cells. *Cellular Microbiology* 2012;14(9):1402-14.

194. Toledo A, Benach JL. Hijacking and use of host lipids by intracellular pathogens. *Microbiology Spectrum* 2015;3(6).

195. Elkington P, Lerm M, Kapoor N, et al. In Vitro Granuloma Models of Tuberculosis: Potential and Challenges. *The Journal of Infectious Diseases* 2019;219(12):1858-66.

196. Stoller P, Celliers PM, Reiser KM, et al. Quantitative second-harmonic generation microscopy in collagen. *Applied Optics* 2003;42(25):5209-19.

197. Sanna V, Roggio AM, Siliani S, et al. Development of novel cationic chitosan-and anionic alginate-coated poly(D,L-lactide-co-glycolide) nanoparticles for controlled release and light protection of resveratrol. *International Journal of Nanomedicine* 2012;7:5501-16.

198. Pereira L, Sousa A, Coelho H, et al. Use of FTIR, FT-Raman and 13C-NMR spectroscopy for identification of some seaweed phycocolloids. *Biomolecular Engineering* 2003;20(4–6):223-28.

Appendix I – Relevant Raman peaks and CARS wavenumbers

Raman peak assignment for sodium alginate

Wavenumber (cm^{-1})	**Vibrational mode**	**Chemical bond**
807	skeletal	C-C
888	stretching	C-O
950 or **954**	bending or deformation	C-C-H, C-C-O or O-H
1000-1025	stretching	C-OH
1025		G residue
1095	stretching	C-O-C (saccharide structure)
1098	breathing	glycosidic ring (M residue)
1250-1290	stretching	C-O-C
1300	stretching	carboxylate
1400	deformation	CH_2
1412 or **1413**	symmetric stretching	carboxylate
1617 or **1625**	asymmetric stretching	carboxylate
2932	stretching	C-H

Table 4. Raman peak assignment for sodium alginate from the literature.[197,198]

Raman peak assignment for human type I collagen

Wavenumber (cm^{-1})	**Vibrational mode**	**Chemical bond**
814 or **815**	stretching	CC
917, 919 or 938	stretching	C-N (proline)
1003 or **1004**	stretching	C-C (phenylalanine)
1060 or **1062**	stretching	C-N
1123 or **1126**	stretching	CCC
1244 or **1248**	characteristic of	amide III
1263 or **1272**	characteristic of	amide III
1298 or **1299**	deformation	CH_2
1443, 1445 or **1446**	deformation	CH_2, CH_3
1650,1655 or **1664**	characteristic of	amide I

Table 5. Raman peak assignment for human type I collagen from the literature.[80,175,176]

CARS wavenumbers imaged and corresponding wavelengths

Wavenumber imaged (cm^{-1})	**CARS wavelength (λ_{CARS}, nm)**	**Pump wavelength (λ_{pump}, nm)**	**Stokes wavelength (λ_{Stokes}, nm)**
2845	649.80	797.17	1031
2850	649.38	796.86	1031
2930	642.7	791.81	1031
2960	640.23	789.93	1031
3030	634.55	785.59	1031

Table 6. List of wavenumbers imaged with CARS and corresponding wavelengths of the CARS signal detected. The Stokes wavelength is always constant at 1031 nm, whereas the wavelength of the pump laser beam was tuned to match the wavenumber of interest. Pump laser's wavelength was calculated using *Equations 5, 6, 7*.